IMAGING MENINGIOMAS
—
THE ROAD TO THE FIRST MEDICAL APPLICATION OF THE NOVEL MAGNETIC RESONANCE RHEOLOGY

Dissertation

zur

Erlangung des Doktorgrades (Dr. rer. nat.)

der

Mathematisch-Naturwissenschaftlichen Fakultät

der

Rheinischen Friedrich-Wilhelms-Universität Bonn

vorgelegt von

Sebastian Theilenberg

aus

Bergisch Gladbach

Bonn, Januar 2017

Angefertigt mit Genehmigung der Mathematisch-Naturwissenschaftlichen Fakultät der Rheinischen Friedrich-Wilhelms-Universität Bonn

1. Gutachter: Prof. Dr. Carsten Urbach

2. Gutachter: Prof. Dr. Karl Maier

Tag der Promotion: 16. Februar 2017

Erscheinungsjahr: 2017

Contents

Bibliography

Physical constants

Boltzmann constant $k_\mathrm{B} = 1.381 \times 10^{-23}\,\mathrm{J/K}$.

Gyromagnetic ratio $\gamma = 2.675 \times 10^{8}\,\mathrm{rad/(s\,T)}$.

Symbols

T_E Echo time.

Δ Time between the two motion encoding gradients, measured from the center of the first lobe to the one of the second one.

δ The length of one trapezoid motion encoding gradient lobe.

Δt_{90} Time between the 90° pulseand the start of the first motion encoding gradient.

ζ The slew time of a trapezoid motion encoding gradient lobe, i. e. the time needed to raise the gradient to maximum strength.

τ Time from the end of the second motion encoding gradient to the start of the falling motion of the movable shell.

$\tilde{\tau}$ Post Trigger Fill Time, i. e. $\tau + const.$, see section 2.1.2.1.

N_τ Number of averages measured per value of $\tilde{\tau}$, see section 2.1.2.1.

T_R Repetitiontime , i. e. the length of one run of an MRI sequence.

Introduction

Manual palpation as a means of investigating the mechanical properties of tissue by touching it, has been succeeding as a diagnostic tool throughout the history of medicine. Its usage can be traced back to the early physicians of ancient Egypt and Mesopotamia around 1550 BC and to the traditional Chinese medicine [1, 2]. Essentially, what physicians do with palpation is measuring mechanical parameters by applying a strain to the tissue (by pushing it) and “measuring” the resulting deformation by the sense of touch of the physician.

Even today, palpation is an inherent part of the diagnosis of diseases: a modern physician will palpate a specific part of the body like the abdomen to look for swellings or stiff inclusions. Palpation, however, does have its limits: it is purely qualitative, depends highly on the level of training of the one performing it, and it is naturally limited to tissue that is accessible to the touch of the physician [2]. In modern medicine, physicians have a multitude of imaging modalities at their hands, each of them depicting specific properties of the tissue, to aid diagnosing and controlling the process of certain diseases. These include radiography and computed tomography (imaging the absorption coefficient of x-rays), ultrasound (US) (usually depicting the acoustic impedance), Magnetic Resonance Imaging (MRI) (imaging the distribution of water in tissue), and PET, which is able to depict the metabolism [3]. It is, therefore, no wonder that the wish for an imaging method emerged that is capable to objectively depict mechanical properties of tissue even in areas that manual palpation cannot reach.

Development of such a mechanical form of palpation began in the 1950s with the works of Oestreicher and von Gierke et al. who studied vibration of the surface of the human body [4, 5]. The works of Dickinson and Hill as well as of Wilson mark the beginning of the development of techniques using US to image the mechanical properties of tissue in the 1980s [6, 7]. In the following years a multitude of techniques emerged that are collectively termed *elastography*. These techniques include vibration elastography imaging where Doppler US is used to image externally introduced vibrations of low frequency [8, 9], compression elastography where US scans with and without static compression are compared [10], techniques based on the imaging of generated shear waves [11–13], and those using acoustic radiation force [14].

In the mid 1990s Magnetic Resonance Elastography (MRE) emerged using either quasi-static deformations [15] measured using a tagging method [16, 17] or a dynamic approach based on shear wave propagation [18, 19]. Later, techniques combining US and MRI were developed [20–23]. These use US to deform the tissue under investigation and depict the resulting deformations using MRI. Since its beginning, elastography has been applied – with partly great success – to various forms of human tissue and to various diseases. A good overview can be found in e. g. [24, 25].

The human brain enclosed in the hard cranial bone is rather unique in the human body. US cannot penetrate the skull in a controlled matter, so that US based approaches of elastography are not feasible for brain tissue (unless in rare cases where the skull is opened, e. g. during surgery). Investigating the mechanical properties of brain tissue in vivo, therefore, only started in the mid 2000s [26] after the emergence of dynamic MRE, whose imaging method is not stalled by the cranial bone.

In dynamic MRE, low frequency shear waves (20 Hz to 200 Hz) are introduced into the tissue by external vibrations of the head and the propagation of these waves is observed using motion sensitive magnetic resonance (MR) phase imaging. From the resulting data mechanical parameters are calculated. Using MRE it was possible to show that various neurological diseases alter the mechanical tissue properties, including brain tumors [27, 28], multiple sclerosis [29], and Alzheimer's disease [30].

However, the results obtained for brain tissue with MRE can vary significantly [31, 32], which can be attributed to different algorithms used to calculate these parameters [33, 34] and to the frequency of the applied vibrations [32]. Additionally, the shear waves generated through external vibrations enter the brain tissue through the very lossy meninges that hamper their propagation. The brain tissue itself shows high damping of these waves, too, especially for higher frequencies. This might lead to locally different excitations of the tissue and may cause reduced sensitivity in the deeper regions of the brain [35]. Consequently, most MRE studies only report average values for the mechanical properties of brain tissue, either globally for the whole investigated volume, or for specific region of interests [cf. e. g. 27].

In this thesis the feasibility of an alternative approach to depict mechanical properties of brain tissue which we call Magnetic Resonance Rheology (MRR) is investigated [36–38]. It is based on a short fall (≈1 mm) of the head resulting in a global excitation of the brain tissue aiming for a homogeneous sensitivity throughout the whole brain. This short excitation and the subsequent investigation of the tissue response is similar to a creep recovery experiment known from rheology, hence the name of the novel method. In its approach MRR is similar to the works of Bayly et al. [39]. However, MRR utilizes MR phase imaging instead of tagging techniques to measure the resulting deformations and works with significantly smaller accelerations. The technical development of MRR has been described by Ulucay [40].

In this thesis means to post-process and analyze the measured phase data and to precisely determine the excitation by the falling motion are presented. Additionally, methods to deduce the tissue response from the measured data are described and tested. The nature of the MRR signal is investigated using numerical simulations and the influence of the stiffness and density of the investigated material is shown on the basis of agar based phantoms. These results are then transfered to in vivo measurements on a healthy volunteer. Finally, the feasibility of MRR to depict local abnormal alterations in the mechanical properties of brain tissue is investigated in a study on four patients suffering from meningiomas, a specific kind of benign brain tumor.

In chapter 1 the theoretical concepts for this thesis are introduced. These include the basic principles of rheology, MRI and phase unwrapping as well as the anatomy and the mechanical properties of the human brain. Chapter 2 describes the experimental methods used for the experiments presented in this thesis: the main principle of MRR is explained and the technical realization of the experiment is described. Additionally, the measurement protocols used for the phantoms and the human subjects are described. Subsequently, the methods used to analyze the data obtained in the MRR experiments are described and in parts discussed in chapter 3. These include a detailed analysis of the induced falling motion of the probe and the post-processing of the obtained phase data. In the first part of chapter 4 numerical simulations are presented. These were used to predict the signals an MRR experiment will produce and to test means to infer the physical trajectory of the probe material from the measurement data. In the following parts, measurements under laboratory conditions and the results of MRR measurements on phantoms and on a healthy volunteer as well as on tumor patients are presented. These results are finally discussed in chapter 5.

Parts of the contents of this thesis have been published in [38].

Throughout this thesis, vectorial entities and tensors are printed in bold ($\boldsymbol{x}$), Fourier transformed entities are marked as $\mathcal{F}(x)$ and the convolution is indicated by the symbol “$*$”. Physical constants and important symbols are summarized at the beginning of the document.

1 Theory

This chapter is intended to provide short introductions into the main topics needed to understand the results presented in this thesis.

It begins with the basic concepts of rheology followed by a brief introduction into the anatomy of the human brain and its mechanical properties. Afterwards the physical foundations of MRI are presented, which is used as a imaging technique in this thesis. The chapter closes with a section concerning coordinate systems in the context of medical imaging and an introduction into phase unwrapping.

1.1 Rheology

Many materials do not simply show ideal elastic or fluid behavior, but exhibit a combination of elastic, viscous and plastic behavior. The study of such materials is the aim of rheology. The term was coined by Eugene Cook Bingham, whose collaboration with Markus Reiner in the late 1920's lead to the formation of rheology as a distinct branch of physics [41]. The term was inspired by the greek phrase πάντα ῥεῖ – "everything flows".

This section gives a short introduction to the basic concepts used in rheology to describe complex materials. Much more detailed explanations can be found in [42–44].

1.1.1 Basic Constitutive Equations

In rheology, material behavior is described by material functions that link acting stresses to the strain the material experiences. Three basic material models are defined describing an ideal elastic solid, an ideal viscose fluid and irreversible plastic behavior, which are introduced in the following. To illustrate the material behavior associated with these models, their behavior in a so-called creep recovery experiment is shown. In such an experiment, a constant stress τ_0 is applied for a certain time and the strain of the material is measured during the application of the stress (creep) and after the stress is removed (recovery).

An ideal elastic solid is represented by a spring, a so-called *Hooke element* (cf. fig. 1.1a). When it is exposed to a shear stress τ_H, it instantaneously shows a proportional finite strain γ_H:

$$\tau_\mathrm{H}(t) = G \cdot \gamma_\mathrm{H}(t), \tag{1.1}$$

The coefficient G is called shear modulus and is a material property. If the stress is relaxed, the strain instantaneously vanishes such that the deformation is reversible (cf. fig. 1.1b).

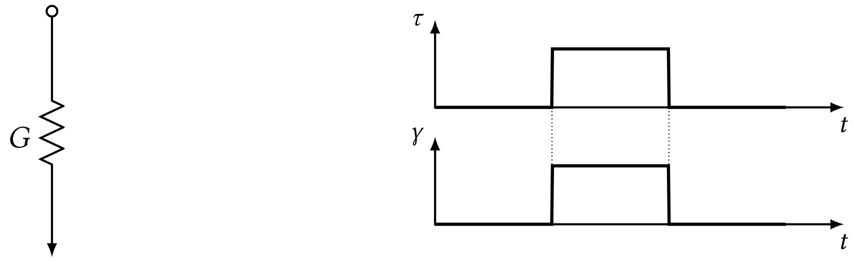

(a) *Hooke element* ***(b)*** *Creep recovery experiment*

Figure 1.1: *Elastic solid:*
An ideal elastic solid material is represented by a Hooke element (a). In a creep recovery experiment (b) the the strain γ follows the stress τ instantaneously and proportionally. When the stress is released, the deformation is fully reversed. [adapted from 43].

For an ideal viscose fluid, the stress is proportional to the rating of straining:

$$\tau_{\mathrm{N}}(t) = \eta \cdot \dot{\gamma}_{\mathrm{N}}(t), \tag{1.2}$$

with the dynamic shear viscosity η. During deformation, such a Newtonian fluid dissipates energy, so that the deformation is irreversible. Such a material behavior is represented by a damper, or *Newton element* (cf. fig. 1.2a).

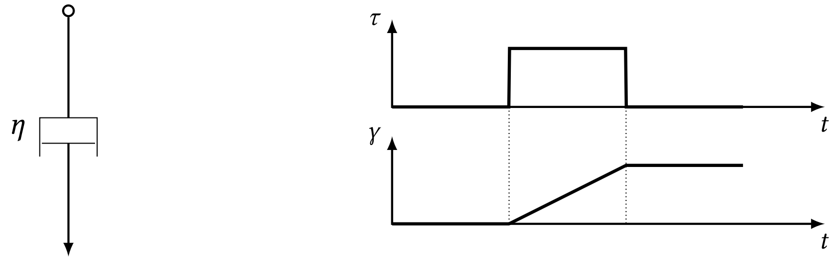

(a) *Newton element* ***(b)*** *Creep recovery experiment*

Figure 1.2: *Newtonian liquid:*
An ideal viscose fluid is represented by the Newton element (a). Such a material only deforms delayed to the application of a stress τ. During the deformation it dissipates energy, so that the deformation is irreversible (b). The slope of the strain function during constant stress is proportional to $\frac{1}{\eta}$. [adapted from 43].

In a creep recovery experiment, the Newton element is deformed as long as a stress is acting on the element, and remains in the deformed state when the stress vanishes (cf. fig. 1.2b).

An ideal plastic solid is represented by a sliding block called *St.-Venant element* (cf. fig. 1.3). It behaves like a rigid solid for stresses below a yield stress $\tau_{\mathrm{V}} \leq \tau_f$ and behaves like a fluid with infinitesimal viscosity once $\tau_{\mathrm{V}} \geq \tau_f$.

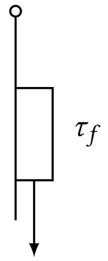

Figure 1.3: *St.-Venant element:*
A sliding block represents plastic behavior. It behaves like a rigid solid until a yield stress is overcome. It then flows readily and deforms irreversibly. It can in principle take every strain rate. [adapted from 43].

1.1.2 Viscoelasticity

Many real materials show both elastic and viscose behavior and are therefore called viscoelastic. Their behavior can be modeled by linearly superposing Hooke and Newton elements. If the deformation of such a model is fully reversible, it is called a viscoelastic solid, while a model showing irreversible deformations is called a viscoelastic fluid.

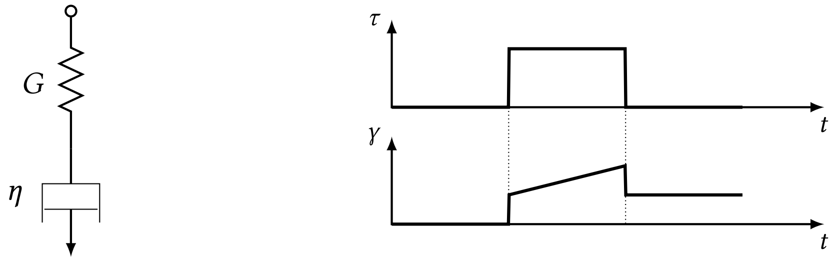

(a) *Maxwell element* ***(b)*** *Creep recovery experiment*

Figure 1.4: *Viscoelastic fluid:*
(a)) the so-called Maxwell element is a series connection of a Hooke and a Newton element. (b) In the presence of a stress τ the Hooke element deforms instantaneously while the Newton element moves delayed. When the stress is released, the deformation of the Newton element is not reversed. [adapted from 43].

A series connection of a Hooke and a Newton element is called a *Maxwell element* (cf. fig. 1.4a). Here, the stress is acting on both constitutive elements equally, while the total strain is the sum of the strain of both constitutive elements:

$$\dot{\gamma} = \dot{\gamma}_{\mathrm{N}} + \dot{\gamma}_{\mathrm{H}} = \frac{1}{\eta}\tau + \frac{1}{G}\dot{\tau}. \tag{1.3}$$

Under constant stress this turns into eq. (1.2), so that this material behaves like a fluid and is, therefore, called a viscoelastic fluid. The elastic part of the model creates an instant deformation when a stress acts on the material. Only the part of the deformation that is associated with the Hooke element is reversible (cf. fig. 1.4b).

Superposing a Newton and a Hooke element under collective strain results in a parallel connection of both elements (cf. fig. 1.5a). This model is called *Kelvin-Voigt element.* Here, the stresses are summed up:

$$\tau = \tau_{\mathrm{H}} + \tau_{\mathrm{N}} = G\gamma + \eta\dot{\gamma}. \tag{1.4}$$

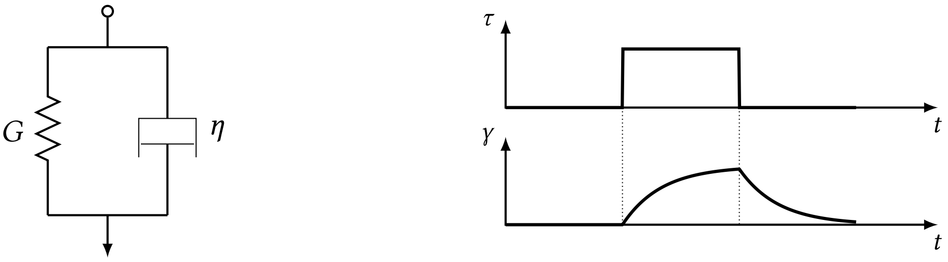

(a) Kelvin-Voigt element *(b) Creep recovery experiment*

Figure 1.5: *Viscoelastic solid:*
(a) The Kelvin-Voigt element is a parallel connection of a Hooke and a Newton element. (a) If a stress τ is applied, the deformation of the Hooke element is slowed down by the Newton element. For short times, the element therefore acts like a fluid (cf. fig. 1.2b). For longer times, however, the strain is limited by the deformation of the Hooke element. When the stress is released, the element exponentially recovers to the original state. [adapted from 43].

For the strain of such a material in a creep experiment, eq. (1.4) yields

$$\gamma(t) = \frac{\tau_0}{G}\left(1 - e^{-t\frac{G}{\eta}}\right). \tag{1.5}$$

Since such a material does not experience any irreversible deformation (cf. fig. 1.5b), it is called a viscoelastic solid.

In principle, numerous basic elements can be combined while keeping in mind that parallel connected elements experience equal strain while serial connected elements experience equal stress. This can be used to create complex models describing increasingly realistic material behavior. For example, a series connection of a Hooke element and a Kelvin-Voigt element leads to a more realistic description of a real fluid showing retarded elasticity (cf. fig. 1.6a). On the other hand, by combining all three basic elements described in section 1.1.1 to a so-called *Elastic Bingham element* (cf. fig. 1.6b), one can create a fluid that behaves elastic up to a certain yield stress. Such a behavior can be observed for example in Ketchup.

1.1.3 Oscillatory Behavior

Next to the here exemplarily discussed creep-recovery experiment that measures the deformation to a given stress, relaxation experiments in which the deformation is given are common. Another approach is to use oscillatory deformations of the form

$$\gamma = \tilde{\gamma}\sin(\omega t) \tag{1.6}$$

and to measure the phase shift between this strain and the resulting stress. In a material without viscose behavior, this phase shift vanishes, while an ideal viscose material shows a phase difference of $\pi/2$.

Typically, a complex shear modulus $G^* = G' + iG''$ is defined: the storage modulus G'

(a) *Voigt-Maxwell element* ***(b)*** *Elastic Bingham element*

Figure 1.6: *Rheological models consisting of three basic elements:*
By combining three basic elements, more complex material behavior can be modeled. The Voigt-Maxwell element (a) is a series connection of a Kelvin-Voigt and a Newton element. It models an energy dissipating fluid with retarded elasticity. The Elastic Bingham element (b) is a combination of all three basic elements. It models the behavior of a fluid, that is elastic up to a certain yield stress. [adapted from 43].

is a measure for the elastic component of the material, whereas the loss modulus G'' is a measure for the viscose component. The strain of a general viscoelastic material can then be described by

$$\begin{aligned} \gamma &= \tilde{\gamma} G' \sin(\omega t) + \tilde{\gamma} G'' \cos(\omega t)) \\ &= \tilde{\gamma} |G^*| \sin(\omega t + \delta) \end{aligned} . \tag{1.7}$$

The phase angle of the complex shear modulus $\delta = \arctan \frac{G''}{G'}$ is also called loss tangent.

1.1.4 Complex Material Behavior

The rheological models in this section have been introduced using one-dimensional shear stress and strain. Due to the linear approach of the theory, the equations can be derived analogously for axial strains. Typically, the elastic modulus E is used in this case instead of the shear modulus G.

A three-dimensional treatment of the material behavior is achieved by combining these equations into tensor-equations (cf. e. g. [42]) using the stress tensor $\boldsymbol{\tau}$ and the strain tensor $\boldsymbol{\epsilon}$ with its components [43]

$$\epsilon_{ij} = \frac{1}{2} \left(\frac{\partial u_i}{\partial x_j} + \frac{\partial u_j}{\partial x_i} \right), \tag{1.8}$$

with the displacements u_i in the direction of x_i. These tensors unite axial and shear stresses and strains respectively.

The linear theory of viscoelasticity derived here is only valid in the realm of small strains of only a few percent. In case of larger deformations or to model more complex material behavior non-linear descriptions are needed that can be derived from continuum mechanics. Often, so-called hyperelastic material models are used, like the Mooney-

Rivlin [45] or the Ogden model [46].

1.2 The Human Brain

The brain is one of the – if not the most – important organs of the human body. It consists of shock- and pressure-sensitive soft tissue that is protected by the hard cranial bone and a fluid cushion. This section provides a brief overview of the brain's anatomy. Furthermore, an overview of the mechanical properties of the brain tissue is given, and neuronal diseases that alter these properties are discussed.

Various educational books are available to provide more detailed information about the anatomy of the brain, see for example [47–49].

1.2.1 Anatomy of the Human Brain

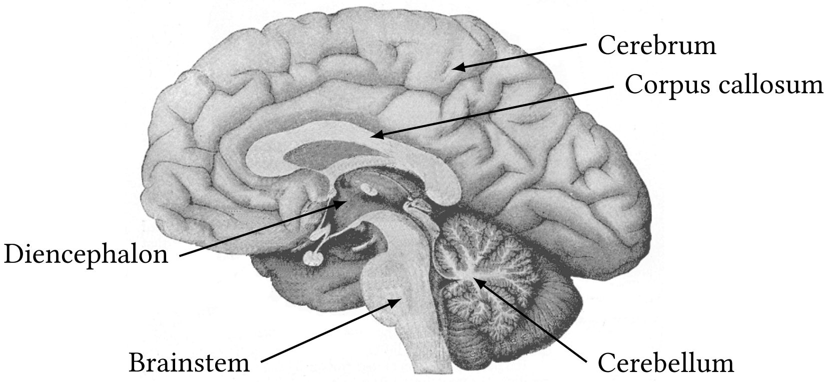

Figure 1.7: *Aspect of the brain sectioned in the median sagittal plane. [modified from 50]*

The brain forms, together with the spinal cord, the central nervous system (CNS). It can be divided into four main parts (cf. fig. 1.7):

- the brainstem connecting the brain to the spinal cord (consisting of the medulla oblongata, the pons and the midbrain)
- the cerebellum
- the diencephalon in the center of the brain (consisting of epithalamus, thalamus, hypothalamus and subthalamus)
- and the cerebrum (consisting mainly of the two cerebral hemispheres).

The cerebrum forms two hemispheres separated by the longitudinal cerebral fissure. Both hemispheres are connected by the corpus callosum located at the floor of the cerebral fissure. The outer few millimeter of the hemispheres – called cerebral cortex – form gyri (elevations) and sulci (depressions) to increase the surface area. The cerebral cortex is comprised of the cell bodies of neurons (called gray matter), which process signals. Gray matter is also found in the deeper structures of the cerebrum as nuclei and in the diencephalon as well as the cerebellum. The bulk of the cerebrum consists of white matter, which contains the nerve fibers that transmit signals between the neuronal cell bodies in the cerebral cortex and other regions of the CNS like the nuclei.

Apart from the neurons, brain tissue also consists of neuroglia. These cells reinforce the tissue, protect the neurons and fulfill various supporting tasks: amongst others, they play an important role in the nutrition of the neurons that are not connected to the blood circuit and they are part of the immune system of the brain. The neuroglia make up for 50 % of the volume of the CNS and provide 90 % of its cells [49].

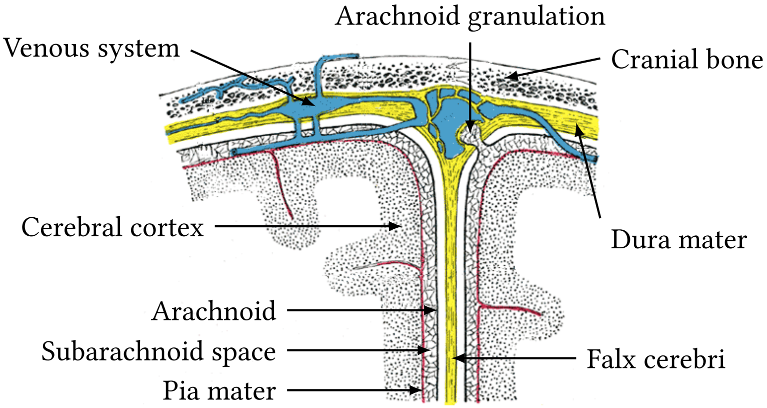

Figure 1.8: *Diagram of a section across the top of the scull showing the meninges: The brain is separated from the cranial bone by three layers of meninges and the cerebrospinal fluid flowing in the subarachnoid space. In the space between the two hemispheres, the dura mater forms the falx cerebri. [modified from 50]*

The brain is surrounded by three meninges that separate the hard cranial bone from the soft brain tissue (cf. fig. 1.8). The outermost of these membranes is the dura mater, a tough and dense connective tissue that is firmly connected to the cranial bone. In the cerebral fissure, the dura mater forms the falx cerebri separating the two hemispheres of the cerebrum. Connected to the inner side of the dura mater is the arachnoid, that follows the course of the dura mater. It is a very fine membrane that forms the so-called arachnoid trabeculae that extend towards the pia mater. These trabeculae form the subarachnoid space. The pia mater is the inner most membrane connected directly to the brain tissue and following its sulci and gyri.

The subarachnoid space is filled with the cerebrospinal fluid (CSF). The brain is therefore effectively embedded into a fluid cushion protecting it from mechanical loads from the outside [51]. Since the brain effectively swims in the CSF, its weight is reduced from approximately 1250 g to 1500 g to about 50 g with which it presses against the cranial bone [48, 49]. The CSF is a clear fluid manufactured in the ventricles, a cavernous system of four interconnected cavities. These are located in the center of the two hemispheres (lateral ventricles), the diencephalon (third ventricle) and between the brainstem and the cerebellum (fourth ventricle). 500 mL to 800 mL of CSF are produced per day, but only 150 mL are present at any one time. Roughly 20 % of this is located in the ventricular system while the rest fills the subarachnoid space. The CSF is constantly resorbed in the arachnoid granulations, which are excrescences of the arachnoid into the venous system (cf. fig. 1.8). Apart from the mentioned role of mechanical protection of the brain, the CSF is also the recipient of brain metabolites and with that plays an important role in the maintenance of a constant extracellular environment.

1.2.2 Mechanical Properties

The mechanical properties of brain tissue have been an active area of research for several decades since Pudenz and Shelden started first experiments on mammals in the 1940s [52]. Those few early results have been summarized in a review by Ommaya [53]. First in vitro experiments on human subjects followed in 1969 by Fallenstein et al. and in 1970 by Galford and McElhaney [54, 55].

In the following years, several studies investigated the rheological properties of different brain tissues both of different mammals and of humans [32, 56]. However, the reported values for different rheological parameters for brain tissue vary over several magnitudes. This high spread can be attributed to different methodical techniques and differences in the sample preparations in in vitro measurements. Additionally, the reported rheological parameters (like shear, compression or relaxation modulus) are hard to compare since their relationship depends on a priori unknown tissue properties like compressibility or heterogeneity.

Nevertheless, there is consensus that brain tissue is a non-linear viscoelastic material with a very small linear strain limit of 0.1 % to 0.3 %, although values of up to 1 % have been reported as well [51]. The shear modulus of brain tissue increases in oscillatory measurements with the loading frequency [32]. It is approximately incompressible [57] and its density is close to the one of water, while the meninges and the CSF have a slightly higher density (cf. table 1.1). Albeit their different structure (cf. the last section), gray and white matter have the same density [58].

Tissue	Density [g/cm^3]
Cranial bone	1.807(10)
Dura mater	1.133(10)
Pia mater & arachnoid	1.171(77)
CSF	1.007(9)
Brain tissue	1.081(3)

Table 1.1: *Values for the densities of different brain tissues and the respective standard errors. [data taken from 58]*

Since brain tissue changes its properties significantly immediately after death [cf. e. g. 59], it is preferable to measure the mechanical properties in vivo. A non-invasive method for such a measurement is MRE which was developed in the mid 1990s [18] and is still an active field of research to this day. An overview of its applications can be found in [25, 31]. MRE uses vibrations to induce shear waves in the tissue, whose propagation is measured via MR phase imaging. From the resulting data, the different rheological properties are calculated. The first application of MRE to brain tissue in vivo was conducted in 2005 [26, 60]. Since then several studies have been performed using different methods to create the shear waves: External actuators like bite bars [61, 62] or head cradles [63] have been used as well as scanner vibrations [64] or the natural physiological pulsation of the brain [34].

Values of mechanical properties of brain tissue measured with MRE still differ significantly dependent on the algorithm used to deduce parameters from the wave data and the method used to apply the vibrations [31, 32]. However, in a very recent review, Hiscox et al. tried to compare several recent MRE studies by calculating the mean shear stiffness of the brain tissue from the available data. They find values in a range from 0.62 kPa to 2.99 kPa [65].

1.2.3 Diseases of the Human Brain

Many diseases alter the structure or composition of the afflicted tissue. Consequentially one might expect changes in the mechanical properties of diseased tissue with respect to healthy tissue. Using MRE, it became possible to investigate such diseases in vivo. First preliminary work in that direction for brain tissue was done by Xu et al. in 2007 for intracranial tumors [66]. Very recently, several studies explored the influence of different kinds of neuronal disorders on the mechanical properties of the tissue using more elaborate MRE techniques [65]. In the following some of these diseases are introduced briefly.

1.2.3.1 Intracranial Tumors

Intracranial tumors can either arise as primary tumors in the brain tissue or the meninges, or they occur as metastases of primary tumors elsewhere in the body. Tumors are rated according to the WHO-classification into four categories depending on their malignancy from grade I (a benign, non cancerous tumor) to grade IV (a highly malign tumor) [67].

Of the primary tumors, gliomas are the most common ones (≈50 %). This term covers several tumor of different grades (astrocytomas including glioblastomas, oligodendrogliomas, ependymomas) that originate from the glia cells of the brain tissue. The second most common tumors are meningiomas originating from the meninges (≈20 %). They are usually benign of grade I [68].

MRE pilot studies recently showed that malignant gliomas tend to show smaller mean values of the complex shear modulus than comparable tissue in a healthy part of the brain of the same patient, while meningiomas tend to be slightly stiffer and more lossy [27, 69]. Murphy et al. reported a correlation between MRE results of mean relative meningioma stiffness (again compared to healthy tissue) and a qualitative assessment of the tumor stiffness by the surgeon during resection [28]. In parts this could be translated to an assessment of meningioma heterogeneity using space-resolved MRE [70].

1.2.3.2 Multiple Sclerosis

Multiple sclerosis (MS) is an inflammatory disease of the CNS in which the insulating covers of the neurons (myelin) in the white matter is destroyed. It is one of the most common neurological diseases with an incidence of approximately 4 per 100 000 residents per year. Its cause is not yet fully explained. Symptoms of MS include muscle weakness and paralysis, vision disorders, and mental or psychiatric symptoms. These symptoms develop in isolated attacks or are built up over time [68]. The first neurological episode of a patient is called clinically isolated syndrome (CIS). Only 60 % of CIS patients develop MS [71].

First MRE studies on MS patients were conducted in 2010 and reported changes in the mechanical properties of the brain tissue [29, 72]. Recently a reduction of white matter stiffness in CIS patients was reported, although no differences were found between those patients that later developed MS and those who did not [73].

1.2.3.3 Alzheimer's Disease

Approximately 7 % of all individuals over the age of 65 suffer from dementia. In at least 50 % of these patients the source of the dementia is Alzheimer's disease (AD). Patients with AD slowly develop neurodegeneration that is accompanied by increasingly severe dysfunctions in retentiveness, orientation, speech and writing. The cause of AD is not yet understood, but the main risk factors include age and family history. [68]

Using MRE techniques, a globally decreased stiffness of the brain tissue was found for AD patients [30] that increases with the severity of the disease [74].

1.2.3.4 Normal Pressure Hydrocephalus

Hydrocephalus is a broadening of the ventricular system caused either by a disturbed CSF drain or by a insufficient resorption of the CSF in the arachnoid granulations (cf. section 1.2.1 and fig. 1.8), accompanied by an increased intracranial CSF pressure. In normal pressure hydrocephalus (NPH), the pressure in the CSF appears normal when measured during a lumbar puncture, although the intracranial pressure is altered. Patients with NPH suffer from gait disturbances, cognitive deficiencies and incontinence. NPH is usually treated by inserting a shunt to enable a pressure equalization. [68]

Using MRE, a softening of the brain tissue was found in patients with NPH [75] that were only reverted in parts after shunt treatment [76]. However, these findings seem to be inconclusive since another study reported a stiffening of the brain tissue of NPH patients [77].

1.3 Magnetic Resonance Imaging

MRI is a widespread medical imaging technique that is used in MRR to measure tissue motion. It is based on the concept of Nuclear Magnetic Resonance (NMR) that was first investigated by Rabi et al. on particle beams and which was later discovered for hydrogen in solids independently by Purcell et al. [78] and Bloch et al. [79, 80]. Bloch and Purcell got awarded the Nobel Prize in Physics in 1952 for their work. Amongst others, the works of Lauterbur and Mansfield et al. [81, 82], who got awarded the Nobel Prize in Physiology

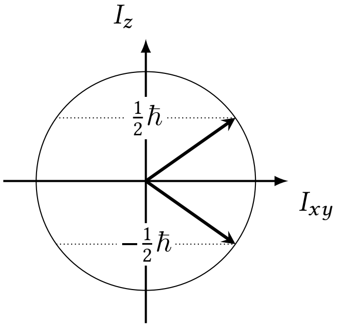

Figure 1.9: *Schematic diagram of a spin* $1/2$ *particle. The two possible spin states are spin up and spin down, with the inclination of* $\boldsymbol{I}$ *determined by the magnetic quantum number* $m_z = \pm 1/2$. *The azimuthal angle is undetermined.*

or Medicine for this work in 2003, lead to the construction of the first MRI scanner in the 1970s.

This section will give a basic introduction to NMR and the fundamental principles of MRI. More detailed descriptions can be found for example in [3, 83].

1.3.1 Nuclear Magnetic Resonance

Nuclei consisting of an uneven number of nucleons possess an non-vanishing spin angular momentum $\boldsymbol{I}$, that - because of its electrical charge - is accompanied by a magnetic dipole moment $\boldsymbol{\mu} = \gamma \boldsymbol{I}$. The constant γ is the *gyromagnetic ratio* that is a characteristic value of a given nucleus. For protons, this value is $\gamma = 2.675 \times 10^8\,\mathrm{rad/(s\,T)}$. The magnitude of $\boldsymbol{I}$ is

$$|\boldsymbol{I}| = \hbar\sqrt{I(I+1)}, \tag{1.9}$$

with I being the *nuclear spin quantum number* and $\hbar = h/2\pi$ as the reduced Planck constant. Since the quantum mechanic spin operators $\hat{S}_x$, $\hat{S}_y$ and $\hat{S}_z$ do not commute, the direction of $\boldsymbol{I}$ cannot be determined. By applying an external magnetic field $\boldsymbol{B}_0$ in z-direction, however, the degeneracy of the eigenstates of the angular momentum is suspended (nuclear Zeeman effect). $\boldsymbol{I}$ will then be oriented in $2I + 1$ possible directions along the direction of $\boldsymbol{B}_0$ with a z-component of $I_z = m_z\hbar$, where m_z is the *magnetic quantum number* with the possible values $-I, -(I-1), \cdots, +I$.

Protons have a spin quantum number of $I = +\frac{1}{2}$, therefore, they have two possible directions (see figure 1.9). These two orientations correspond to two different energy levels, of which the one with a vector component of $\boldsymbol{I}$ parallel to $\boldsymbol{B}_0$ ("spin-up", in contrast to "spin-down") is energetically favorable. The energy difference of these states is

$$\Delta E = 2 \cdot \boldsymbol{\mu} \cdot \boldsymbol{B}_0 = 2\gamma I_z B_0 = \gamma\hbar B_0 \tag{1.10}$$

In the thermal equilibrium, the ratio of the populations of the two states can be computed by the Boltzmann distribution

$$\frac{n_\uparrow}{n_\downarrow} = \exp\left(\frac{\Delta E}{k_\mathrm{B} T}\right), \tag{1.11}$$

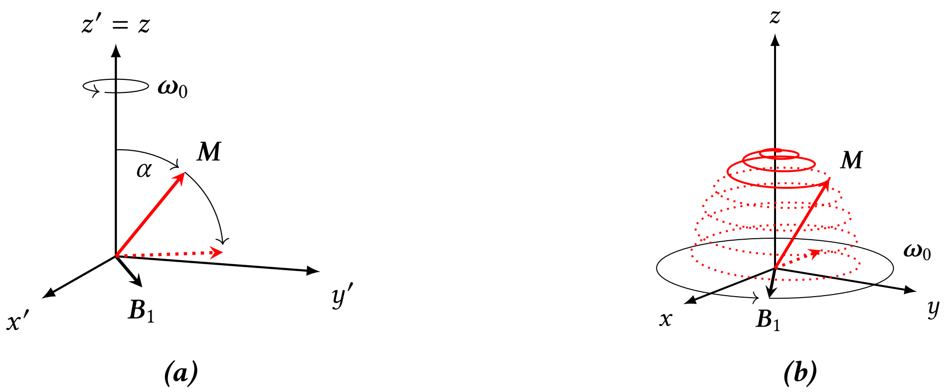

Figure 1.10: *Fabrication of a transversal magnetization.*
(a) In the rotating reference frame, a transversal magnetic field $\boldsymbol{B}_1$ rotating with $\boldsymbol{\omega}_0$ causes the otherwise stationary magnetization vector $\boldsymbol{M}$ to rotate around the direction of $\boldsymbol{B}_1$ towards the transversal plane. (b) In the laboratory frame, this corresponds to a spiral trajectory of the rotating magnetization. The angle α between the z-axis and the magnetization $\boldsymbol{M}$ depends on the strength of the transversal magnetic field and the length of its application.

where $n_\uparrow$ and $n_\downarrow$ are the number of nuclei in the spin-up respectively the spin-down state, k_B is the Boltzmann constant and T is the absolute temperature in the spin system. At 310 K (the approximate temperature of the human body) and a magnetic field of 1.5 T, this leads to a ratio of $\sim 1 \times 10^{-5}$.

Although not observable, an individual spin precesses around the direction of $\boldsymbol{B}_0$ with the *Larmor frequency*

$$\boldsymbol{\omega}_0 = -\gamma \boldsymbol{B}_0. \tag{1.12}$$

Since the precession of individual spins of an ensemble occur with individual phases, the magnetic moments sum up to zero in the xy-plane. The aggregated magnetization $\boldsymbol{m} = \sum_i \boldsymbol{\mu}_i$ of many nuclei (a so-called isochromat) is therefore parallel to $\boldsymbol{B}_0$. The magnetization $\boldsymbol{M}$ of a sample is then again the sum of many individual magnetization vectors $\boldsymbol{m}_i$. Just like the individual spins, $\boldsymbol{M}$, too, obeys the Larmor equation (1.12).

In water, 6.7×10^{14} protons per cubic millimeter contribute to the magnetization. Due to this large amount of spins aggregated into the vector $\boldsymbol{M}$, a classical description in form of a rotary is sufficient in most cases (the so-called *vector model* of NMR).

To simplify the further considerations, a rotating reference frame (x', y', $z' = z$) is defined, rotating with the Larmor frequency of protons around the z-axis. In equilibrium, $\boldsymbol{M}$ is stationary in this reference frame. By applying an additional magnetic field $\boldsymbol{B}_1$ oriented transversal to $\boldsymbol{B}_0$ and rotating at $\boldsymbol{\omega}_0$, transitions between the two energy states of the protons are induced (see (1.10)). This causes the magnetization $\boldsymbol{M}$ to rotate about the direction of $\boldsymbol{B}_1$ towards the $x'y'$-plane. (figure 1.10a). In the laboratory frame, this corresponds to a spiral trajectory of $\boldsymbol{M}$ (figure 1.10b). If the duration t of the irradiation of $\boldsymbol{B}_1$ is short in comparison to the sample's relaxation times (see next section), it is called a radio frequency pulse (RF pulse). Such a pulse will rotate $\boldsymbol{M}$ by an angle of $\alpha = \gamma B_1 t$.

Hence, a so-called 90° pulse will rotate $\boldsymbol{M}$ into the $x'y'$-plane and a 180° pulse will put $\boldsymbol{M}$ antiparallel to $\boldsymbol{B}_0$.

When a component of $\boldsymbol{M}$ in the $x'y'$-plane is created through application of a RF pulse, the rotating transversal magnetization creates a magnetic flux inside an antenna positioned around the probe. This induces a high-frequency signal in the antenna with a frequency of $\boldsymbol{\omega}_0$.

1.3.1.1 Relaxation

After the magnetization $\boldsymbol{M}$ is deflected by an RF pulse, it will return to its balanced state in the absence of $\boldsymbol{B}_1$, which is called relaxation. This transition has to take place by transitions between the nuclei's energy levels. The time needed until the magnetization is back in its state of equilibrium is dependent on the measured sample. There are two main relaxation processes, longitudinal relaxation and transversal relaxation. In the case of weakly interacting spins as in a liquid sample, both processes can be described accurately by Bloch's equations [84]. From those, the following considerations can be deduced.

The longitudinal relaxation (or spin-lattice relaxation[1]) describes the return of the z-component of magnetization M_z to its equilibrium value. This takes place with the characteristic longitudinal relaxation time T_1:

$$\frac{dM_z(t)}{dt} = -\frac{M_z(t) - M_z(0)}{T_1}. \tag{1.13}$$

This process describes the energy transfer between the spin system and the surrounding thermal bath, the lattice. Since spontaneous emission is suppressed, the primary mechanism is stimulated emission caused by fluctuating magnetic fields. These are generated by the dipole moments of neighboring molecules (such as water). Some of these magnetic fields will have a component in the $x'y'$-plane and a vibration frequency of ω_0, thereby stimulating transitions between the different energy levels of the spins. After a 90° pulse (1.13) yields for the longitudinal magnetization:

$$M_z(t) = M_z(0) \cdot \left(1 - e^{-t/T_1}\right). \tag{1.14}$$

The transversal relaxation (or spin-spin relaxation) describes the loss of magnetization from the $x'y'$-plane as a result of a loss of phase coherence between the different precessing magnetic moments of an isochromat, that takes place with the characteristic transversal relaxation time T_2:

$$\frac{dM_{xy}}{dt} = -\frac{M_{xy}(t)}{T_2}. \tag{1.15}$$

This relaxation is mainly the result of two processes: flips of two or more spins with no net transfer of energy but a loss of phase information, and small differences in the Larmor

---

[1] This term has historic reasons: The early experiments on NMR were performed on crystalline solids.

frequency of different spins. These are caused again by alterations of the effective magnetic field due to dipole moments of neighboring molecules that also have a z component. $T_2$is always equal or less than T_1. In practice, inhomogeneities in $\boldsymbol{B}$ caused by imperfections of the main magnet or by variations of the susceptibility of the sample cause further dephasing of different isochromats, leading to a much faster transversal relaxation that can be described by an effective time constant T_2^*. The transversal magnetization after a 90° pulse can then be derived from (1.15) as

$$M_{xy}(t) = M_{xy}(0) \cdot e^{-t/T_2^*}. \tag{1.16}$$

The signal in an antenna right after a RF pulse is called free induction decay (FID). It, too, decays with T_2^*.

Typical relaxation times for different brain tissues are listed in table 1.2.

1.3.1.2 Magnetic Field Gradients

In a spacious sample, the progression of the magnetization of individual isochromats can be further manipulated by the use of magnetic field gradients. By superimposing a linear magnetic gradient $\partial B/\partial r = G$ to the main field $\boldsymbol{B}_0$ along an arbitrary spatial direction $\hat{\boldsymbol{r}}$, the Larmor frequency of protons in the probe will vary according to [3]

$$\omega(\boldsymbol{r}) = -\gamma B_0(\boldsymbol{r}) = -\gamma(B_{00} + \boldsymbol{r} \cdot \boldsymbol{G}). \tag{1.17}$$

This variation maps the spatial location of the magnetization to its frequency (see figure 1.11).

During the time t the gradient is present, a magnetization vector at position $\boldsymbol{r}$ addition-

Tissue	^{1}H-density [%]	T_1[ms]	T_2[ms]
Liquor	100	>4000	>2000
Gray Matter	70	780	90
White Matter	85	920	100
Meningioma	90	400	80
Metastasis	85	1800	85
Adipose Tissue	100	260	80

Table 1.2: *Proton densities and relaxation times for different tissues present in the human brain at $B_0 = 1.5\,\mathrm{T}$. These values may differ greatly due to aging, water content, etc. Data taken from [85], a more detailed compilation may be found e.g. in [83].*

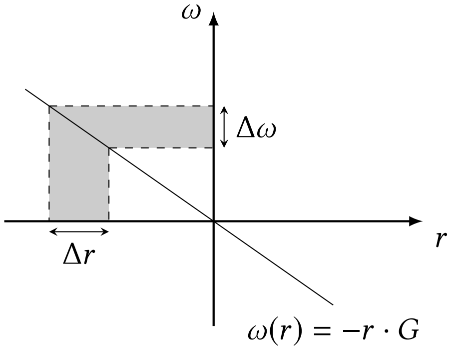

Figure 1.11: *Spatial variation of the Larmor frequency in the presence of a magnetic field gradient.*
A linear gradient G alters the Larmor frequencies of isochromats along the direction of the gradient. A frequency band $\Delta\omega$ therefore corresponds to a length Δr in that direction.

ally acquires a phase relative to a vector rotating with the unaltered Larmor frequency ω_0:

$$\phi = -\int_0^t \Delta\omega_{\mathrm{d}} u = -\gamma \int_0^t \boldsymbol{G}(u) \cdot \boldsymbol{r}(u)\,\mathrm{d}u \tag{1.18}$$

$$= -\gamma \cdot r \cdot G \cdot t \qquad \text{for } \boldsymbol{G}(t) = G \text{ and } \boldsymbol{r}(t) = r. \tag{1.19}$$

This leads to a dephasing of isochromats in the presence of gradients and with that to a decay of transversal magnetization.

1.3.2 Echoes

As described above, there are several mechanisms causing a decay of transversal magnetization. This decay can be rather quick even in biological samples, which is why echoes are used to reverse parts of this effect to gain more time for signal acquisition.

1.3.2.1 Spin Echo

Spin echoes [86] are used to reverse the dephasing of isochromats that lead to the decay of an FID with T_2^*. After excitation, isochromats with a precession frequency lower than ω_0 rotate in the $x'y'$-plane slower than isochromats with a precession frequency higher than ω_0. By irradiating a 180° pulse a time $T_\mathrm{E}/2$ after the excitation pulse, the system is mirrored, so that the slower isochromats end up in front of the faster ones. These therefore catch up with them and rephase the ensemble. The maximum transversal magnetization is reached again after an additional time $T_\mathrm{E}/2$, making T_E, the *echo time*, the duration between the excitation and the echo. The signal strength of this echo decays with T_2, since the statistic processes of the T_2-relaxation can not be reversed (cf. fig. 1.12).

1.3.2.2 Gradient Echo

Gradients that are present after an excitation provide a different mechanism of decaying the signal by dephasing the magnetization vectors along the direction of the gradient. This effect can be retracted by applying a second gradient of reversed polarity, thereby inversing the relative precession frequencies, so that the magnetizations along the gradient direction meet again. The echo forms at the time, at which the area of the rephasing gradient matches the area of the first one (cf. eq. (1.18)). Gradient echoes can not unwind the effects of transversal relaxation, since these are based on magnetic field inhomogeneities. The signal strength of the echo hence decays with T_2^*.

1.3.3 Spatial Encoding

To use NMR for tomography, signals originating from different volume elements in the investigated probe have to be distinguished. This spatial encoding is done by three procedures, that are combined to achieve a spatial encoding in all three dimensions. The fundamental principle of all these procedures is the variation of the resonant frequency of the isochromats in different regions of the investigated probe (cf. section 1.3.1.2).

1.3.3.1 Selective Excitation

Without loss of generality, the selective excitation is performed along the z direction. If a gradient G_z along that direction is present during the irradiation of an RF pulse with finite bandwidth, only those volume elements whose Larmor frequency match a frequency within the pulse's bandwidth are excited (cf. fig. 1.11), leading to an excitation of a confined slice. The signal acquired from that slice is then further encoded to get a three-dimensional spatial resolution. A widely used RF pulse has the shape of a truncated sinc. It's Fourier Transformation has a nearly rectangular shape, therefore, the excited slice is well defined.

After the excitation, the magnetization vectors along the z direction have different phases due to the varying Larmor frequencies in the time the gradient was present (cf. eq. (1.19)). To compensate for this, an additional gradient in opposite direction with half the slice selection gradient's length[2] is applied, effectively re-phasing the magnetization vectors.

---

[2] More precisely, the area under the gradient has to be equal to half the original gradient's area.

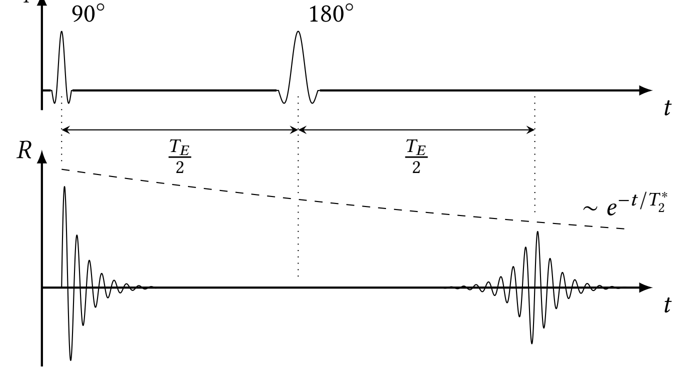

Figure 1.12: *Generation of a spin echo.*
Irradiating a 180° pulse a time $T_E/2$ after the 90° pulse reverses the dephasing of the isochromats' magnetization vectors and rephases them. This creates an echo with a maximum amplitude at the time T_E. Since this rephasing only reverses the T_2^* decay, but not the statistical T_2 decay, the amplitude of the echo is smaller then the one of the initial FID.

1.3.3.2 Frequency Encoding

Frequency encoding is achieved by applying a gradient G_x along for instance the x-direction while measuring the signal of the rotating transversal magnetizations. The such achieved spatial dependence of the measured signal (cf. section 1.3.1.2) can be used to distinguish the signals after Fourier Transformation.

1.3.3.3 Phase Encoding

The remaining y-direction is encoded by varying the phase of the signals. To do so, a gradient G_y in that direction is applied for a distinct time *before* the read-out begins. While this gradient is present, isochromats along the y-direction obtain different phases according to eq. (1.18). After the gradient is switched off, this spatial modulation of the phasing is preserved, so that during the read out at a later time the measured signal includes this phasing. By alternating several phase encoding steps with varying gradient strengths (and therefore different modulations of the phasing) with read out events, several signals with different phasing can be obtained, from which the signals of different volume elements along the y direction can be calculated.

1.3.4 Pulse Sequences

A series of RF pulses, gradient waveforms and data acquisition times to obtain the NMR signal is called a pulse sequence. By combining the above described techniques in a smart way, the magnetization can be manipulated to produce a specific signal, creating an image in the desired fashion. Two frequently used pulse sequences are the spin echo (SE) and the echo planar imaging (EPI). A substantial overview of common imaging sequences can be found in [87].

In the SE, a spin echo is created after excitation (cf. section 1.3.2.1). During this echo, the signal acquisition takes place in combination with frequency-encoding (cf. section 1.3.3.2). The time in between the excitation and the echo is used implement one phase encoding step (cf. section 1.3.3.3). This scheme is repeated until the desired number of phase encoding steps is reached.

In EPI, all phase encoding steps are performed after one excitation pulse. To do so, it is followed immediately by a fast train of gradient echoes (cf. section 1.3.2.2). Every echo is used as a read-out event combined with frequency encoding (cf. section 1.3.3.2). In between two gradient echoes a short additional gradient[3] is inserted, creating a different phase encoding for the next echo. Since the signal after the excitation decays quickly with T_2^*, the gradients have to be very short and be switched on and off very quickly. Nevertheless, signal to noise ratio in EPI is substantially lower than in SE, in exchange for a very short acquisition time.

---

[3] called “blip”

1.3.5 Motion Sensitive Imaging

Apart from spatially modulating the signal, magnetic field gradients can be used to encode motion into the phase of the signal. By expanding an arbitrary trajectory $\boldsymbol{r}(t)$ of an excited isochromat into a Taylor series, eq. (1.18) yields

$$\phi(t) = -\gamma \int_0^t \boldsymbol{G}(u) \cdot \left(\boldsymbol{r}_0 + \boldsymbol{v}_0 u + \frac{1}{2} \boldsymbol{a}_0 u^2 + \dots \right) \mathrm{d}u. \tag{1.20}$$

By introducing the n-th gradient moment as $\boldsymbol{m}_n(t) = \int_0^t \boldsymbol{G}(u) u^n \, \mathrm{d}u$, eq. (1.20) can be decomposed into a moment expansion:

$$\phi(t) = \gamma \left(\boldsymbol{m}_0 \cdot \boldsymbol{r}_0 + \boldsymbol{m}_1 \cdot \boldsymbol{v}_0 + \frac{1}{2} \boldsymbol{m}_2 \cdot \boldsymbol{a}_0 + \dots \right). \tag{1.21}$$

Considering a bipolar gradient form, which comprises two lobes of equal area but opposite polarity, the total area A of the gradient form is zero and therefore $\boldsymbol{m}_0 = 0$. By integrating over the whole gradient waveform, the first moment becomes $\boldsymbol{m}_1 = A\Delta \cdot \hat{\boldsymbol{r}}_\mathrm{G}$, where Δ is the time between the starts of the two lobes and $\hat{\boldsymbol{r}}_\mathrm{G}$ is the unit vector in the direction of the gradient. For the acquired phase at the end of the bipolar gradient lobes, this yields

$$\phi = \gamma A \Delta v_r. \tag{1.22}$$

The phase of the isochromat is therefore a measure for its mean velocity v_r in the direction of the gradient. When reconstructing an image based on the phase of the spatially encoded signals instead of the magnitude, one obtains an imaging contrast based on the motion of the individual volume elements.

By choosing appropriate gradient lobes, different moments can be nulled and, thus, higher moments of motion can be observed. A three-lobed gradient waveform for example can be used to create an acceleration phase contrast. However, these gradient lobes take up considerable more time than the bipolar one.

For arbitrary trajectories with non negligible changes in accelerations on the time scale of the gradient's length, these waveforms do not yield a phase that corresponds directly to the isochromat's motion.

1.4 Anatomical Terms of Location

In medical imaging, the Digital Imaging and Communications in Medicine (DICOM) standard [88] has been established to handle and transmit medical information. This standard uses a common right-handed coordinate system, the Dicom Patient Coordinate System (DPCS), that is defined as follows:

x-axis: Increases from the right hand side (R) to the left hand side (L) of the patient.

y-axis: Increases from the anterior (A, frontal) to the posterior (P, back) side of the patient.

z-axis: Increases from the caudal (foot) to the cranial (head) side of the patient.

In anatomy, three basic anatomical planes are used to describe locations of structures. Using the DPCS, they are defined as:

Transverse plane The xy-plane, cutting the body into a head and a foot part.

Coronal plane The xz-plane, dividing the body into a frontal and a back part.

Sagittal plane The yz-plane, cutting the body into a right and a left part.

It is convention that transverse images in computed tomography and MRI are displayed so that the left side of the patient is shown on the right side and vice versa. The anterior side is shown on the upper side of the image, the posterior side at the bottom. This way, slices are viewed as if the patient was lying on its back with the feet towards the viewer. All images shown in this thesis will follow this convention.

The DICOM standard stores information of the position and orientation of the image relative to the reference coordinate system of the scanner. The reference system is the DPCS with an arbitrary set origin, that is defined by the scanner. In an image, pixels are addressed by their column and row index (r resp. c). The origin ($r = 0, c = 0$) of the image is the upper left corner. The `ImagePositionPatient` field stores the position $\boldsymbol{S}$ of the image's origin in the reference frame. The orientation of the unitvectors of the columns ($\hat{\boldsymbol{e}}_c$) and rows ($\hat{\boldsymbol{e}}_r$) of the image is stored as `ImageOrientationPatient`. Additionally, the spacing (Δc and Δr) of adjacent pixels is stored as `PixelSpacing`. These definitions are illustrated in figure 1.13.

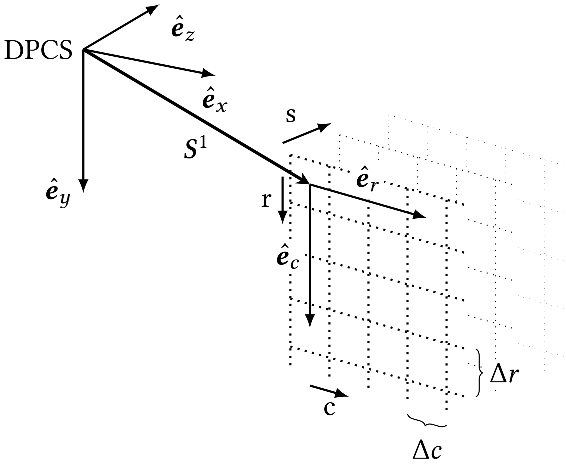

Figure 1.13: *Pixel data and Dicom Patient Coordinate System.*
A pixel's position in the three dimensional pixel data of a dicom set is identified by the three indices r, c and s. It's center's position in the DPCS is determined by the unitvectors $\hat{\boldsymbol{e}}_r$ *and* $\hat{\boldsymbol{e}}_c$ *and the translation vector* $\boldsymbol{S}$ *between the origins of the DPCS and the image data.*

In the case of a three-dimensional data set, that is a set of different slices of the same volume, the slice of a pixel is addressed by the slice index s. The unit vector in slice direction can be found as the scaled difference of the position vectors $\boldsymbol{S}^1$ and $\boldsymbol{S}^N$ of the first and last slice of the ordered image set. A robust way of ordering an image set with respect to the position in the slice direction is to calculate the inner product of the normal vector in slice direction $\boldsymbol{n}$ with the position S of each image's origin. $\boldsymbol{n}$ can be found as $\boldsymbol{n} = \hat{\boldsymbol{e}}_c \times \hat{\boldsymbol{e}}_r$ [cf. 89].

The position (x, y, z) in mm in the DPCS of a pixel (r, c, s) in the pixel data of a DICOM file or set can finally be calculated using the affine transformation between those two coordinate systems [cf. 88, sec. 3.C.7.6 and 3.10.7.1.1]:

$$\begin{pmatrix} x \\ y \\ z \\ 1 \end{pmatrix} = \begin{pmatrix} \hat{\boldsymbol{e}}_{c,1} \cdot \Delta r & \hat{\boldsymbol{e}}_{r,1} \cdot \Delta c & \boldsymbol{k}_1 & S^1_1 \\ \hat{\boldsymbol{e}}_{c,2} \cdot \Delta r & \hat{\boldsymbol{e}}_{r,2} \cdot \Delta c & \boldsymbol{k}_2 & S^1_2 \\ \hat{\boldsymbol{e}}_{r,3} \cdot \Delta r & \hat{\boldsymbol{e}}_{r,3} \cdot \Delta c & \boldsymbol{k}_3 & S^1_3 \\ 0 & 0 & 0 & 1 \end{pmatrix} \cdot \begin{pmatrix} r \\ c \\ s \\ 1 \end{pmatrix}, \tag{1.23}$$

$$\text{with } \boldsymbol{k} = \begin{cases} \boldsymbol{0} & \text{for a single slice,} \\ \frac{1}{1-N}\left(S^1 - S^N\right) & \text{for } N \text{ slices.} \end{cases}$$

1.5 Phase Unwrapping

In this thesis, data is collected by reconstructing phase images. In these, phase wraps occur naturally, that need to be unwrapped before further post-processing may take place.

1.5.1 Basic Principles

Phase is measured against a reference phase in the range of 2π. If the original phase exceeds these limits, the measured phase will be wrapped back into this range, creating discontinuities in the data (cf. fig. 1.14). These discontinuities can be eliminated using so-called phase unwrapping algorithms. This section provides a short introduction of the mathematical background for the phase unwrapping methods used during the course of this thesis. The mathematical descriptions are mostly taken from [90].

In the obtained phase data, the original phase ϕ will be wrapped to the interval $[0, 2\pi)$. The measured phase ψ can then mathematically be described as

$$\psi(n) = \mathcal{W}(\phi(n)) = \phi(n) + 2\pi k(n), \tag{1.24}$$

with $k(n)$ as an integer function and $\mathcal{W}$ as a wrapping-operator. By unwrapping the measured phase one tries to receives an estimation of the true phase ϕ.

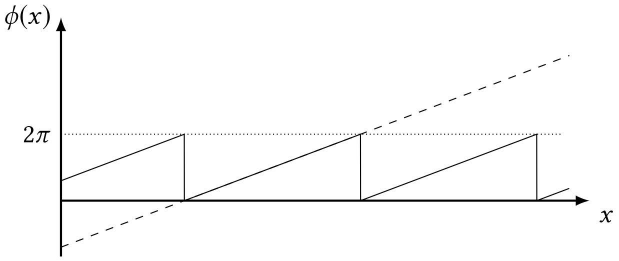

Figure 1.14: Original (dashed) and measured (solid) phase of a phase signal exceeding the range of 2π.

Since ϕ is not measured continuously but is sampled, the true signal is - in the one-dimensional case - an array ϕ_n. If there are no phase differences between samples of more than $|\Delta\phi| \leq \pi$, the relation $\Delta\phi_n = \mathcal{W}(\Delta\psi_n)$ is valid for every n. The array can then be unwrapped by choosing an initial value $\phi_0 = \psi_0$ and summing up the wrapped phase differences [91].

Extending this concept to the two-dimensional case that is present in MRI, the true phase $\phi_{m,n}$ at pixel (m, n) can be determined by integrating along a path C over the entire sampled phase image:

$$\phi_{m,n} = \sum_{C} \left[\mathcal{W}\left(\Delta_x \psi_{i,j}\right) + \mathcal{W}\left(\Delta_y \psi_{i,j}\right) \right] + \phi_0 \tag{1.25}$$

with

$$\Delta_x \phi_{i,j} = \phi_{i+1,j} - \phi_{i,j}, \qquad \Delta_y \phi_{i,j} = \phi_{i,j+1} - \phi_{i,j}. \tag{1.26}$$

The smoothness condition in the two-dimensional case is given by

$$\left|\Delta_x \phi_{i,j}\right| \leq \pi \quad \text{and} \quad \left|\Delta_x \phi_{i,j}\right| \leq \pi. \tag{1.27}$$

If this condition is violated at any position in the sampled phase image, the integration result will depend not only on ϕ_0, but also on the path C chosen. The unwrapping is path-independent only if $\sum \left[\mathcal{W}(\Delta_x \psi_{i,j}) + \mathcal{W}(\Delta_y \psi_{i,j}) \right] = 0$ holds for every closed path[4]. Positions that yield non-zero values are called residues. They can take values (or “charges”) of $\pm 2\pi$. If an integration path encircles several residues, these might balance out with a total charge of zero. In this case the result is not influenced by these “balanced residues”.

1.5.2 Algorithms

In the course of this thesis, phase unwrapping was done using so-called path-following algorithms, that determine an integration path that does not encircle any unbalanced residues. The main challenge for these algorithms is to find an optimal path that meets this requirement and still covers all pixels so that no separate regions arise in the image. Three algorithms have been used, that will be shortly discussed in the following section. All algorithms were implemented based on pseudo-code from Ghiglia and Pritt [90].

1.5.2.1 Goldstein’s Algorithm

Goldstein, Zebker and Werner’s algorithm [92] balances residues in the phase image by connecting those of opposite polarity with so-called branch cuts. When the image is unwrapped, the integration path is not allowed to cross any branch cuts, therefore rendering the result independent of the actual path chosen.

To detect residues in the sampled phase image, the smallest closed path (2 × 2 pixels) around every intersection of four pixels is investigated.

---

[4] There are several equivalent conditions, too.

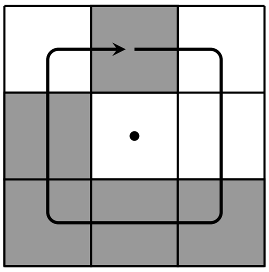

Figure 1.15: *Test for mask connectivity.*
Masked pixels are filled in gray, non-masked ones are in white. The number of transitions between mask and nonmask pixels in the 3 × 3 neighborhood of the current masked pixel (indicated by the dot) is counted. Here two transitions occur along the indicated path: one from top to top-right, and one from right to bottom-right. The top-left pixel does not add transitions, because the mask is connected diagonally.

The found residues are then used to create branch cuts. To do so, a box of size 3×3 is placed around a residue. This box is increased until it contains another residue, at which point both are connected by a branch cut. This is repeated with boxes of increasing size for all residues connected to the current branch cut, until either the sum of charge of all connected residues becomes zero, or the box touches the border of the phase image. In this case a branch cut is placed to that border.

This process is then repeated until all residues in the phase image are balanced. The actual unwrapping of the phase image is done by starting at a single pixel that is not a branch cut and consecutive unwrapping of neighboring pixels while avoiding branch cuts.

As a preprocessing step to this algorithm, neighboring residues of opposite polarity were eliminated [cf. 93] to achieve a higher quality of the generated branch cuts.

1.5.2.2 Mask Cut Algorithm

The mask cut algorithm [94] works very similar to Goldstein's algorithm. The placement of branch cuts is however guided by a quality map to guide the placements of branch cuts. The quality map assigns a value to each pixel that describes the "goodness" of the phase value of this pixel. Throughout this thesis, the used quality map was the phase derivative variance, that will be explained later (section 1.5.2.4).

The algorithm starts at a single residue in the sampled phase image and grows a mask along the pixels of lowest quality, until either the charge of all connected residues is balanced, or the mask grows into the border of the image. This procedure is repeated until all residues are balanced out.

The created masks naturally tend to be thick, since the path along the lowest quality is not necessarily the shortest one between two residues. To reduce this effect, the masks are thinned in a second processing step [95]: Pixels of the mask are removed consecutively if this does not change the connectivity of the mask. This is tested in the 3×3 neighborhood of every masked pixel in the image: if the number of mask-nonmask transitions is no greater than two, the pixel can be removed (cf. fig. 1.15. This is repeated until the mask is minimized.

After successful thinning of the masks, the sampled phase image is unwrapped while ignoring masked pixels.

1.5.2.3 Quality Guided Algorithm

This algorithm [90, 96] uses a quality map (again, throughout this thesis, the phase derivative variance was used) to determine an ideal integration path during the phase unwrapping without a special treatment of residues. The implementation used here was done after the pseudo-code in .

The phase unwrapping is started at the pixel with the highest quality of the image. Then the pixel with the highest quality neighboring an already unwrapped pixel is unwrapped consecutively. This does not guarantee that the integration path may not encircle residues, but makes it unlikely, assuming that phase inconsistencies arise most likely at pixels of lower quality.

In advantage to Goldstein's algorithm and the mask cut algorithm, this one does not rely on branch cuts and therefore never creates disconnected regions in the phase image.

1.5.2.4 Phase Derivative Variance

The phase derivative variance [97] was used to create quality maps for the mask cut and the quality guided algorithms. It is the root-mean-square measure of the variance of the wrapped phase differences in x- and y-direction. For the pixel (m, n) it is calculated as

$$z_{m,n} = \frac{\sqrt{\sum_{i,j}(\Delta_x\psi_{i,j} - \overline{\Delta_x\psi}_{m,n})^2} + \sqrt{\sum_{i,j}(\Delta_y\psi_{i,j} - \overline{\Delta_y\psi}_{m,n})^2}}{k^2}, \tag{1.28}$$

where the indexes i and j range over a $k \times k$ window centered at the pixel and $\overline{\Delta_{x/y}\psi}$ is the average of the corresponding derivatives in the windows. Assuming that the phase gradients tend to be large in the presence of noisy phase data, the phase derivative variance is a measure of "badness" of individual pixels. To create a quality map of "goodness" for the quality guided algorithm, the reciprocal values were used.

2 Experimental Methods

In this chapter, the basic idea of Magnetic Resonance Rheology (MRR) is introduced and the technical realization is described. At the end of the chapter the preparation of agar based phantoms and the measurement protocols both for these phantoms and for human subjects are described.

2.1 In vivo Creep Relaxation Experiment

In this thesis, human brain tissue is investigated by an in vivo creep relaxation experiment that was termed MRR [36, 37, 40]. The basic ideas behind this experiment are explained in the following.

As described in section 1.2.2, brain tissue can be regarded as a viscoelastic material. By comparison, the cranial bone can be regarded as a rigid solid during the course of this experiment. Suppose the subject rests on its back. The gravitational forces acting on the brain tissue $\boldsymbol{F}_\mathrm{G}$ and the restoring forces $\boldsymbol{F}_\mathrm{R}$ of the tissue will then be in equilibrium. If the head is accelerated downwards for a short time, this equilibrium is disturbed. In the reference system of the head, the gravitational forces are reduced, leading to an acceleration of the volume elements of the brain tissue evoked by the unaltered $\boldsymbol{F}_\mathrm{R}$. The brain tissue therefore deforms. When the head lands, the gravitational forces are fully restored. Additionally, the now deformed tissue is further excited by the deceleration forces.

The excitation forces will propagate through the brain volume as compressional waves with the sound velocity of the tissue, which will be similar to the one of water ($v \approx 1500\,\mathrm{m/s}$). Compared to that, the shear deformations of the tissue will only slowly return to the original state of equilibrium. We can therefore assume the whole brain volume is instantly excited globally.

Since the excitation forces act only for a short time, we may treat them as a narrow step function. Hence, a broad band of frequencies will be excited in the brain tissue. Of those, only the resonance frequencies will not be damped out quickly. One therefore expects the tissue response to the excitation to be an oscillation in the local resonance frequencies which in general depend on the boundary conditions and the mechanical properties of the tissue. Local inhomogeneities in those mechanical properties will therefore lead to different local trajectories of the tissue's volume elements, and therefore to strain.

In MRR, the local trajectories of the tissue elements after the excitation by a short drop of the head are measured using motion sensitive MRI (cf. section 1.3.5). The following sections will therefore explain in detail how the controlled downward motion of the head inside an MRI scanner is achieved and how the resulting trajectories are measured using the MRI system.

2.1.1 Experimental Setup

During the course of this thesis, several prototypes have been developed with the aim of performing the above introduced creep experiment which have been described in detail in [40]. In the following sections, therefore, only the latest version of the prototype will be explained in detail. All measurements presented in this thesis were performed with this system.

The downward motion was induced and controlled by a lifting device fitting into the head coil[1] of the used MRI scanner[2]. The actual motion was controlled by a pneumatic system and monitored optically. An overview over these components is shown in fig. 2.1. They will be described in detail below.

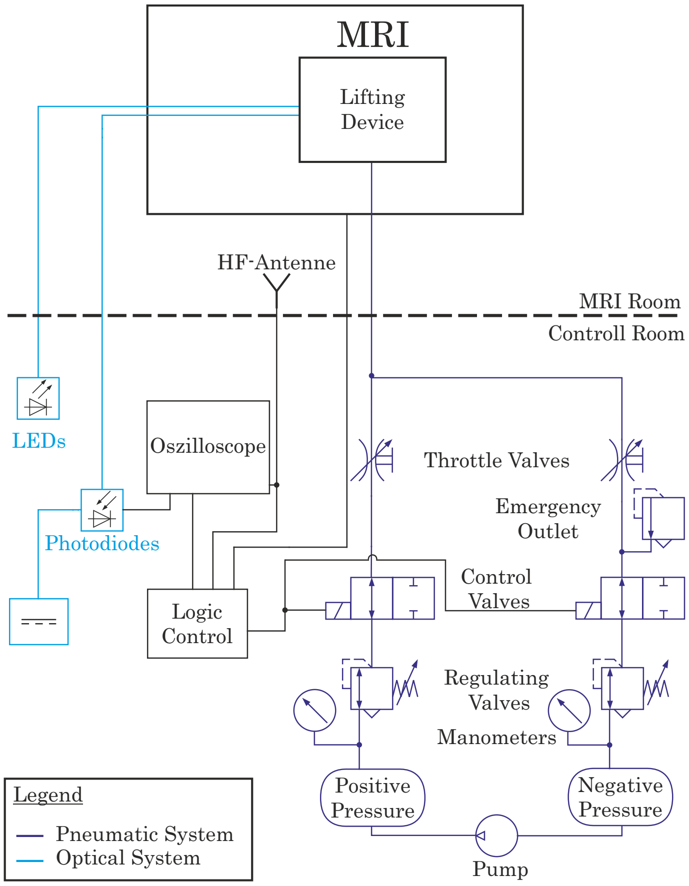

Figure 2.1: *Overview of the experimental setup.*
The lifting device is located in the head coil of the MRI scanner. The pneumatic control with the control valves and the pressure tanks are indicated in dark blue. All these components are located in the control room of the scanner. The pneumatic system is triggered by an optical signal of the control computer of the MRI scanner that was processed by the logic unit. The optical position monitioring is indicated in light blue. The LED and the photo diodes are positioned in the control room as well. The light is transmitted to the lifting device by optical fibers. The recording of the optical position monitioring data was triggered by an antenna signal that depicted the RF pulses of the MRI. [modified from 98]

2.1.1.1 Lifting device and pneumatic system

The self-made lifting device and its components are visualized in figure 2.2. It consisted of a baseplate and a half ring made out of Polyoxymethylene (POM) fitting tightly into the

---

[1] Head Matrix Coil, Siemens Healthcare

[2] MAGNETOM Avanto 1.5 T, Siemens Healthcare

head coil of the used MRI scanner. Two pneumatic rubber hoses were positioned on top of the baseplate, with an open end connected to openings in the half ring. Above the hoses a movable shell was positioned that held the patients head. To ensure a lightweight design while allowing for a high rigidity, the shell was constructed as a sandwich-structured composite. The sandwich was made of two outer layers of aramid fiber-reinforced plastic[3] encasing a 3 mm thick honeycomb core of aramid paper[4]. The shell was connected to the half ring via four flat springs made of fiberglass. These realized a linear bearing to ensure a precise vertical motion of the shell. To limit the maximum height of the shell, four flat headed screws made from POM were tightened from below through the baseplate into threads laminated into the shell.

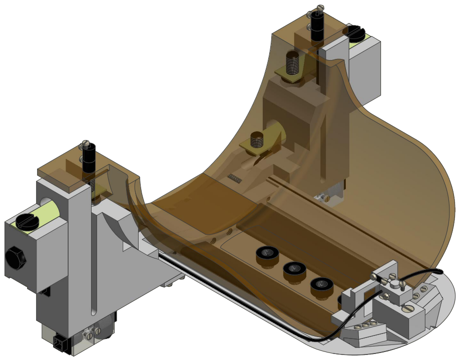

Figure 2.2: *Sketch of the lifting device. The half ring and the baseplate are shown in grey. [40]*

The lifting and lowering of the shell was done by filling the rubber hoses with air and venting them. The hoses were connected via plugs in the half ring to a pneumatic system located outside of the examination room. It consisted of two pressure tanks of approximately each 10 L. A membrane pump[5] constantly produced an overpressure in the one and an underpressure in the other tank, each compared to the ambient pressure. The pressures were controlled via two pressure regulating valves. Both tanks were connected via electronically operated control valves to a common piping wiring leading to the lifting device. The flow in both pipes could be controlled individually by throttle valves.

In normal position, the control valve in the overpressured branch was open, while the other one was closed. Therefore, the shell was in an upper position by default. The motion of the shell was induced by an optical trigger signal of the control computer of the MRI scanner. The optical signal was converted into a voltage signal[6], used to create a transitor-transistor-logic (TTL) pulse in a time-logic module[7] and directed to a digital delay generator[8] that was used to create delays with a sub-millisecond precision. A delayed TTL pulse was transmitted to the gate and delay generator again, where a TTL

---

[3] fabricated using woven Kevlar®49 T (Style 284, ECC, C. Cramer GmbH & Co. KG, Heek, Germany) and Epoxydharz und Härter L (R&G Faserverbundstoffe GmbH, Waldenbuch, Germany)

[4] R&G Faserverbundstoffe

[5] Vacuubrand, MZ2D, Vacuubrand GmbH & Co. KG, Wertheim, Germany

[6] optical sensor OPT101P, Texas Instruments, Dallas, Texas, USA

[7] NIM Dual Gate and Delay Generator Modell 222, LeCroy, Chestnut Ridge, New York, USA

[8] Digital Delay Generator 7020, Berkeley Nucleonics Corporation, San Rafael, California, USA

pulse of distinct length was created to toggle the control valves. The duration of the pulse determined how long the overpressure and underpressure control valves where closed respectively opened. During the experiments conducted through the course of this thesis, the pulse length was approximately 700 ms to ensure the shell only moving back into the upper position after all measurements were finished.

2.1.1.2 Motion monitoring

The motion of the shell was measured optically with three optical position monitiorings (OPMs), one on each the head's left and right side towards the inferior side of the lifting device (from now on called left and right), and one centered at the superior side of the device (called superior). Those OPMs consisted of two optical fibers facing each other with a small gap (≈0.3 mm). Light emitted by a red light-emitting diode (LED) was conducted through one optical fiber and collected again by the second one. In the gap, a diagonally shaped slit attached to the shell moved, screening off parts of the light (see fig. 2.3). The collected light was conducted to a photo diode and the voltage generated there was measured using an oscilloscope. The optical fibers were permanently installed in the baseplate. Connectors were present to plug in lengthier fibers to connect the diodes positioned outside of the examination room. It has been shown in [40] that the measured voltage is proportional to the height of the shell over a great range.

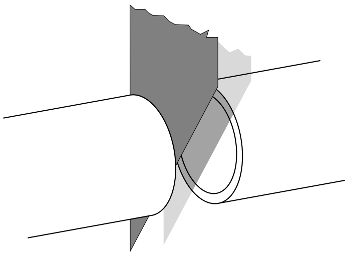

Figure 2.3: *Functionality of the optical measurement system: A diagonal slit that is attached to the shell moves in a small gap in the optical fibers. It therefore shades part of the light that is emitted by the one fiber and illuminates the face of the other one. The gap is not sketched in true scale.*

To know the time response of the shell motion relative to the MRI imaging sequence, the RF pulses of the scanner were collected using a broadband antenna in the examination room. The coaxial cable used to connect the antenna was wrapped around a circular ferrite core. This acted as a choke to suppress the introduction of unwanted signals into the examination room. The antenna signal was amplified, integrated and discriminated, and used as trigger signal for the oscilloscope.

If for a measurement not only the qualitative progression of the shell motion, but the actual position in physical units was needed, the OPMs were gauged prior to the measurement. This step took place after loading the lifting device and directly prior to the actual measurement to minimize the risk of involuntary readjustment of the optical fiber connectors which would alter the transmitted light intensity. The vertical distance between the shell and the baseplate of the lifting device was calipered at locations near to the ones of the OPMs both in the elevated and the deaerated position of the shell. Together with the voltages of the photo diodes at the corresponding heights of the shell this was used to calibrate the optical system (cf. section 3.1.1 for details).

2.1.2 Motion Sensitive MRI Sequence

The MRI sequence used to measure the movement occurring during the drop experiment (“nin_ep2d_diff_vb10r”) has been programmed and provided by Dr. Jürgen Finsterbusch[9] [99]. It is a motion sensitive SE-EPI sequence. Its functionality is illustrated in fig. 2.4 and will be explained in the following. For details on the individual components see section 1.3.

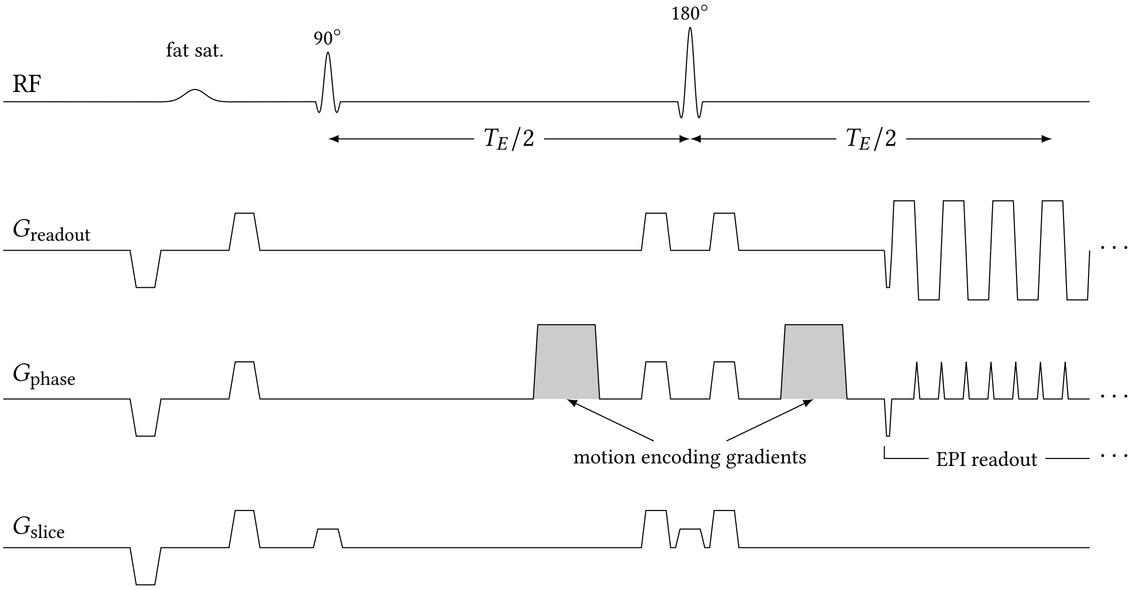

Figure 2.4: *The “nin_ep2d_diff_vb10r” sequence:*
The imaging sequence is based on a standard SE-EPI sequence. The additional motion encoding is realized by adding two gradients on either side of the 180° *pulse. The EPI read out echo train starts after the second motion encoding gradient. The center of that echo train is located at the peak of the echo at* T_E. *Note that due to this fact, the motion encoding gradients are not necessarily positioned symmetrically around the* 180° *pulse with small echo times. To minimize imaging artifacts, a fat saturation pulse is added prior to the* 90° *pulse, and both this and the* 180° *pulse are surrounded by crusher gradients in every spatial direction to get rid of unwanted magnetizations. Note that the schematic is not sketched in true scale!*

The sequence used a 180° pulse after the slice selecting and exciting 90° pulse to create a spin echo at the time T_E after the excitation pulse. During this echo, EPI read out was used to spatially encode the signals of the imaging plane (cf. section 1.3.4).

To reduce imaging artifacts due to the different Larmor frequencies of fat and water, the sequence included a fat saturation pulse prior to the excitation pulse. To further reduce artifacts due to the excitation of remaining transversal magnetization, crusher gradients in every direction were added symmetrically around the fat saturation and the 180° pulse.

The motion sensitivity of the sequence was achieved by adding two trapezoid motion encoding gradients (MEGs) [100]. These are unipolar gradients in y-direction at either

---

[9] University Medical Center Hamburg-Eppendorf, Department of Systems Neuroscience

side of the 180° pulse. Since this pulse inverts the spin system, the effect of these two gradient lobes on an isochromat is exactly equal to the one of a bipolar gradient form as explained in section 1.3.5: If the isochromat moves in between both gradient forms, its phase will accumulate an offset according to (1.18). In this way the sequence encoded all motion of excited isochromats in the direction of the gradients that took place in between the two gradient lobes. Since the phase offset is not only dependent on the trajectory of the isochromat but also of the shape of the gradient form, quantities to describe these have been established (cf. [87] and the illustrations in fig. 2.5): The length of one trapezoid gradient lobe is defined as the time δ from the beginning of the rising flank of the gradient to the end of the plateau. The length of the rising flank is described by the parameter ζ. The interval between both gradient lobes is defined by the time Δ between the centers of both lobes. Apart from ζ these parameters could be adjusted by the user. For the MRI system used, ζ seemed to be fixed to the minimal value of 0.361 ms. Due to historical reasons, the gradients' strength G could not be adjusted directly. Instead, the b-value[10] was used to adjust G dependent on the other parameters. For trapezoidal gradients, it is defined by

$$b = \gamma^2 G^2 \left(\delta^2 \left(\Delta - \frac{\delta}{3} \right) + \frac{\zeta^3}{30} - \frac{\delta \zeta^2}{6} \right). \tag{2.1}$$

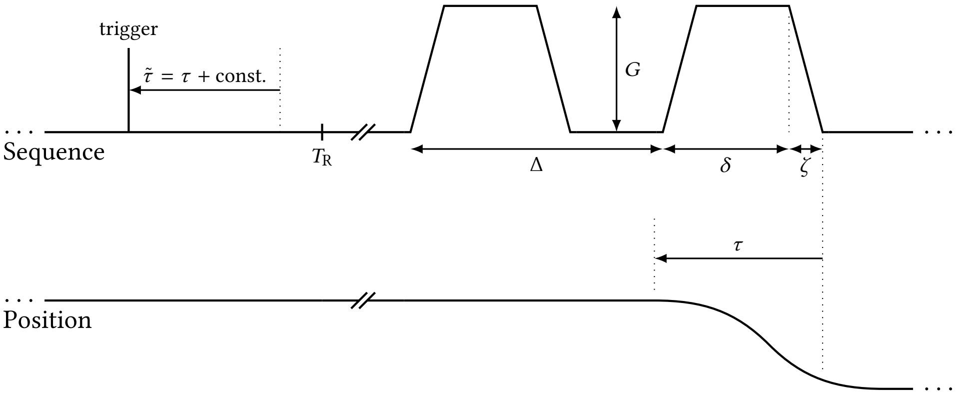

***Figure 2.5:** Characteristic parameters of the motion sensitivity:*
The form of the motion encoding gradients is described by the length δ of a single trapezoid gradient, the length ζ of one flank of such gradient, the time Δ between the starts of the first and the second gradient, and the gradients' strength G.
The start of the falling motion of the shell is characterized by the parameter τ describing the time between the end of the second gradient and the beginning of the falling motion. The motion is triggered near the end of the previous *run of the sequence and can be shifted by the amount $\tilde{\tau}$.*

---

[10] Such gradients were first used in diffusion measurements, where the attenuation of the signal is described by the product of b and the diffusion coefficient D

2.1.2.1 Motion sampling

To describe the start of the falling motion of the shell in relation to the sequence, the parameter τ was defined (cf. fig. 2.5) as the time from the end of the second MEG (t_2) to the beginning of the falling motion. τ therefore describes the variation in time of the motion with the origin being the start of the excitation. Negative values of τ describe measurements where all motion encoding was finished before the falling of the shell started. Using eq. (1.18) and the fact that τ effectively shifts the trajectory of the motion relative to the time axis of the gradients, the phase of an isochromat with trajectory $\boldsymbol{r}$ after a measurement with a specific τ is given by

$$\phi(\tau) = \phi_0 + \gamma \int_{t_1}^{t_2} \boldsymbol{G}(t) \cdot \boldsymbol{r}(t+\tau)\,\mathrm{d}t, \tag{2.2}$$

with an arbitrary constant phase ϕ_0. $\boldsymbol{G}(t)$ describes the form of all gradients of the imaging sequence and is assumed to be non-zero only for $t \in [t_1, t_2]$. By performing measurements at different τ, the complete trajectory of the probe material during the experiment could be investigated, provided the trajectory could be reproduced accurately for every measurement.

To synchronize the induced motion of the probe with the imaging sequence, a variable trigger signal was added near the end of the sequence, that was for this reason called post trigger (PT). Since the trigger was positioned at the end of the sequence, the motion measured during one run of the imaging protocol was triggered by the *prior* run. The position of the PT relative to the end of the sequence was defined by the quantity $\tilde{\tau}$ called post trigger fill time (PTFT). The sequence additionally provided a mechanism to automatically sample the motion occurring during the drop experiment by performing several runs of the sequence in one imaging protocol. The PT could be shifted after every run, thereby realizing measurements with different τ. For that, an initial $\tilde{\tau}$ was defined, which was reduced over several runs of the sequence. The amount of time the trigger was shifted each time was controlled by the PTFT Decrement $\Delta\tau$. The number of runs with the same $\tilde{\tau}$ was controlled by the number of PTFT Averages N_τ. Since the motion was triggered by the prior run, the protocol effectively created $N_\tau + 1$ images with the first specified PTFT and $N_\tau - 1$ images of the last one. The number of shifts performed during one imaging protocol, and with that the minimal $\tilde{\tau}$ achieved, was determined by the total number of runs of the sequence. This could be set by specifying the amount of total averages N_{total} for the imaging protocol. The maximum value possible for N_{total} was 510. All fields were accessible using the standard MRI control software.

The value $\tau(\tilde{\tau} = 0)$ is controlled by adjusting the delay between the trigger detection and the toggling of the control valves of the pneumatic system (cf. section 2.1.1.1). Typically, the delay was tuned so that $\tau(\tilde{\tau} = 0)$ was slightly below 0 ms to make sure the beginning of the trajectories was sampled. Therefore, for all measurements presented in this thesis, $\tau \approx \tilde{\tau}$ apart from a small constant offset. Therefore, if not mentioned otherwise, only τ will be used throughout this thesis while keeping the potential offset in mind.

2.1.2.2 Sensitivity

Letting $\phi_0 = 0$ and neglecting the constant γ, (2.2) equals the convolution $\boldsymbol{r} * \boldsymbol{G}$ except for the sign of t in $\boldsymbol{r}$. According to the convolution theorem, this equals the multiplication of the Fourier transformed quantities:

$$\mathcal{F}(\phi) = \mathcal{F}(\boldsymbol{r} * \boldsymbol{G}) = \mathcal{F}(\boldsymbol{r}) \cdot \mathcal{F}(\boldsymbol{G}), \tag{2.3}$$

where $\mathcal{F}(\boldsymbol{r})$ and $\mathcal{F}(\boldsymbol{G})$ are the Fourier transforms of $\boldsymbol{r}$ and $\boldsymbol{G}$ respectively. Therefore, one expects limited sensitivity of MRR measurements at those frequencies where the spectrum of $\boldsymbol{G}$ has minimums, namely $\frac{1}{\delta}$ and $\frac{1}{\Delta}$ (cf. fig. 2.6).

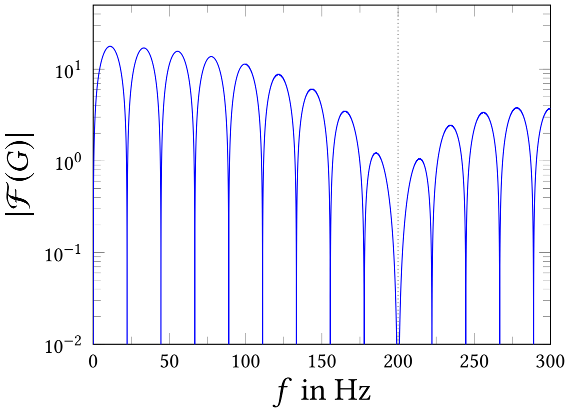

Figure 2.6: *Frequency spectrum of a one-dimensional bipolar gradient waveform: The plot shows the Fourier spectrum of a numerically created bipolar gradient waveform* ($\delta = 5\,\mathrm{ms}$, $\Delta = 45\,\mathrm{ms}$, $\zeta = 0.361\,\mathrm{ms}$, *and* $G = 25\,\mathrm{mT/m}$. *The Fourier transformation has been computed using Fast Fourier Transformation. The spectrum has minimums at* $n \cdot \frac{1}{\delta}$ *and* $n \cdot \frac{1}{\Delta}$. *The dotted line shows* $\frac{1}{\delta}$.

2.1.2.3 Data storage

The recorded image data was stored in the format of the DICOM standard. For every run of the sequence that was performed, the magnitude data respectively the phase data of the magnetization were used to reconstruct two single images stored in separate DICOM files. Most imaging parameters were stored in the extensive header of this files as well. Additionally, all parameters needed to reconstruct the location of the MEG as well as the value of $\tilde{\tau}$ were stored in special fields within the private CSA header of DICOM files created by Siemens MRI scanners. An overview over these fields is provided in table A.3 in appendix A.2.

2.1.3 Coordinate Alignment

The trajectories of the measured volume elements during a drop experiment are encoded in the phase progression of the corresponding voxel. The position of those volumetric pixels (voxels) is known accurately in the DPCS. In order to interpret the phase progressions, it would be beneficial to know the motion of the shell in the same coordinate system.

The trajectory of the shell in the three-dimensional space can be reconstructed from the data of the three OPMs (see section 2.1.1.2). In order to transfer this trajectory into the DPCS, the position of the shell in the DPCS has to be known. Since the lifting device itself is not visible in MRI, vitamin E capsules were put into holders permanently fixed to the shell close to the locations of the OPMs. The capsules appear bright in T_2-weighted images due to a long T_2. Therefore, alignment scans were obtained prior to the actual measurements. Those scans were sets of coronal images with a spatial resolution of $0.3 \times 0.3\,\mathrm{mm}^2$ in the horizontal plane and a slice thickness of 3 mm (cf. fig. 2.7). One scan was obtained to find the two markers positioned dorsal left and right, and one additional scan was obtained to image the third marker positioned at the cranial end of the shell. Since the origin of the DPCS is the same for those scans and the later acquired motion sensitive images (assuming the alignment of the patient/probe was not changed in between), locating the signatures of the markers in the alignment scans provides a way to locate the shell in the DPCS.

For the analysis of these scans and the deduction of the position of the shell in the DPCS see section 3.1.2.

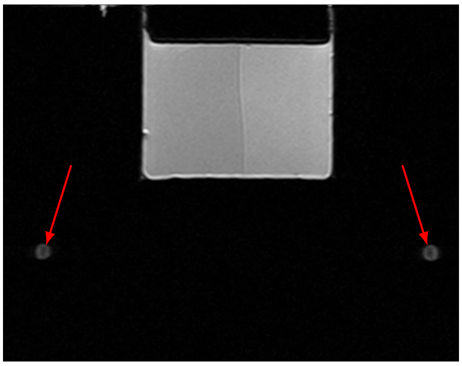

Figure 2.7: *Coordinate alignment of the lifting device: Shown is one slice of a set of transversal high-resolution turbo spin echo (TSE) images of a phantom loaded in the lifting device. Two vitamin E markers are visible posterior left and right. The location of those markers in the image set is used to determine the location of the lifting device and the optical position monitioring in the DPCS. Since the signal of the markers is weak compared to the one of the phantom's hydrogel, the positions of the two markers are indicated by a red arrow.*

2.2 Test Subjects

During the course of this thesis, measurements on tissue mimicking phantoms as well as on human subjects were performed to asses the feasibility of the measurement principle.

2.2.1 Tissue Mimicking Phantoms

The phantoms used were made out of an agar based hydrogel inside a container made from polymethyl methacrylate (PMMA), which is a common choice for such phantoms [cf. 22, 101, 102].

The phantom container had a length of 100 mm and a diameter of 127 mm. It was covered with two plates fitting accurately into the shell of the lifting device (cf. fig. 2.8). One of those plates could be removed to fill the container with the hydrogel. The inner surface of the container was lined with approximately 18 mm thick fine-pored open-celled sponge material on all faces. The inner surface of the material was sealed using a polymer sealant[11]. The sponge material was used to ensure a certain degree of mobility of the incompressible hydrogel without introducing different boundary conditions on individual surfaces. The volume filled with the hydrogel was therefore a cylinder with an

---

[11] Poly Max glasklar express, UHU GmbH & Co KG, Bühl, Germany

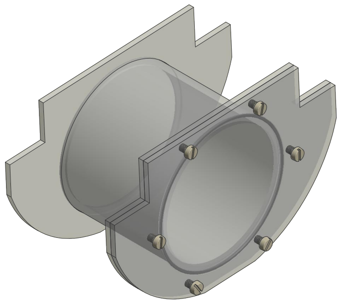

Figure 2.8: Phantom container.
The container was made from PMMA and shaped in such a way that it fit tightly into the movable shell of the lifting device. The inside of the container was lined with sponge material. [98]

approximate length of 64 mm and an approximate diameter of 90 mm, which corresponds to a volume of about 400 ml. Since such a phantom weights only about 400 g, the phantom was loaded with sandbags in the lifting device to match the weight of a typical head.

The hydrogel was produced in a similar fashion to the one described in [103]. The agar[12] was added into water and cooked while stirring constantly for 2.5 min. After that the fluid was cooled down in a water quench still under constant stirring to a temperature of about 42 °C. The fluid was then filled into the container and stored in a cool place until the gelling process was completed.

To adjust the mechanical properties of the gel, the agar concentration C was altered. The Young's modulus E of the gel subject to C roughly follows a powerlaw [102, 104]. For this work, the Young's modulus was estimated using the relationship provided in [102]:

$$E = 0.349\,\mathrm{kPa} \cdot \left(\frac{C}{\mathrm{g/L}}\right)^{1.87}. \tag{2.4}$$

The density of the agar hydrogel is $\rho_{\mathrm{agar}} \approx 1\,\mathrm{g/cm^3}$ for small agar concentrations. To alter this density, tungsten carbide powder[13] with an average particle size of 50 µm to 60 µm was added to the hot fluid after cooking it. The volume V_{WC} of tungsten carbide needed to realize a specific density ρ_{gel} of a hydrogel of volume V_{gel} can be calculated by

$$V_{\mathrm{WC}} = \frac{\rho_{\mathrm{gel}} - \rho_{\mathrm{agar}}}{\rho_{\mathrm{WC}} - \rho_{\mathrm{agar}}} \cdot V_{\mathrm{gel}}. \tag{2.5}$$

Tungsten carbide has a density of $\rho_{\mathrm{WC}} = 15.63\,\mathrm{g/cm^3}$. Therefore, to realize a hydrogel density of $\rho_{\mathrm{gel}} = 1.2\,\mathrm{g/cm^3}$, only a volume $V_{\mathrm{WC}} = 0.014 \cdot V_{\mathrm{gel}}$ of tungsten carbide is needed, corresponding to a mass of $m_{\mathrm{WC}} = 21.37$ g per 100 ml of hydrogel. Due to this small volume of added powder the elastic properties of the hydrogel should not be altered much. To prevent the powder from sedimenting, the heated fluid was stirred until the fluid was cooled down close to the gelling point before decanting it into the container. A temperature of 35 °C to 37 °C was found to be sufficient.

After all measurements with a phantom were performed, the density of the phantom material was measured using a pycnometer. For that, samples of approximately 1 cm³

---

[12] Agar-Agar Kobe I, Carl Roth GmbH & Co. KG, Karlsruhe, Germany

[13] Wolframcarbid DS 50, H. C. Starck GmbH, Goslar, Germany

were cut out and dissected into smaller pieces to fit through the neck of the pycnometer. The masses of the empty pycnometer m_0, the pycnometer filled with distilled water m_1, the pycnometer with the dissected sample m_2 and the pycnometer with the sample filled up with distilled water m_3 where measured. The density of the sample was then calculated via

$$\rho_{\text{sample}} = \frac{m_{\text{sample}}}{V_{\text{sample}}} = \frac{m_2 - m_0}{m_1 + m_2 - m_0 - m_3} \rho_{\text{H}_2\text{O}}. \tag{2.6}$$

In this thesis, homogeneous phantoms and two-layered phantoms will be presented. The layered phantoms each consisted of two differently produced layers. One phantom had two layers with equal densities but different agar concentrations and therefore different Young's modulus, the other one had two layers with equal agar concentrations but different densities. To fabricate these phantoms, approximately half the volume of the phantom container was filled with liquid agar hydrogel and cooled resting on the side of the container. When the gel was fully coagulated, the hydrogel was cut off at the top to make room for the sponge layer of the cover plate. After that, the second hydrogel for the second layer was cooked and filled in. The phantom container was then closed and stored in a cool place until the MRR measurement. The detailed parameters of these phantoms can be found in table 2.1. Details on the measured densities can be found in appendix A.1.

		C [g/L]	ρ [g/cm^3]	E [kPa]
Phantom I	1st layer	8.1(2)	1.003(5)	17.4(9)
	2nd layer	6.5(2)	1.002(5)	11.6(6)
Phantom II	1st layer	6.5(2)	0.996(5)	11.6(6)
	2nd layer	6.5(2)	1.197(10)	11.6(6)

Table 2.1: *Properties of the fabricated phantoms.*
Listed are the agar concentrations C, the measured densities ρ and the Young's moduli E estimated with (2.4). The stated errors are propagated from the assumed measurement errors and in case of ρ the standard deviation of the weighted average of the individual samples (see A.1 for details).

In the MRR measurements of these phantoms, three time series were recorded for each phantom. Two measurement series were acquired with a sample interval of $\Delta\tau = 2$ ms, one from 0 ms to 100 ms and one from 1 ms to 99 ms. For these measurements N_τ was set to 10. The third time series was measured with $\Delta\tau = 1$ ms from $\tau = 0.5$ ms to 99.5 ms and $N_\tau = 5$. Combined, these measurements provided a time series covering τ values from 0 ms to 100 ms with a sample interval of $\Delta\tau = 0.5$ ms. In total 1510 images were acquired in a scan time of 77 min for each phantom.

2.2.2 In vivo Measurements

The measurements on human subjects presented in this thesis were taken on one healthy volunteer and on four patients with diagnosed meningioma prior to surgery (cf. section 1.2.3.1. The healthy volunteer was a 30 years old male, the meningioma patients were two male aged 71 and 67 years (Patients **B** and **C**) and two female ones aged 43 and 55 years (Patients **A** and **D**). All these measurements were approved by the ethics committee of the medical faculty of the University of Bonn[14].

For the experiment the head of the subject was placed on the lifting device and fixated using a vacuum cushion to minimize head motion. Dependent on the size of the subject's head, either a standard vacuum cushion as part of the MRI scanner's equipment or a custom made one[15] were chosen. A series of high resolution structural images of transversal planes were obtained, as well as the alignment scans images to align the lifting device with the scanner's coordinate system (see section 2.1.3).

Subject	$\Delta\tau$[ms]	τ[ms]	N_τ	N_{total}	t_{total} [min]
Healthy volunteer	1.0	0.0 - 100.0	5	505	30
	1.0	0.5 - 99.5	5	500	30
	10.0	110.0 - 400.0	5	150	9
	10.0	105.0 - 395.0	5	150	9
Patient **A**	1.5	0.0 - 69.0	10	470	28
	10.0	75.0 - 175.0	10	110	7
	10.0	80.0 - 180.0	10	110	7
Patient **B**	1.5	0.0 - 69.0	10	470	28
Patients **C** and **D**	1.0	0.0 - 80.0	5	405	24
	10.0	100.0 - 290.0	5	100	7
	10.0	95.0 - 285.0	5	100	7

Table 2.2: *Summary of measurements on human subjects.*
Listed are the sampling interval $\Delta\tau$, the range of the measured values of τ, the amount of averages N_τ per value of τ, the total number of images N_{total} acquired in this measurement sequence and the total scan time t_{total}. All images acquired for one subject were combined into one single timeline during the post-processing.

A transversal slice (in the case of the meningioma patients one that contained the meningioma) was selected that was measured using the motion sensitive sequence described in section 2.1.2. A time series with varied τ was recorded with the following parameters: The motion sensitive gradients were chosen as $\delta = 5\,\text{ms}$, $\Delta = 45\,\text{ms}$ and $G = 34.82\,\text{mT/m}$. τ was varied from 0 ms to 400 ms for the healthy volunteer, 0 ms to 180 ms for the patients A and B, and from 0 ms to 290 ms for the patients C and D. Each time series was sampled with varying steps of $\Delta\tau$ and for every τ five to ten measurements were taken. Due to the limitation of maximum 510 images per measuring protocol (cf. section 2.1.2.1), these times series were sampled using up to four individual time series and combining them. The details are summarized in table 2.2. All measurements were performed with an echo time $T_{\text{E}} = 80\,\text{ms}$ and a repetition time $T_{\text{R}} = 3500\,\text{ms}$. The voxel sizes were $2 \times 2 \times 5\,\text{mm}^3$. Partial Fourier was set to 6/8. For each subject, additional ten

---

[14] Healthy volunteers: No. 139/12, Meningioma patients: No. 019/15

[15] Made by Sylvia Napiletzki during her master's thesis

measurements were taken without induced motion of the head prior to the measurement with motion.

3 Data Analysis

During the course of this thesis, several methods were developed to analyze the data obtained with the experimental setup as described in the last chapter. These methods are introduced and described in this chapter. This includes the data of the OPMs and the post-procession of the measured phase data. The chapter finishes with the description of approaches to infer the physical trajectory of volume elements from the measured phase progression.

All analysis methods presented in this chapter, including the phase unwrapping algorithms, have been implemented in python [105] using the Numpy [106] and Scipy [107] packages and have been bundled into the package PyMRR [108].

All data analysis for this thesis was done using the IPython notebook [109] and python scripts based on the PyMRR package.

3.1 Reconstruction of the Induced Falling Motion

The prototype of the lifting device is equipped with three OPMs to monitor the motion of the movable shell (cf. section 2.1.1.2). This section describes, how the voltage signal of the OPM was processed to determine the motion of the shell in physical units.

3.1.1 Smoothing and Calibration

Every time an individual measurement with one specific τ was performed, the data of the three OPMs as well as the data of the RF-antenna (see section 2.1.1.2) was stored automatically using the oscilloscope's test mode[1]. Later, the saved waveforms were matched to the acquired phase data by comparing the time stamp of the waveform files with the acquisition time of the phase data stored in the DICOM files.

For further analysis the data was smoothed to remove the high frequency noise present by convolving the sampled time series with a Hann window function [110]. The value of this function at a sample n is defined as

$$w(n) = \frac{1}{2}\left(1 - \cos\left(\frac{2\pi n}{N-1}\right)\right), \qquad 0 \leq n \leq N-1. \tag{3.1}$$

The length N of the window was usually chosen as an odd number of samples corresponding to a width of 3 ms ($N = 749$ with a sampling interval $\Delta t = 4\,\mu\text{s}$). This seemed to

---

[1] Storing was done in the oscilloscope's binary format .ics to ensure the storing process finished before the start of the next signal.

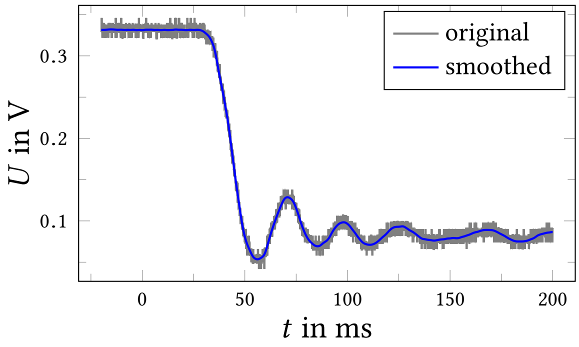

Figure 3.1: *Example of a smoothed optical signal.*
The voltage of the photo diode was sampled with $\Delta t = 4\,\mu\text{s}$ and smoothed with a Hann window with a window length of $N = 749$ samples, which equals roughly 3 ms.

be a reasonable compromise between sufficient smoothing and reduced dynamics of the signal. Figure 3.1 shows an example of a measured signal and the smoothed equivalent.

If the OPMs were gauged prior to a measurement, the smoothed voltages were converted to positions in a last step. For this calibration, a linear function was fitted to the gauge data by orthogonal distance regression [111, present in 107] to be able to account for measurement errors both in the voltage U as well as the calipered distances $\tilde{y}_\text{s}$ (cf. section 2.1.1.2). The standard deviation $\sigma(\tilde{y}_\text{s})$ of the position was then calculated in the normal way using the covariance matrix $\boldsymbol{V}_U$ of the fit results [112, 60]:

$$\sigma(\tilde{y}_\text{s})^2 = \boldsymbol{g}^\top \boldsymbol{V}_U \boldsymbol{g}, \qquad \boldsymbol{g} = \begin{pmatrix} \tilde{y}_\text{s} \\ 1 \end{pmatrix}. \tag{3.2}$$

An example of such a calibration is shown in fig. 3.2.

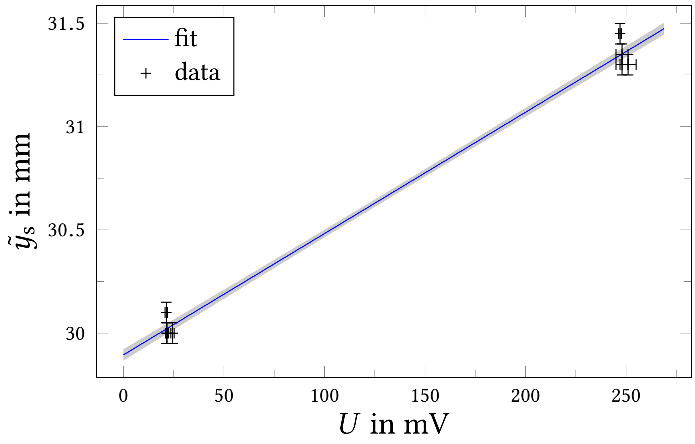

Figure 3.2: *Exemplary calibration curve.*
The OPM at the patient right side of the healthy volunteer (cf. section 4.4) has been calibrated by calipering the height $\tilde{y}_\text{s}$ of the movable shell with respect to a fixed point at the base in the upper and lower position and simultaneously measuring the voltage U of the photo diode. A linear function has been fitted to this data that was later on used as a calibration curve for this OPM. The errorband indicates the standard deviation of the position based on the error matrix of the fit parameters.

3.1.2 Matching Coordinate Systems

To locate the lifting device and the OPMs in the DPCS, the location of the three vitamin E markers fixed to the shell was analyzed in alignment scans obtained prior to an MRR measurement. Those scans were sets of coronal slices (cf. section 2.1.3).

To ensure reproducibility over all measured slices for one measurement as well as over different measurements, and to ease the work flow needed to analyze such a measurement, a (semi)automatical way was chosen to find the signature of the vitamin E markers in those images.

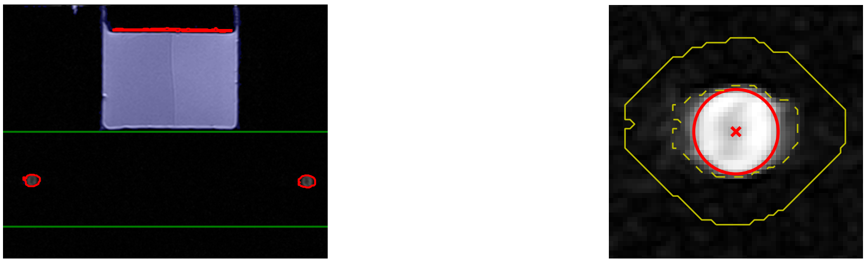

(a) *Alignment scan partitioned into regions*

(b) *Fit of an ellipse to a marker region*

Figure 3.3: *Partitioning of alignment scans and marker fitting.*
(a) shows the partitioning of a single slice of an alignment. The slice used is the same as the one shown in fig. 2.7. Regions that were classified as potential markers by the number of pixels in that region are outlined in red. All other regions found are indicated in blue. Green lines indicate the spatial limits for regions to be classified as markers. Only the two small regions anterior left and right were classified as markers, as was intended. (b) shows the fit of an ellipse to the region of the marker on the patient's right side. The original region is outlined in dashed yellow, the grown region $\mathcal{R}$ *used for fitting is outlined in solid yellow, and the resulting ellipse and its center are marked in red. In this case, the ellipse is almost circular.*

First the image was partitioned in different regions. For this, a binary image of the original one was created by setting all pixels above a certain threshold p_{thresh} to one and all other pixels to zero. Throughout this thesis, a threshold of $p_{\text{thresh}} = 35$ was used. The binary image was used to find clusters of connected pixels set to one using the DBSCAN algorithm [113, implemented in 114, 115]. The algorithm was tuned such that each region consists of connected valid pixels completely surrounded by other valid pixels, and their neighboring valid pixels.

To find the regions corresponding to the markers in the binary image, the amount N of pixels in each region was considered. All regions with $N < 200$ and $N > 1000$ were rejected. In a second step, constrains on the location of the remaining regions were applied. Only regions were considered whose pixels (r_i, c_i) were all located in the specified limits. For the dorsal alignment scan, only regions with $r \in [200, 350]$ were considered. For the cranial scan, pixels were constrained to $r \in [50, 200]$ and $c \in [150, 300]$. Using these selection criteria, the markers in almost all analyzed images were identified correctly: In two of nine cases, the location of the dorsal scans were shifted so that the row constraint had to be adapted, and in one case the binary threshold for the dorsal scan had to be raised to 60 due to ghost artifacts. In only one case more regions than markers were found in the dorsal scan so that a manual selection had to be performed. An example of the partition of the images is shown in fig. 3.3a.

The marker regions were transfered to the original alignment scans and each marker region was used to fit an ellipse to the region to find the marker's center. The ellipse was chosen due to the ellipsoidal form of the vitamin E markers: every slice through such a marker is either a circle or an ellipse. For fitting, the region was first grown by ten pixels in each direction to minimize the influence of the binary threshold used for finding the regions. The image data was normalized to the maximum value present in that grown region $\mathcal{R}$, so that all values p_i of the pixels in that region were in the interval $p_i \in [0, 1]$. All pixels outside of $\mathcal{R}$ were set to zero.

The ellipse to be fitted was assumed to have the major axis aligned to the coordinate axis of the image. Pixels (r_i, c_i) inside its area fulfill the equation

$$\left(\frac{c_i - m_c}{a_1}\right)^2 + \left(\frac{r_i - m_r}{a_2}\right)^2 \leq 1 \tag{3.3}$$

with the two semi-axes a_1 and a_2 and the center point (m_r, m_c). To fit the ellipse, the following minimization was performed:

$$\underset{a_1,a_2,m_c,m_r \in \mathbb{R}}{\arg\min} \sum_{i \in \mathcal{R}} (p_i - b_i)^2, \qquad b_i = b(r_i, c_i) = \begin{cases} 1 & \left(\frac{c_i - m_c}{a_1}\right)^2 + \left(\frac{r_i - m_r}{a_2}\right)^2 \leq 1, \\ 0 & \text{else.} \end{cases} \tag{3.4}$$

The b_i describe a binary image with all pixels inside the ellipse equal to one and all pixels outside equal to zero. Therefore, pixels with low intensity will contribute less likely to the fit than pixels with high intensity. An exemplary result of the fitting process is shown in fig. 3.3b.

The so found pixel coordinates (m_r, m_c) of the ellipse's center in slice s of an alignment scan were converted to the DPCS using eq. (1.23). The different centers found in different slices were then averaged to get an estimate on the marker's center in the coronal plane of the DPCS. Since we were only interested in the motion of the shell relative to its starting position, the position of the markers in the y-direction of the DPCS has been neglected.

The locations of the marker on the shell relative to the locations of the OPMs were measured by means of a photograph of the shell taken from directly above. Chessboard scales were positioned on the shell to be able to determine distances in this photograph. The optical distortion of the objective lens used has been corrected using the manufacturers software. The known locations of the markers were each used to calculate the location of a fixed reference point in the DPCS. As the reference point, the center of the photograph used to measure the distances was chosen. This point was roughly centered on the shell. The weighted average of the coordinate of this reference point was then used to calculate the locations of the OPMs in the DPCS. The measures of the lengths of the connection lines from the markers to the reference point and from the reference point to the OPMs can be found in table 3.1.

conjunction		x in mm	z in mm
left marker	→ Ref	−81.2(11)	47.5(7)
right marker	→ Ref	85.6(14)	42.9(7)
cranial marker	→ Ref	−8.1(1)	−101.6(6)
Ref → left OPM		−127.1(19)	89.3(14)
Ref → right OPM		139.4(21)	78.1(12)
Ref → cranial OPM		−6.4(1)	−129.4(8)

Table 3.1: *Horizontal distances on the shell.*
Listed are the horizontal measures of the lengths of the connection lines from the markers to the reference point (Ref) and from the reference point to the OPMs. left *and* right *are named after the position in the DPCS, i. e. according to the patient's orientation. These measures and their listed standard deviation were used to calculate the location of the OPMs in the DPCS.*

3.1.3 Shell Motion

To closely investigate the falling motion during the MRR experiment, the data of the three OPMs were used to reconstruct both location and orientation of the movable shell over time. To do so, a horizontal plane through the shell was assumed, represented by the Hesse normal form

$$\boldsymbol{r} \cdot \boldsymbol{n} - d = 0, \tag{3.5}$$

where $\boldsymbol{n}$ is the unit normal vector of the plane, d the distance of the plane to the origin of the coordinate system and $\boldsymbol{r}$ is the position vector of an arbitrary point on the plane. The locations of the OPMs in the xz-plane of the DPCS (cf. last section) and the calibrated optical data (cf. section 3.1.1) were used to create three position vectors $\boldsymbol{p}_1(t)$, $\boldsymbol{p}_2(t)$ and $\boldsymbol{p}_3(t)$. The y component of these vectors was normalized such that $y = 0$ in the upper position of the shell. The $\boldsymbol{p}_i$, therefore, described the relative height of the shell at the locations of the OPMs over time. The three position vectors were then used to construct the plane:

$$\boldsymbol{n} = \frac{(\boldsymbol{p}_1 - \boldsymbol{p}_3) \times (\boldsymbol{p}_2 - \boldsymbol{p}_3)}{\left|(\boldsymbol{p}_1 - \boldsymbol{p}_3) \times (\boldsymbol{p}_2 - \boldsymbol{p}_3)\right|} \tag{3.6}$$

and

$$d = \boldsymbol{n} \cdot \boldsymbol{p}_3. \tag{3.7}$$

$\boldsymbol{n}$ and d have been computed for different points in time over the course of the falling motion. The systematic uncertainties of the position vectors $\boldsymbol{p}_i$, including those of the location of the OPMs in the DPCS and of the calibration of the individual OPM have been propagated to both $\boldsymbol{n}$ and d.

Using $\boldsymbol{n}(t)$ and $d(t)$, the height of the movable shell $y_\mathrm{s}(\tau, t, x, z)$ in the DPCS could be computed by solving eq. (3.5) for $y_\mathrm{s} = r_2$. In particular, this allowed the calculation of the falling motion at the location of the measured transversal slice by choosing z accordingly.

Additionally, the orientation of the shell during the falling motion was analyzed by computing the azimuth and the inclination of $\boldsymbol{n}$.

3.2 Phase Processing

This section describes how the phase data acquired with MRR was processed to obtain the final multi-dimensional phase data.

3.2.1 Phase Unwrapping

As described in section 1.5, the phase in the acquired images is initially wrapped to the interval $[0, 2\pi)$. To obtain a continuous image of the true phase, the data had to be unwrapped. For this, all three algorithms described in section 1.5.2 have been implemented in python and tested with the data acquired in MRR. In this section, typical results and artifacts are presented by means of phase images of a homogeneous agar hydrogel phantom.

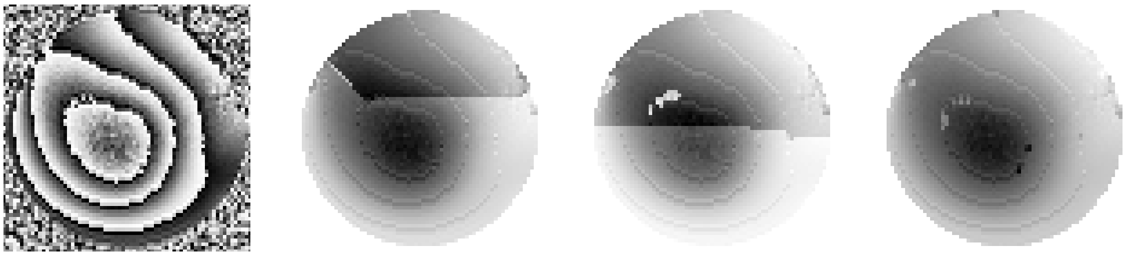

(a) *initial* ***(b)*** *Goldstein* ***(c)*** *mask cut* ***(d)*** *quality guided*

Figure 3.4: *Phase unwrapping using different algorithms.*
The performance of three different unwrapping algorithms is presented by means of a single phase image of a MRR measurement of a homogeneous agar hydrogel phantom. Fig. (a) shows the unprocessed phase image. In the circular region of the phantom cross section the phase increases from the center to the border. Three concentrical lines of discontinuity are visible. Especially in the center of the phantom, significant measurement noise is visible as well. In the region outside of the phantom area the phase shows random noise. (b) to (d) show the results of Goldstein's algorithm, the mask cut algorithm and the quality guided algorithm. Both Goldstein's algorithm and the mask cut algorithm partition the phantom area into discontinuously connected regions. Only the quality guided algorithm creates a continuous phase over most of the phantom's area. The contours of the original phase discontinuities remain visible in all three unwrapped images.

Figure 3.4 shows the first unprocessed phase image of ten identical measurements and the result of all three phase unwrapping algorithms. In the unprocessed image (fig. 3.4a), several concentric phase discontinuities are visible as black-white transitions. The quality of the measured phase appears to be low in some areas where a lot of noise is present, most prominently in the center and at the right border of the phantom. The area outside of the phantom is filled with random noise, since in this region no MRI signal is present during the measurement. Prior to the unwrapping these areas are masked so that the unwrapping is restricted to the region of interest (ROI). The result of the phase unwrapping of this image using Goldstein's algorithm (cf. section 1.5.2.1) is partitioned into two large areas and few small ones. Every area individually shows a continuous phase. The difference in phase values on either side of the border of these areas is $\pm 2\pi$. The creation of these areas can be explained by the branch cuts created by the algorithm. These are positioned in such a way that they balance the residues that are created by noise in the image. In this case, the branch cuts created separated regions that are unwrapped individually. In the mask cut algorithm (cf. section 1.5.2.2) the placement of these cuts is supposed to be optimized by the use of a quality map. However, in this case the algorithm does not provide a better result: Although the cuts were placed at different locations, the result is still partitioned in several regions. The quality guided algorithm (cf. section 1.5.2.3) does not use cuts. Consequently, the result of this algorithm is not partitioned and shows a continuous phase over a large percentage of the phantom area. However, there are still small regions near the original discontinuities present. Additionally, in all three unwrapped images, the original phase discontinuities are still visible as thin lines.

The results presented here are typical results for all measurements performed during in this theses, albeit the line artifacts did not occur in every measurement and if so they did not in every image. Generally speaking, the quality guided algorithm was supposed to be the least robust one of the three tested algorithms (cf. section 1.5.2). Nevertheless, for the phase images acquired in MRR it significantly outperformed the other two algorithms in terms of amount and severity of the produced artifacts. Therefore, the quality guided algorithm eventually became the common choice while post processing MRR data. This came with the cost of increased run time: In the current implementation, the unwrapping of the 3295 pixels in the unmasked region of the phantom took 336 ms with Goldstein's algorithm, but 743 ms with the quality guided algorithm on a common desktop machine. The implementation of the algorithms was not run-time optimized, though, and can likely be improved greatly.

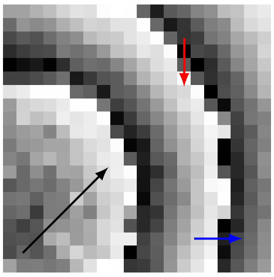

Figure 3.5: *Magnified region of the unprocessed phase image: The phase increases from the inside (lower left corner) to the outside (upper right corner) of the phantom, marked with the black arrow. The discontinuities in the phase are sharp along the rows (blue arrow), but smoothed along the column direction (red arrow). The intermediate phase values of this smooth transition cause the contour lines in the unwrapped images (cf. fig. 3.4).*

The origin of the thin lines appearing along the location of the original phase wraps can be seen in fig. 3.5. It shows a magnified portion of the unprocessed phase image in fig. 3.4a. In the direction of the lower left corner to the upper right corner of the image, the phase value increases until it reaches a value of 2π (white), is then wrapped to a value near 0 (black) and continues to increase. However, closer inspection of the line of the phase wrap shows, that the wrapping is only discontinuous along the rows of the image. In column direction, black and white pixels are always separated by a gray pixel. This intermediate value smooths the phase wrap and destroys the underlying discontinuity. After the phase unwrapping, these pixels with intermediate values remain and create the line artifacts.

The origin of this smoothing of the phase wrap is currently unknown. The direction of the smoothing is aligned with the direction of the falling motion in the measurement and with the direction of the phase encoding gradients of the spatial encoding of the sequence. Therefore, the phenomenon might be a motion artifact: As explained in sections 1.3.3.3 and 2.1.2, the y-direction of the image is encoded by altering the phase of the isochromats in y-direction prior to the read-out. If there is still macroscopic motion present during this process, this phase encoding might be altered and the signals of adjacent voxels might be mixed [3, sqq.571]. However, the effect should then be greatest with small values of τ, and smaller with large values, which is not what was observed. The effect might also be originated in the image reconstruction algorithm used to create the phase images from the measured MRI signal, that might use some kind of filtering or smoothing in the phase encoding direction. This algorithm has been provided by the manufacturer of the used MRI scanner and has not been altered during this thesis, so this assumption was not tested. However, in this case the effect should have been present in *all* acquired images, which was not observed, either.

Typically, measurements in MRR with specific values of τ were repeated 5 to 10 times and the average image was calculated to reduce the measurement noise. However, the images have to be unwrapped prior to averaging them due to the phase wraps that are present in the individual images. Unwrapping artifacts, especially whole regions with phase offsets of multiples of 2π, can have a large impact on the averaged images. However, even small artifacts like the ones present in fig. 3.4d can significantly reduce the quality of the averaged phase image in the respective area.

Therefore, it was beneficial to average the wrapped phase images and improve the signal-to-noise ratio (SNR) of the phase prior to the unwrapping. This has been done by representing the phase ϕ of each voxel as a phasor on the unit circle:

$$\begin{pmatrix} x \\ y \end{pmatrix} = \begin{pmatrix} \cos(\phi) \\ \sin(\phi) \end{pmatrix}. \tag{3.8}$$

The mean phasor of N phase values could then be calculated by taking the mean value of the x and y coordinates individually:

$$\begin{pmatrix} \overline{x} \\ \overline{y} \end{pmatrix} = \frac{1}{N} \sum_i \begin{pmatrix} x_i \\ y_i \end{pmatrix}. \tag{3.9}$$

Finally, the mean phase of a voxel was calculated as the angle of the mean phasor by using $\overline{\phi} = \operatorname{arctan2}(\overline{y}, \overline{x})$ with the two argument variant of the arctan function:

$$\operatorname{arctan2}(y,x) = \begin{cases} \arctan\left(\frac{y}{x}\right) & x > 0, \\ \arctan\left(\frac{y}{x}\right) + \pi & x < 0 \wedge y \geq 0, \\ \arctan\left(\frac{y}{x}\right) - \pi & x < 0 \wedge y < 0, \\ +\frac{\pi}{2} & x = 0 \wedge y > 0, \\ -\frac{\pi}{2} & x = 0 \wedge y < 0. \end{cases} \tag{3.10}$$

This function was used because it produces the whole range of angles $(-\pi, \pi]$. For consistency reasons, $\overline{\phi}$ was finally mapped back into the range $[0, 2\pi)$.

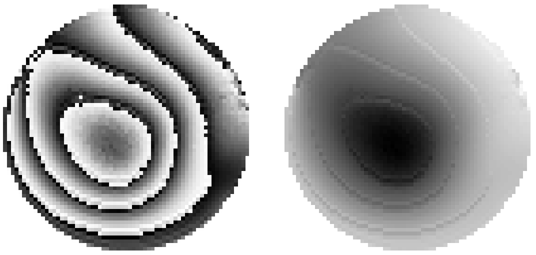

(a) *Mean wrapped phase* ***(b)*** *Unwrapped average*

Figure 3.6: *Unwrapped average phase image. Prior to unwrapping, an averaged wrapped phase image (b) was calculated from all ten identical measurements of the homogeneous phantom. Due to the averaging, the measurement noise in the image was significantly reduced (cf. fig. 3.4a). The average phase image was unwrapped using the quality guided algorithm. The result (b) is free of unwrapping artifacts. The contour lines of the original phase discontinuities are still present, though, since they appeared at the same location in every individual image.*

Figure 3.6a shows the averaged wrapped phase image of all ten measurements of the homogeneous phantom. The image shows significantly less noise than the single phase image in fig. 3.4a. The average phase was unwrapped using the quality guided algorithm (cf. fig. 3.6b). The small artifacts that were present in the corresponding single phase image (cf. fig. 3.4d) are not visible here. The contours of the original phase discontinuities are still visible, though. The fact that those lines do not vanish in the averaged image is an indication of the reproducibility of the measurement: major changes in the falling motion or image acquisition between measurements would misalign the phase wraps.

3.2.2 Combining Individual Measurements

As has been described in section 2.1.2.1, the data of an MRR measurement is present in series of DICOM files, each representing one image of a measurement of one slice at one specific τ value. To combine these individual measurements, the data was first sorted by τ. Then all images for a distinct value of τ were averaged using the mean phasor approach described in the last section and subsequently unwrapped. This ensured as little unwrapping artifacts as possible were introduced into the data. The data was then combined into a single three-dimensional array representing the temporal and spatial evolution of the phase $\phi(r, c, \tau)$ of the isochromats in the measured slice. Since the images of different values of τ were unwrapped individually, the phase progression in the temporal direction was not continuous at this point. The phase was, therefore, unwrapped along the τ-axis. The algorithms described in section 1.5.2 could not be used for this since they only operate on two-dimensional data. Instead, the difference between successive images was calculated pixel wise and the average difference examined. Similar to the basic phase unwrapping concepts described in section 1.5.1, multiples of 2π were added to all pixels of one image if this difference exceeded the range of $[-\pi, +\pi]$. An example of this temporal unwrapping is shown in fig. 3.7.

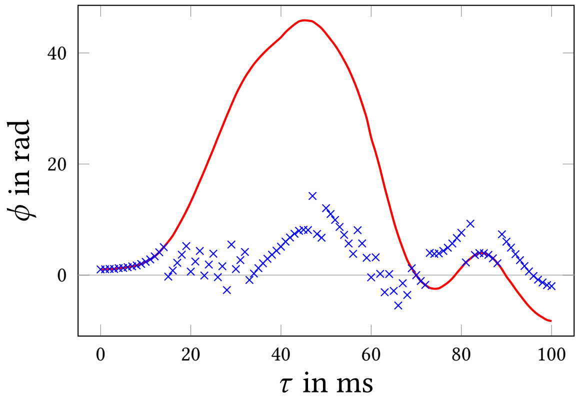

Figure 3.7: *Phase unwrapping in the temporal domain.*
The phase of a single voxel of a homogeneous agar hydrogel phantom is plotted as a function of τ. Blue marks show the phase values prior to the temporal unwrapping of the phase, the red line shows the continuous phase progression after the temporal unwrapping.

The measured phase contains, besides the encoded motion, all phase altering effects like magnetic field inhomogeneities or local susceptibility distinctions. To remove all non-motion effects, every series of measurements is accompanied by a baseline measurement with the same sequence parameters but without induced motion. This baseline image is unwrapped and averaged and subtracted from the phase progression pixel wise. This way, the phase of those corrected phase images should only encode motion, provided the other influences on the phase do not change during the measurement.

In the results section of the thesis, the post processed phase is presented with a standard error. This has been computed by error propagating the standard error of the average of the baseline along with the standard error of the average of the phase images pixel wise.

3.2.3 Relative Phase

After combining the individual measurements to a continuous data set (cf. the last section), the phase ϕ encodes the total displacement of every measured volume element relative to the original location of the element prior to the falling motion. For an examination of the response of the brain tissue to the excitation by the falling motion only the displacement *relative* to the original position of the volume element in the brain is relevant. If we assume the cranial bone is not deformed during an MRR measurement, this is equivalent to the displacement relative to the cranial bone. It would, therefore, be beneficial to remove the phase signal of the falling motion from the measured phase.

This has been done by calculating the relative phase $\Delta\phi_r$ with respect to the phase of a reference pixel inside the brain volume. This reference pixel was chosen as one of the pixel in the central part of the falx cerebri, since this part of the brain is assumed to show little displacement relative to the cranial bone (cf. section 1.2.1.

In principle, this relative phase could be computed from the total phase ϕ directly. However, to account for possible constant phase shifts between different phase images obtained with the same value of τ, the reference phase has been computed for every single phase image prior to any other post processing except masking areas outside of the ROI. Computing this differences in the measured wrapped phase ψ yields (cf. eq. (1.24))

$$\begin{aligned}\Delta\psi &= \psi_1 - \psi_2 \\ &= \phi_1 + 2\pi \cdot n_1 - (\phi_2 + 2\pi \cdot n_2) \\ &= \Delta\phi + 2\pi\Delta n.\end{aligned} \tag{3.11}$$

This means the differences in the wrapped and unwrapped phase images only differ by multiples of 2π, which will vanish by unwrapping the data. The computed wrapped phase difference images have been averaged and unwrapped in the same way as described in the last section. To perform the baseline correction, the same differences relative to the reference pixel have been computed in the baseline images as well, averaged pixel wise and subtracted from the relative phase images. Finally, the so obtained baseline corrected relative phase was unwrapped in the temporal domain and normalized so that $\Delta\phi_r(0) = 0$.

The standard error of the relative phase has been computed by computing the standard error of the average of the relative phase images and propagating the standard error of the average differences in the baseline images.

3.2.4 Strain Assessment

As described in section 2.1, the phase acquired in MRR measures deflection of the material after an excitation with respect to the original location of the volume element prior to the falling motion. The signal of the falling motion can to some extend be eliminated (cf. the last section). However, even this signal still measures *deflection*, albeit with respect to the cranial bone and with that to the original configuration of the material. This deflection will however depend highly on the geometry and the boundary conditions of the test subject: A homogeneous agar phantom for instance should show a high deflection in the center of the volume and a low deflection near the phantom container. To minimize this effect of the global boundary conditions, the measure phase strain ϵ_ϕ was introduced, which is the gradient of the phase in y-direction:

$$\epsilon_\phi(\tau) = \frac{\partial}{\partial y}\phi(\tau). \tag{3.12}$$

The calculation was done by using central differences on the phase images. Prior to the calculation the phase data was spatially smoothed using a gaussian kernel to avoid the enhancement of noise. For the results presented in this thesis the width of this kernel was $\sigma = 0.7$ if not noted otherwise.

Using eq. (2.2) one obtains

$$\epsilon_\phi(\tau) = \frac{\partial}{\partial y}\gamma \int_{t_1}^{t_2} \boldsymbol{G}(t) \cdot \boldsymbol{r}(t+\tau)\,\mathrm{d}t \tag{3.13}$$

and, since $\frac{\partial}{\partial y}G = 0$ (cf. section 1.3.1.2),

$$\epsilon_\phi(\tau) = \gamma \int_{t1}^{t_2} \boldsymbol{G}(t) \cdot \frac{\partial}{\partial y}\boldsymbol{r}(t+\tau)\,\mathrm{d}t. \tag{3.14}$$

In MRR, the trajectory $\boldsymbol{r}$ is the sum of the trajectory of the falling motion $\boldsymbol{r}_{\text{macro}}$ and the relative displacement $\boldsymbol{u}$ of a volume element. If we assume the cranial bone does not deform during an MRR experiment, we obtain $\frac{\partial}{\partial y}\boldsymbol{r}_{\text{macro}} = 0$. If we further assume MRR only encodes motion in the direction of the MEGs, we get $\boldsymbol{u} = u \cdot \hat{\boldsymbol{e}}_G$. Throughout this thesis, the MEGs were always aligned with the falling motion, so that we get $\boldsymbol{u} = u_y$. We can then write (cf. eq. (1.8))

$$\frac{\partial}{\partial y}\boldsymbol{r} = \frac{\partial}{\partial y}u_y = \epsilon_{yy}, \tag{3.15}$$

i.e. the derivative of the trajectory is the principal strain in the direction of the falling motion. With that, eq. (3.14) becomes

$$\epsilon_\phi(\tau) = \gamma \int_{t_1}^{t_2} G(t) \cdot \epsilon_{yy}(t+\tau)\,\mathrm{d}t. \tag{3.16}$$

Note the similarity of this equation with eq. (2.2). The phase strain defined in eq. (3.12) is, therefore, the convolution of the strain and the gradients of the MRI sequence (again except for the sign of t in ϵ_{yy}, cf. eq. (2.3)):

$$\begin{aligned} \epsilon_\phi &= \epsilon_{yy} * G, \\ \mathcal{F}(\epsilon_\phi) &= \mathcal{F}(\epsilon_{yy}) \cdot \mathcal{F}(G). \end{aligned} \tag{3.17}$$

The phase strain ϵ_ϕ is therefore a measure for the local principal strain ϵ_{yy} in the same way as the measured total phase ϕ is a measure for the local total deflection and should be directly dependent on the local acting forces and the local mechanical properties of the material.

If the volume elements in the brain tissue oscillate after the excitation, the strain will oscillate as well and different parts of the brain volume will likely experience higher or lower strain at different values of τ. For further analysis, the integrated absolute value of the phase strain

$$\epsilon_{\phi,\,\text{total}} = \int\limits_{\tau_{\min}}^{\tau_{\max}} |\epsilon_\phi| \,\mathrm{d}\tau \tag{3.18}$$

has been computed. While the integral over the phase strain should equal zero in the exact case, this is obviously not the case for $\epsilon_{\phi,\,\text{total}}$. However, this measure should yield higher values for higher magnitudes of the strain. In general, higher strain values indicate softer material, provided the acting forces are homogeneous (cf. section 1.1). Throughout this thesis, $\epsilon_{\phi,\,\text{total}}$ has been computed from the sampled data using the composite trapezoidal rule.

3.3 Deconvolution of the Phase Signal

The phase measured in one MRR decodes the occurring displacements $\boldsymbol{r}(t)$ convoluted with the MRI sequence's combined gradient form $\boldsymbol{G}(t)$ (cf. section 2.1.2.2). Similarly, the phase strain introduced in section 3.2.4 is a convolution of the mechanical strain and $\boldsymbol{G}$. It might be beneficial to extract the physical displacement respectively the physical strain from this phase data to be able to quantify the measured results. This is done by deconvolution of eq. (2.2) or eq. (3.16) respectively. Means to perform this deconvolution are discussed in this section. Since both equations are similar, we will only consider displacements in the following derivations. The presented results hold true for the deconvolution of the phase strain, too, though.

In principle, $\boldsymbol{G}(t)$ encodes motion in arbitrary directions. In the following, we assume one-dimensional displacement, so that gradients perpendicular to the direction of that motion do not alter the measured phase ϕ and $\boldsymbol{G}(t)$ becomes $G(t) \cdot \hat{\boldsymbol{e}}_r$. We therefore write $\boldsymbol{G}$ and $\boldsymbol{r}$ as scalars.

In the presence of measurement noise eq. (2.3) becomes

$$\phi(\tau) = (r * G)(\tau) + n(\tau) \tag{3.19}$$

or

$$\mathcal{F}(\phi) = \mathcal{F}(r) \cdot \mathcal{F}(G) + \mathcal{F}(n) \tag{3.20}$$

with some noise term n.

The naive approach of reconstructing r, solving eq. (3.20) for $\mathcal{F}(r)$,

$$\mathcal{F}(r) = \frac{\mathcal{F}(\phi)}{\mathcal{F}(G)} - \frac{\mathcal{F}(n)}{\mathcal{F}(G)}, \tag{3.21}$$

fails due to the form of $\mathcal{F}(G)$ which includes various zero points (cf. fig. 2.6). Additionally, high-frequency parts of n will be increased disproportionately since $\mathcal{F}(G)$ decreases with higher frequencies.

Hence, three different approaches to solve eq. (2.2) have been developed and tested during the course of this thesis, which will be described in the following parts. For all those approaches, we assume $\boldsymbol{r}(t) = 0 \ \forall \ t \leq t_s$, with t_s being the start of the falling motion and $G(t) \neq 0$ only for $t \in [t_1, t_2]$[2]. We further assume the phase has no constant offset. From this definitions follows $\phi(\tau = 0) = 0$. In practice, as described in section 2.1.2.1, the phase is only measured at N discrete values of τ, which we write as $\tau_0, \dots, \tau_N$.

3.3.1 Direct Approach

The most basic approach was to iteratively use eq. (2.2) to calculate samples r_i of the trajectory. If we assume $r(\tau)$ is known up to τ_{n-1}, $\phi(\tau_n)$ can be written as

$$\phi(\tau_n) = \gamma \int\limits_{t_1}^{t_2-\Delta\tau} G(t) \cdot r(t+\tau_n)\,\mathrm{d}t + \gamma \int\limits_{t_2-\Delta\tau}^{t_2} G(t) \cdot r(t+\tau_n)\,\mathrm{d}t, \tag{3.22}$$

with $\Delta\tau = \tau_n - \tau_{n-1}$. In the first term, which we denote as ϕ_{prior}, $r(t+\tau_n)$ is known, so that the integral can be computed. The second integral can be approximated by

$$\gamma \int\limits_{t_2-\Delta\tau}^{t_2} G(t) \cdot r(t+\tau_n)\,\mathrm{d}t \approx \frac{\gamma\Delta\tau}{2}\Big(G(t_2) r(t_2+\tau_n) + G(t_2-\Delta\tau) r(t_2+\tau_{n-1})\Big). \tag{3.23}$$

As long as $\Delta\tau < \delta$ holds true, $G(t)$ is approximately constant. Setting additionally $t_2 = 0$ leads to the following iteration formula for r:

$$r(\tau_n) = \frac{2\Big(\phi(\tau_n) - \phi_{\text{prior}}(\tau)\Big)}{\gamma G \Delta\tau} - r(\tau_{n-1}). \tag{3.24}$$

The approximation in eq. (3.23) becomes better, the smaller $\Delta\tau$ becomes. At the same time, the smaller $\Delta\tau$ becomes, the lesser the assumption of a constant gradient G in eq. (3.24) is justified due to the non-constant ramp of length ζ at the end of the gradient (cf. fig. 2.5). Therefore, the accuracy of this approach is clearly limited.

---

[2] Due to the definition of τ, $t_s = t_2$ if $\tau = 0$. See section 2.1.2.1.

3.3.2 Derivative Based Approach

Alternatively, one can take the derivative of eq. (3.22) with respect to τ. Using Leibniz's rule, this yields

$$\begin{aligned}\frac{\mathrm{d}}{\mathrm{d}\tau}\phi(\tau_n) = \frac{\mathrm{d}}{\mathrm{d}\tau}\phi_{\text{prior}}(\tau_n) &+ \gamma G\Big(r(t_2+\tau) - r(t_2+\tau_{n-1})\Big) \\ &+ \gamma G \int\limits_{t_2-\Delta\tau}^{t_2} \frac{\partial}{\partial\tau} r(t+\tau_n)\,\mathrm{d}t\end{aligned} \tag{3.25}$$

while again approximating $G(t) \approx G$ for $t \in [t_2 - \Delta\tau, t_2]$. Assuming that the velocities $\frac{\partial}{\partial\tau}r(t)$ are considerably smaller than the deflection r, we assume the last integral is negligible. Setting again $t_2 = 0$, this leads to a different iterative formula to obtain r:

$$r(\tau_n) = \frac{1}{\gamma G}\left(\frac{\mathrm{d}}{\mathrm{d}\tau}\phi(\tau_n) - \frac{\mathrm{d}}{\mathrm{d}\tau}\phi_{\text{prior}}(\tau_n)\right) + r(\tau_{n-1}). \tag{3.26}$$

For a given n, ϕ_{prior} can be computed numerically using eq. (2.2) and the already computed $r(\tau_i)$ with $i = 0, \ldots, n-1$. The derivatives with respect to τ can also be evaluated numerically using the previously computed values of $\phi_{\text{prior}}(\tau_i)$ and the measured values $\phi(\tau_i)$.

The assumption of a constant gradient G is again only justified as long as $\Delta\tau$ is considerably larger than the length ζ of the gradient's flank. If the second derivatives of $r(\tau)$ are not too large, though, the derivatives in eq. (3.26) may be determined accurately without the need for small $\Delta\tau$. Throughout this thesis, the derivatives were calculated using central differences.

3.3.3 Least-squared Based Approach

If the motion encoding gradients are sampled as $g_0, g_1, \ldots, g_M$, with $M < N$, with the same constant sample spacing $\Delta\tau$ as ϕ, a discretization of eq. (2.2) yields

$$\begin{aligned}\phi_0 &= \gamma\Delta\tau \cdot g_M \cdot r_0 \\ \phi_1 &= \gamma\Delta\tau(g_{M-1} \cdot r_0 + g_M \cdot r_1) \\ \phi_2 &= \gamma(g_{M-2} \cdot r_0 + g_{M-1} \cdot r_1 + g_M \cdot r_2) \\ &\vdots \\ \phi_N &= \gamma\Delta\tau \sum_{i=N-M}^{N} g_{M-N+i} \cdot r_i,\end{aligned} \tag{3.27}$$

with $r_0 = r(\tau = 0)$, $r_i = r(\tau = i\Delta\tau)$ and $r = 0 \; \forall \; \tau < 0$. By combining the r_i and ϕ_i into vectors $\boldsymbol{r}$ and $\boldsymbol{\phi}$ respectively, and introducing the $N \times N$ matrix

$$\mathbf{A}_G \coloneqq \begin{pmatrix} g_M & 0 & 0 & \cdots & & 0 \\ g_{M-1} & g_M & 0 & \cdots & & 0 \\ g_{M-2} & g_{M-1} & g_M & \cdots & & 0 \\ \vdots & \vdots & \vdots & & & \\ & & & & \vdots & \vdots \\ & & & \cdots & g_M & 0 \\ 0 & 0 & 0 & \cdots & g_{M-1} & g_M \end{pmatrix}, \tag{3.28}$$

eq. (3.27) can be written as

$$\frac{1}{\gamma\Delta\tau}\boldsymbol{\phi} = \mathbf{A}_G \cdot \boldsymbol{r}. \tag{3.29}$$

This is a common approach in deconvolution problems [cf. 116, 82 sqq.]. Although there may not be an exact solution of this equation in the presence of noise, an estimate of $\boldsymbol{r}$ can be found numerically by using a least-squared approach.

4 Results

In this chapter, the results obtained during this thesis are presented and in parts briefly discussed. An extensive discussion follows in the next chapter.

The chapter is structured into five sections. The first section describes numerical simulations of the phase data of assumed trajectories of a single volume element. The second section shows results of laboratory measurements performed to test the prototype of the lifting device. The last three sections present exemplary experimental results of measurements on phantoms and vivo on a healthy volunteer as well as results of an in vivo study on four patients with diagnosed meningiomas.

4.1 Simulations

In this section results of numerical simulations are presented. These simulations were performed to test the trajectory reconstruction algorithms described in section 3.3 and to get an initial idea of what signal to expect during a measurement as described in section 2.1.

4.1.1 Test Functions

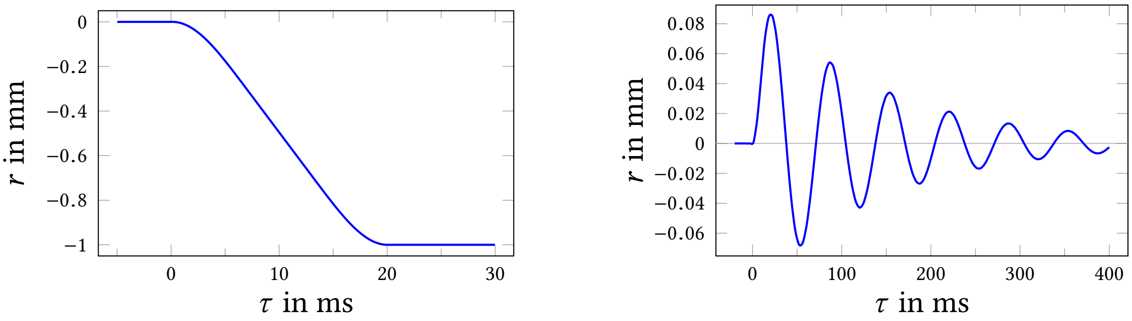

(a) *Macroskopic test function* ***(b)*** *Microscopic oscillatory test function*

Figure 4.1: *Test functions used for simulations.*
(a) represents a downward motion of 1 mm over a period of 20 ms similar to the typical motion of the movable shell, whereas (b) shows a damped oscillatory behavior similar to what is expected as responsive motion of tissue elements. For $\tau \leq 0$*, both functions equal* $r(\tau) = 0$.

All simulations in this chapter were performed using two test functions. The first one (fig. 4.1a) represents a downwards motion of 1 mm over a period of 20 ms similar to the motion of the shell of the lifting device. The second one (fig. 4.1b) represents a damped

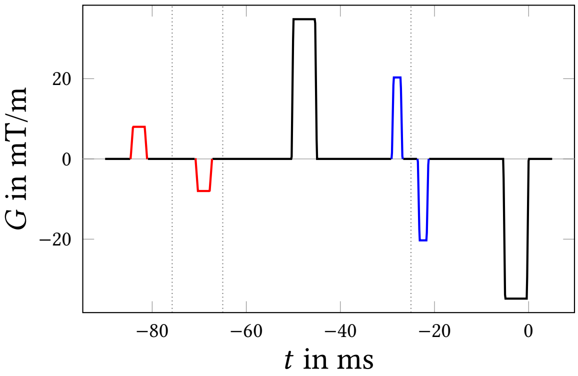

Figure 4.2: *Idealized gradient waveform: This gradient sequence was used to simulate the measurement sequence's gradients in one spatial direction. The MEGs are plotted in black, the crusher gradients of the fat saturation in red and the of the inversion pulse are plotted in blue. The location of the RF pulses (fat saturation, 90° pulse and 180° pulse) are indicated by vertical lines. In the measurement sequence, both last gradients would have opposite polarity due to the inversion of the NMR system. The end of the last gradient has been chosen as* $t_2 = 0$.

oscillation of the form $r(t) = A_0 \cdot \exp(-\beta t)\sin(2\pi f \cdot t)$ with initial amplitude $A = 100\,\mu\text{m}$, damping ratio $\beta = 7/\text{s}$ and frequency $f = 15\,\text{Hz}$. This trajectory is similar to the one expected as the response of a tissue element to the excitation (cf. section 2.1).

4.1.2 Phase Signal and Influence of Additional Gradients

In this section, the phase signal a measurement as it is described in section 2.1 would produce is investigated. For this, a single volume element that performs a specific trajectory $r(\tau)$ during the measurement was assumed.

Figure 4.2 shows an idealized version of the major gradients present in a measurement sequence[1] with $T_\text{E} = 80\,\text{ms}$ (cf. section 2.1.2). The parameters for the crusher gradients have been extracted from a simulation of the measurement sequence[2] [117]. Additional gradients, especially those present during the actual imaging process, were neglected. The gradient sequence was simplified to the spatial direction of the MEGs. It was expected, that each gradient pair present (the MEGs and both the inversion and the fat saturation crusher) will produce a similar signal, since they are all pairs of trapezoidal gradients.

This gradient waveform together with each of the test functions described in the previous section was used to calculate the expected phase signal $\phi(\tau)$ according to eq. (2.2). Since the phase ϕ is a linear mapping of G, the phase for each of the gradient pairs could be calculated separately and summed up afterwards to obtain the total phase signal. Figure 4.3 shows the calculated signals for all gradient pairs both for the macroscopic and the oscillatory microscopic trajectory. For better display, the individual contributions of the gradient pairs have been plotted out of scale.

The phase progression of the macroscopic trajectory (cf. fig. 4.3a) due to the MEGs showed a plateau with symmetric rising and falling flanks. The additional gradients each produced a smaller but similar signal, although the one of the fat saturation crushers

---

[1] MEGs: $\delta = 5.000\,\text{ms}$, $\Delta = 45.000\,\text{ms}$, $G = 25.40\,\text{mT/m}$ ($b = 50$), $\zeta = 0.361\,\text{ms}$;
fat saturation crushers: $\delta = 3.000\,\text{ms}$, $\Delta = 13.800\,\text{ms}$, $G = 8.00\,\text{mT/m}$, $\zeta = 0.501\,\text{ms}$;
inversion crusher: $\delta = 1.880\,\text{ms}$, $\Delta = 5.520\,\text{ms}$, $G = 20.30\,\text{mT/m}$, $\zeta = 0.361\,\text{ms}$

[2] IDEA Integrated Development Environment for Applications, Siemens Healthcare

did not show a plateau. The inversion crusher's signal centered around the center of the signal of the MEGs (at approx. 35.5 ms). The center of the signal produced by the fat saturation crushers was shifted to higher values of τ (86 ms).

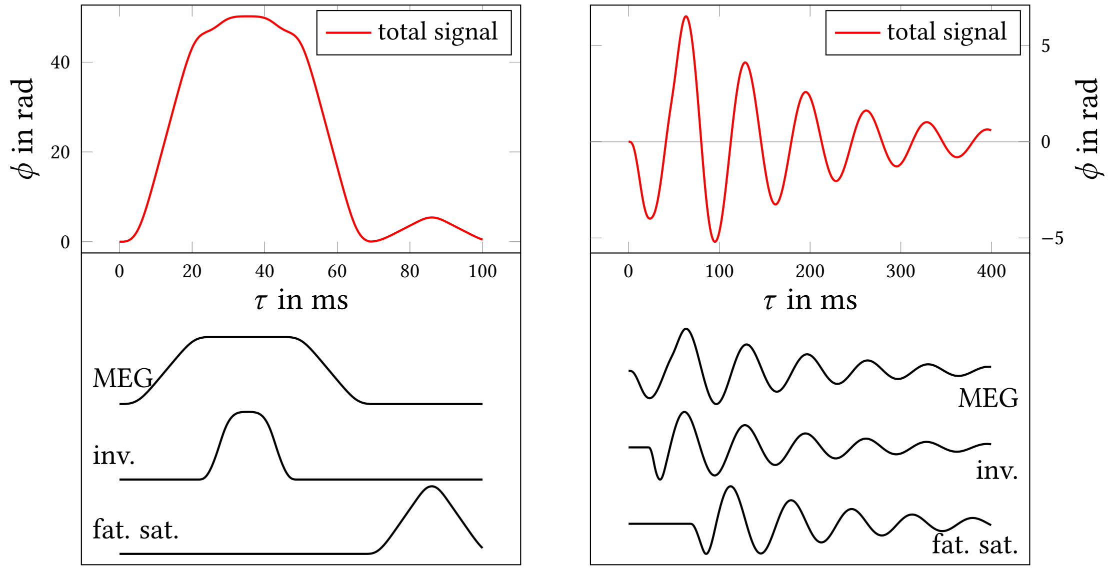

(a) *Macroscopic phase signal.*

(b) *Microscopic phase signal.*

Figure 4.3: *Phase signals produced by the test gradient sequence:*
Using eq. (2.2)*, the phase progression that a measurement with the test sequence (cf. fig. 4.2) would yield for each trajectory in section 4.1.1 was calculated. The total phase signal is shown in red in the top panel, the individual contributions of the gradient pairs are indicated in black in the lower panel. Note that the ordinate of these is not in true scale. (a) shows the results for the macroscopic trajectory. For τ-values greater than the ones shown, the phase equals zero. (b) shows the results of the microscopic oscillatory trajectory.*

With the oscillatory trajectory (cf. fig. 4.3b), the signal of the MEGs was again an oscillation very similar to the one of the trajectory. The additional gradients each created a smaller oscillation, too. The maximum value of the MEG signal was 6.1 rad, while the maximum values of the signals of the inversion and the fat saturation crushers were 0.4 rad and 0.6 rad respectively. As with the macroscopic trajectory, the signal of the inversion crusher gradients was not shifted relative to the MEGs' signal, whereas the signal of the fat saturation crushers showed a phase shift. The total signal therefore was a beat frequency. While the signal of the macroscopic trajectory seemed to be noticeable distorted, the total oscillating signal does not differ much from the one resulting only from the MEGs. This effect might be larger with other sequence parameters and therefore with different phase shifts or with other frequencies of the oscillation, though.

As expected, the simulated signals of the different gradient pairs are qualitatively equal. The exact form of such a signal then depends on the gradient pairs' length and strength. The temporal shifts of the additional signals are easily explained by the location of the corresponding gradients in the sequence. The shifts between the starts of those signals equals the distance between the end points of the corresponding gradient pairs in the sequence.

For both trajectories, the maximum of the signal of the inversion crusher gradients was about 10 % and the maximum of the signal of the fat saturation crushers was about 15 % of the signal of the MEGs.

4.1.3 Comparison of Trajectory Reconstruction Algorithms

To test the performance and accuracy of the three trajectory reconstruction algorithms described in section 3.3, the idealized gradient waveform used in the last section (cf. fig. 4.2) was further simplified by using only the MEGs. The calculated phase signals of these gradients (cf. fig. 4.3, label "MEG") have been sampled with different sample spacings ($\Delta\tau = 1\,\text{ms}$, 2 ms and 4 ms) to create sampled phase data. Each of the three algorithms described above were used to reconstruct the trajectory $\tilde{r}(\tau)$ from every set of phase data.

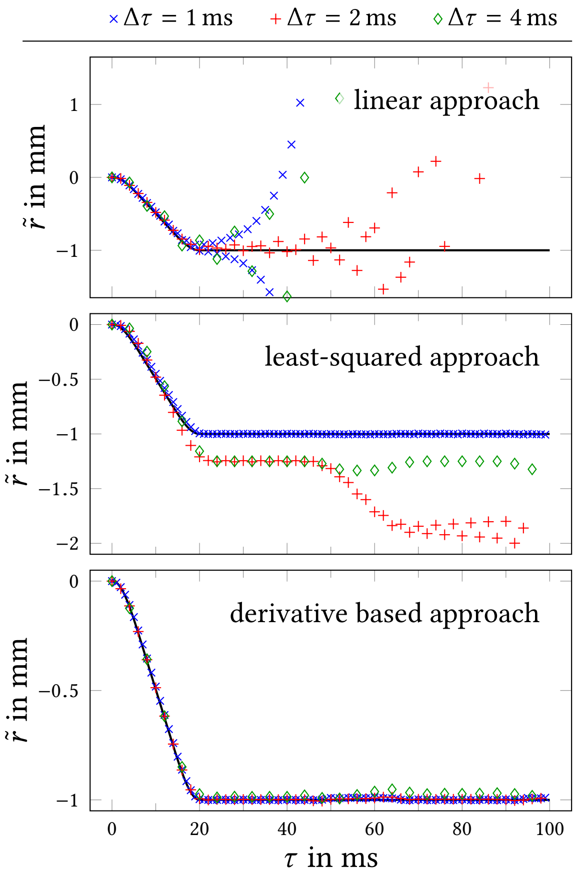

Figure 4.4: *Reconstruction of the macroscopic trajectory.*
Samples $\tilde{r}(\tau)$ of the macroscopic trajectory have been reconstructed from differently sampled phase data with all three reconstruction approaches. For comparison, the original trajectory $r(\tau)$ is plotted in black.
The data reconstructed using the linear approach heavily oscillates around the original trajectory for $\tau > 20\,\text{ms}$. This effect is smallest for the samples with $\Delta\tau = 2\,\text{ms}$, though for larger τ, those values deviate to a great extent, too. The amplitude of the oscillation seems to increase exponentially to very large numbers. To allow inspections of the results for small τ, the plot limits of the ordinate have been adjusted.
The reconstruction using the least-squared approach is accurate only with the small sample spacing ($\Delta\tau = 1\,\text{ms}$). Coarser spacing leads to incorrectly reconstructed trajectories.
The derivative based reconstruction worked well for all sample spacings. For larger $\Delta\tau$ a small deviation after $\tau \approx 50\,\text{ms}$ emerges.

The results for the macroscopic test trajectory (cf. fig. 4.1a) are shown in fig. 4.4. The positions reconstructed using the linear approach (upper panel, cf. eq. (3.24)) initially followed the original trajectory with some minor deviations up to the point were the trajectory leveled out. With increasing τ, the reconstructed points oscillated increasingly heavily around the original trajectory. The performance with $\Delta\tau = 1\,\text{ms}$ and 4 ms were comparable, while the algorithm was able to reconstruct the trajectory slightly better from the phase data sampled with $\Delta\tau = 2\,\text{ms}$. However, this approach is clearly not feasible and has therefore been excluded from further investigations.

In the case of the least-squared based matrix formulation (middle panel, cf. eq. (3.29)), only the positions reconstructed with $\Delta\tau = 1\,\text{ms}$ followed the original trajectory. With $\Delta\tau = 2\,\text{ms}$ and 4 ms, $\tilde{r}$ showed a steeper downward motion and a larger final displacement. $\tilde{r}(\Delta\tau = 2\,\text{ms})$ did not level out at all and additionally showed some oscillatory behavior starting at about 70 ms.

The derivative based approach (lower panel, cf. eq. (3.26)) performed significantly better than the other two approaches, since the trajectory was reconstructed correctly for all three phase data sets. A small deviation occurred from $\tau \approx 50\,\text{ms}$ to 65 ms that was more distinct with higher $\Delta\tau$.

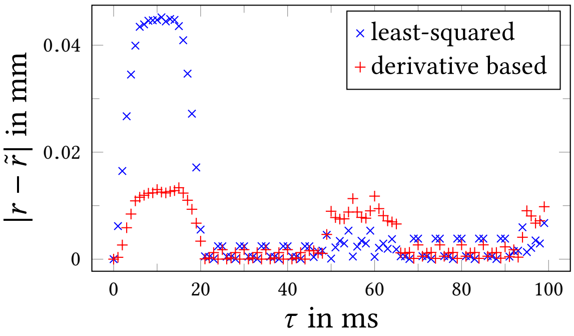

Figure 4.5: *Comparison of the reconstruction algorithms:*
Plotted is the absolute deviation $|r(\tau) - \tilde{r}(\tau)|$ between the original trajectory r and the reconstructed trajectories $\tilde{r}$ for $\Delta\tau = 1\,\text{ms}$. The linear reconstruction approach is not shown.

To compare the performance of the least-squared approach and the derivative based approach with $\Delta\tau = 1\,\text{ms}$, the absolute difference $\Delta r = |r - \tilde{r}|$ of the original and the reconstructed trajectories are plotted against τ in fig. 4.5. Both algorithms show the largest differences at $\tau < 20\,\text{ms}$ during the actual motion of the original trajectory. The maximum difference of the least-square based algorithm are approximately three times as large as the maximum difference of the derivative based algorithm ($\Delta r_{\text{max}} \approx 45\,\mu\text{m}$ to $\Delta r_{\text{max}} \approx 13\,\mu\text{m}$). Both algorithms show an increase of Δr starting at $\tau \approx 45\,\text{ms}$ for about 20 ms and a second one starting at $\tau \approx 95\,\text{ms}$. The distance between those two events equals the total length of the two gradients that were used to calculate the phase data.

The results of the microscopic oscillatory trajectory (cf. fig. 4.1b) are shown in fig. 4.6. Note the longer range of τ-values compared to the previous results.

Matching the results obtained with the macroscopic trajectory, the least-squared approach (upper panel) reconstructed the positions $\tilde{r}$ correctly for $\Delta\tau = 1\,\text{ms}$. Even for $\Delta\tau = 4\,\text{ms}$ the reconstruction worked reasonably well. For $\Delta\tau = 2\,\text{ms}$, however, the reconstruction failed for $\tau > 100\,\text{ms}$. The positions reconstructed with the derivative based approach (lower panel) follow the original trajectory nicely over the whole range of τ. Only the reconstruction of the phase data sampled with $\Delta\tau = 4\,\text{ms}$ accumulated a slight offset with increasing τ.

The performance of the least-squared and derivative based algorithms was additionally tested in the presence of additive gaussian noise. The quality of a noisy signal is

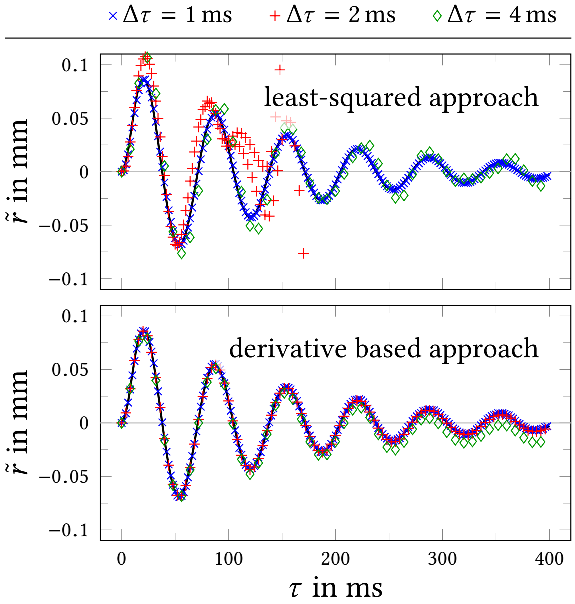

Figure 4.6: *Reconstruction of an oscillatory trajectory:*
Samples $\tilde{r}(\tau)$ of the microscopic trajectory have been reconstructed from the sampled phase data. For comparison, the original trajectory $r(\tau)$ is plotted in black. It is hidden behind the blue data points. The reconstruction using the least-squared failed for a sample spacing of $\Delta\tau = 1\,\text{ms}$ but worked reasonably well otherwise. The derivative based approach worked well with all sample spacings but accumulated a slight offset with $\Delta\tau = 4\,\text{ms}$.

characterized by the SNR. For this work, the following definition of SNR was used [118]:

$$Q = \sqrt{\frac{P_\phi}{\sigma^2_{\text{noise}}}} \quad \text{with} \quad P_\phi = \frac{1}{t_2 - t_1} \int_{t_1}^{t_2} \phi^2(t)\, dt, \tag{4.1}$$

with the standard deviation σ_{noise} of the noise. For testing, random samples from a gaussian distribution were added to the sampled phase data of the macroscopic test function with $\Delta\tau = 1\,\text{ms}$. The standard deviation of the distribution was chosen such that an SNR of 50, 100 and 200 was achieved ($\sigma_{\text{noise}} = 0.420$, 0.210 and 0.105 according to eq. (4.1)).

The trajectories $\tilde{r}$ reconstructed from these noisy phase samples for both the least-squared approach as well as the derivative based approach are shown in fig. 4.7. Both reconstructed time series oscillate around the original trajectory. These oscillations grow stronger with higher τ and with lower SNR. In all cases the derivative based algorithm performed significantly better than the least-squared approach. The deconvolution of the oscillatory trajectory with added noise are not shown here, since they qualitatively show the same results like the one with the macroscopic trajectory.

In summary, the reconstruction of the oscillatory trajectory seems to work better in general than of the macroscopic trajectory, which might be due to the fact that its progression is more continuous. With a sample spacing of $\Delta\tau \leq 2\,\text{ms}$, however, the derivative based approach seems to produce reliable results for both cases. Reconstructing 100 datapoints lasted 3 ms with the least-squared approach and 55 ms using the derivative based approach. Regarding run time, thus, the least-squared based approach should be preferred, as it is ten times faster than the derivative based one. Regarding the deconvolution of measurement data, especially with relatively low SNR, noise reduction in the phase data prior to reconstruction is clearly inevitable for both approaches.

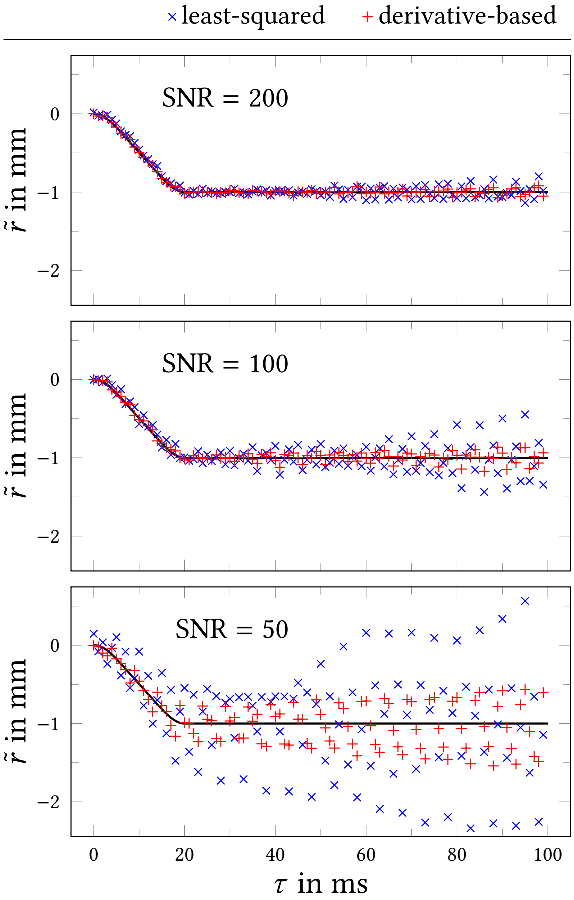

Figure 4.7: *Reconstruction of noisy phase data. Gaussian noise was added to the sampled phase data of the macroscopic trajectory. The noisy phase data was used to reconstruct the trajectory $\tilde{r}$ with the least-squared and the derivative based approach. With lower SNR and higher τ the reconstructed positions $\tilde{r}$ oscillate stronger around the original trajectory. The derivative based approach seems to be more reliable.*

4.2 Laboratory Measurements

In this section, measurements that were performed under laboratory conditions are presented. Two measurements have been conducted: one regarding the temporal stability of the OPMs' LEDs and one investigating the acceleration profile of the falling motion.

4.2.1 Stability of the Optical Control System

During this thesis, the OPMs (cf. section 2.1.1.2) were used to monitor and reconstruct the trajectory of the movable shell of the lifting device during the experiment (cf. section 3.1). Since this reconstruction is based on the measurement of the transmitted light, it was important that the emitted light intensity of the LEDs remained unchanged during the experiment. This has been tested under laboratory conditions with the exact set up used in the actual measurement for all three used LEDs. Figure 4.8 shows the measured voltage of the photo diodes of the three LEDs as a function of the time t after connecting them to the power supply unit. Two of the three diodes show a long transient until they reach a stable output voltage after approximately 1 h.

It was not tested in detail whether this transient was produced by the photo diodes or the LEDs, and what the origin of this effect was. However, in all MRR measurement

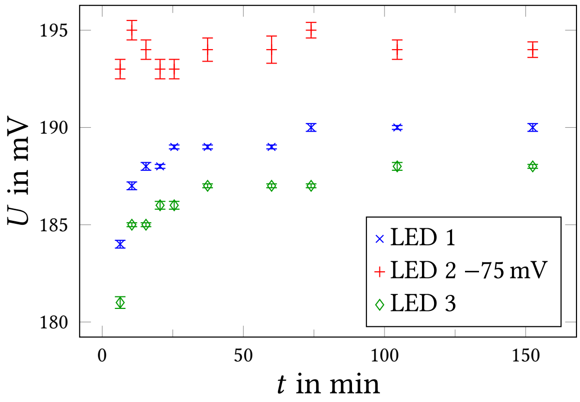

***Figure 4.8:** Temporal stability of the LEDs. The voltage of the photo diodes of the OPMs were measured at several points in time after connecting the LEDs to the power supply unit. Only after more than one hour are the measured voltages roughly constant.*

presented in this thesis, the exact same set up of the OPMs was used. Due to these results, we made sure the optical system was activated at least one hour prior to any actual measurement.

4.2.2 Acceleration Measurements

The optical measurement of the shell motion (cf. section 2.1.1.2) monitors the position over time. Since the excitation of the brain tissue depends on the acceleration of the cranial bone, it was tested to what extent this acceleration can be extracted from that measurement.

For that, the whole equipment was assembled in the laboratory outside the MRI scanner. The shell was loaded with lead weights to make up for the weight of the proband's head.

The shell was then equipped with an accelerometer[3] right above one of the OPMs. The optical positioning sensor was calibrated as described in section 2.1.1.2 and both the optical signal and the acceleration signal after a drop of the shell were recorded. This was repeated five times for all three locations of the OPMs. The accelerometer provided the acceleration in multiples of the gravitational acceleration. Its signal has been sampled with a sample rate of 10 kHz and the voltage of the photo diode U with a sample rate of 250 kHz, although the bandwidth of the diode itself was only 14 kHz.

Due to the supposed linear relation of U and the position of the shell (cf. section 2.1.1.2), the acceleration could be calculated using

$$y(t) = m \cdot U(t) + y_0 \tag{4.2}$$

$$\ddot{y}(t) = m \cdot \ddot{U}(t) \qquad \sigma^2(\ddot{y}) = \sigma^2(m) \cdot \ddot{U}, \tag{4.3}$$

with the slope of the linear calibration m.

For computing this, the measured voltage U of the photo diode was smoothed as described in section 3.1 using a window length of 4001 samples ($\equiv$ 16 ms). This strong smoothing ensured that no high frequency oscillations due to measurement noise remained in the data. A spline representation $\tilde{U}$ of fifth degree was then fitted to the data and the second temporal derivative of that spline was computed. The degree of the spline was

---

[3] 3D acceleration sensor S, LD DIDACTIC GmbH, Hürth, Germany

chosen in that way to be able to readily compute the second derivative. The acceleration was then computed using eq. (4.3) and $\ddot{U} = \frac{\mathrm{d}^2}{\mathrm{d}t^2}\tilde{U}$.

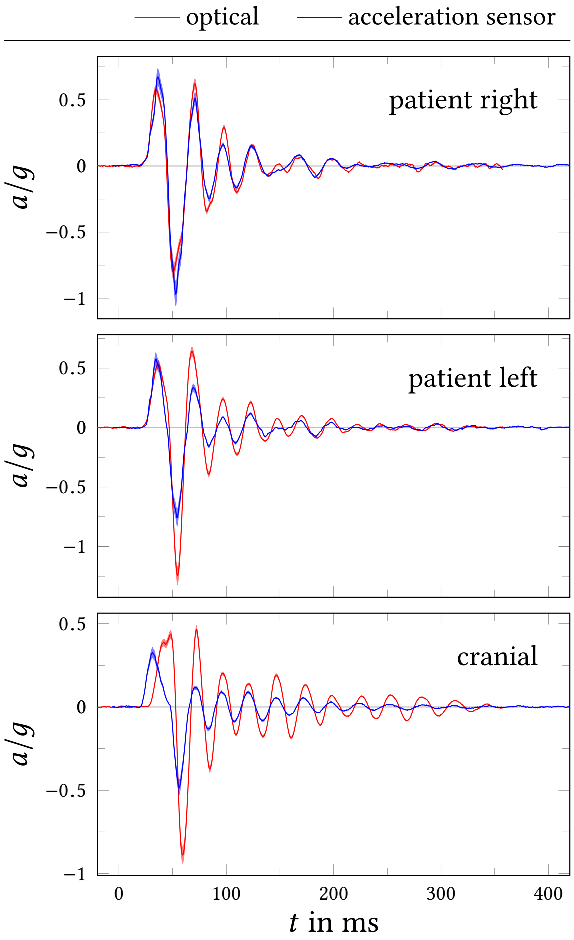

Figure 4.9: *Acceleration of the shell.*
The acceleration of the shell has been measured consecutively at all three locations of the optical position measurement system with an accelerometer. Simultaneously, the data of the optical position measurement system was recorded and the acceleration determined from this signal. Both data sets are plotted next to each other showing the acceleration in the reference frame of the shell in multiples of $g = 9.81\,\mathrm{m/s^2}$. *The data of the accelerometer has been shifted by 6 ms on the time axis to account for a delay in the recording system. The small errorband of the optical signal was determined by the standard deviation of the linear calibration fit. The accelerometer data is assumed to have a standard deviation of 10 %.*

The results of the five repetitions of the measurements all yielded almost identical results. Figure 4.9 therefore only shows the results of the first measurement on each of the three optical measurement positions. The readout system of the accelerometer was delayed, so the corresponding graphs were shifted by 6 ms. The measured accelerations matched the ones reconstructed from the measured position, although the magnitude of the optical data was larger at some points. The data from the cranial measurement position showed a larger deviation in the beginning of the progression. The source of that deviation is currently unknown.

The acceleration progression showed that the shell did not come to a rest soon after the landing, but performed several oscillations on the rubber of the pneumatic hoses over a course of at least 100 ms. The frequency of this oscillation can be estimated to 38 Hz.

4.3 Phantom Measurements

In this section measurements on agar based phantoms are presented. The first part describes a measurement on a homogeneous phantom without induced motion to investigate the stability of the phase measurement of the MRI scanner. In the second part measurements on inhomogeneous phantoms are presented.

4.3.1 Phase Stability

In a measurement on a healthy volunteer, Ulucay [40, 69] found in an analysis of MRR images obtained without motion, that the phase measured in a single voxel as well as the mean phase of the entire image fluctuated in a range of $\frac{\pi}{2}$. In order to investigate this further, a homogeneous agar hydrogel phantom was placed into the lifting device in the scanner and a series of measurements without motion was conducted. The movable shell was in the lower position during this measurement, i. e. the pneumatic system was vented and the movable shell rested on the empty rubber hoses. The sequence parameters were chosen as follows: $T_E = 80\,\mathrm{ms}$, $T_R = 3000\,\mathrm{ms}$, $\delta = 5\,\mathrm{ms}$, $\Delta = 45\,\mathrm{ms}$ and $G = 34.07\,\mathrm{mT/m}$, the voxel sizes were $1.3 \times 1.3 \times 5\,\mathrm{mm}^3$. 150 images were acquired without interruption. Because the pneumatic system was not fully vented yet when the measurement started, the first two images were discarded, leaving a total of 148 images.

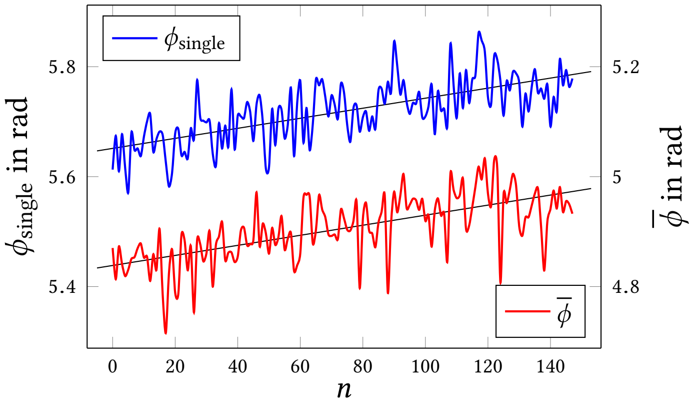

Figure 4.10: *Reproducibility of the measured phase: A homogeneous agar hydrogel phantom was measured using the full MRR setup up but without induced motion. The movable shell including the phantom container rested on the vented rubber hoses. Both the phase ϕ_{single} of a single arbitrary voxel and the mean phase $\bar{\phi}$ of the entire phantom region of the measured slice show a random fluctuation and a trend towards higher values. To guide the eye, a linear regression has been computed on both data sets and plotted in black.*

Figure 4.10 shows, similar to the data obtained by Ulucay, the phase ϕ_{single} of an arbitrary single voxel and the mean phase $\bar{\phi}$ of the entire phantom region as a function of the image number n. It was verified that no air bubbles were enclosed in the measured slice that might alter the phase. Both ϕ_{single} and $\bar{\phi}$ fluctuate in a random fashion, although a slight drift towards higher values is observable. To quantify this trend linear regressions have been performed on both progressions: The slopes of these are 9.13×10^{-4} rad/image and 9.15×10^{-4} rad/image for ϕ_{single} and $\bar{\phi}$ respectively. Using the specified repetition time, this translates to 3.05×10^{-4} rad/s. Over all acquired images, ϕ_{single} varied over a range of 0.3 rad with a standard deviation of $\sigma(\phi_{\text{single}}) = 0.06$ rad. This value is one magnitude smaller than the one observed by Ulucay.

Ulucay found that the phase of a single voxel and the mean phase of the ROI behaved similar up to a constant offset and deduced the reason for the fluctuations might be a non-constant reference phase of the MRI scanner. However, this identical dynamics were not observed in the measurement presented here. Ulucay used a different gradient setting ($\delta = 15$ ms, $\Delta = 55$ ms and $G = 22.29$ mT/m) resulting in a b-value approximately four times larger than the one used here. A fluctuation in the reference phase, however, should not scale with the parameters of the MEGs. Ulucay obtained data in vivo, while the data here was obtained from a phantom. Physiological processes (e. g. blood or CSF pulsations) might lead to motion in the brain that can alter the measured phase. However, it seems unlikely, that such a process would alter the mean phase of the ROI in such a large range. Ulucay is not clear in the details on how the measurements were obtained. Based on his descriptions and the results presented here, it seems likely that he measured in the upper position with the movable shell resting on the filled rubber hoses. The fluctuations he observed might have resulted from vibrations of the MRI scanner transfered to the lifting device or involuntary movement of the volunteer. Whether the linear trend observed here was present in Ulucay's data could not be determined due to the form of display and the large spread of the fluctuations. This trend might indeed originate from the MRI scanner's phase measurement.

4.3.2 Inhomogeneous Phantoms

In this section, results of measurements on two agar based hydrogel phantoms are presented. They serve as an indicator of the influence of the agar concentration (and with that stiffness) and the density of the material on the generated displacements. Kofahl did a more thorough analysis of agar based phantoms [38, 98].

The experiments have been conducted as described in section 2.2.1 and the data has been processed as described in section 3.2.

4.3.2.1 Phantom I

Phantom **I** consisted of two layers of different agar concentration that resulted in Young's moduli of 11.6 kPa respectively 17.4 kPa (cf. section 2.2.1).

The phantom was placed in the movable shell so that the stiffer layer was located at the right side and the softer layer was on the left side.

Figure 4.11 shows a high resolution magnitude image and a time series of 9 averaged phase images. In the magnitude image, the two layers can be distinguished by their different intensity. This is due to the fact, that the signal strength in the magnitude image is weighted by the T_2 of the material, which is in turn affected by the agar concentration [119]. The phase images reveal a complex spatial oscillation pattern inside the phantom material. The amplitude of these oscillations increases with higher values of τ. As expected, the image with $\tau = 0$ ms shows an homogeneous gray value except for some measurement

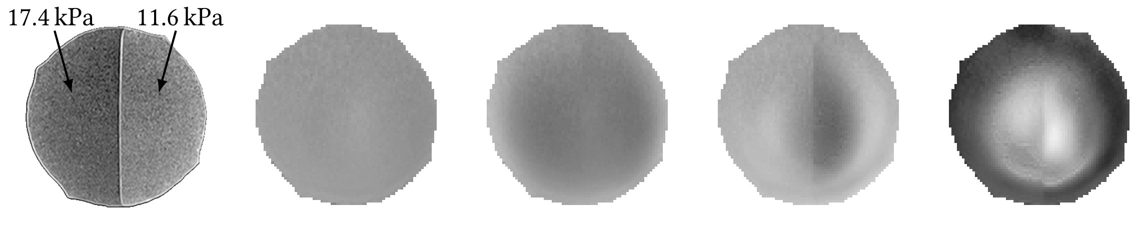

(a) *Magnitude* ***(b)*** $\tau = 0\,\mathrm{ms}$ ***(c)*** $\tau = 11.0\,\mathrm{ms}$ ***(d)*** $\tau = 22.0\,\mathrm{ms}$ ***(e)*** $\tau = 33.5\,\mathrm{ms}$

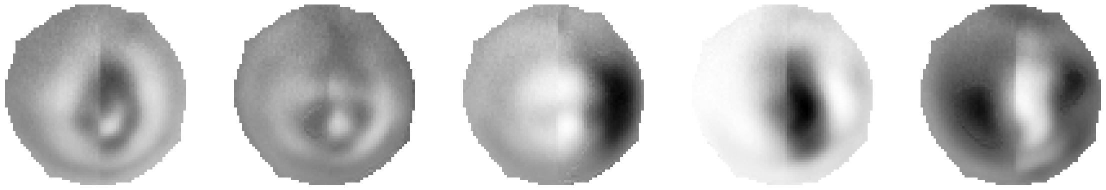

(f) $\tau = 44.5\,\mathrm{ms}$ ***(g)*** $\tau = 55.5\,\mathrm{ms}$ ***(h)*** $\tau = 66.5\,\mathrm{ms}$ ***(i)*** $\tau = 78.0\,\mathrm{ms}$ ***(j)*** $\tau = 89.0\,\mathrm{ms}$

Figure 4.11: *Representative phase images of Phantom **I**:*
(a) shows a high-resolution magnitude image of the measured transversal slice. The phantom's layer on the patient's right side had a higher agar concentration than the layer on the patient's left side, and was therefore stiffer (E = $11.6\,\mathrm{kPa}$ *resp.* $17.4\,\mathrm{kPa}$*). The border between both layers is visible as a hyper intense line. (b) to (j) show phase images of the same slice acquired with different values of* τ. *All images are averages of 5 or 10 measurements and were corrected by the baseline image. At* $\tau = 0\,\mathrm{ms}$, *the phase shows an almost flat gray value. With increasing* τ, *the contrast enlarges and a complex oscillation pattern becomes visible. Evidently the two different layers of hydrogel behave differently as the boundary of the two regions is visible in all images with* $\tau > 0\,\mathrm{ms}$.

noise in the top region of the phantom. For this image, the induced motion did only start after the motion encoding was finished. As one would expect, the oscillations in the softer layer of the phantom show more dynamics than the one in the stiffer layer (cf. e.g. fig. 4.11g). This makes it possible to distinguish the two layers and locate their border by eye easily in the images figs. 4.11d–j.

Some of the phase images (figs. 4.11e, 4.11g and 4.11j) show phase unwrapping artifacts in the form of lines at the position of phase discontinuities in the original wrapped phase images as described in section 3.2.1.

The absolute value of the calculated phase strain (cf. section 3.2.4) is shown in fig. 4.12 for the same values of τ as before. $\tau = 0\,\mathrm{ms}$ is not shown, since the corresponding phase image already did not show any contrast. The strain distribution in the measured slice shows a complex pattern of regions with higher and lower strain, as was expected from the phase images. Although the values of $|\epsilon_\phi|$ seem to be slightly lower in the stiffer layer of the phantom, it is hard to identify the border of the two layers in the strain images.

Figure 4.12b shows the integrated absolute phase strain $\epsilon_{\phi,\,\mathrm{total}}$ (cf. eq. (3.18)). Here, the distinction of the two layers is obvious by the much higher values in the softer layer of the phantom. At the same time, an influence of the geometry of the phantom is apparent: The central left and right regions show smaller values than the center, and the bottom shows

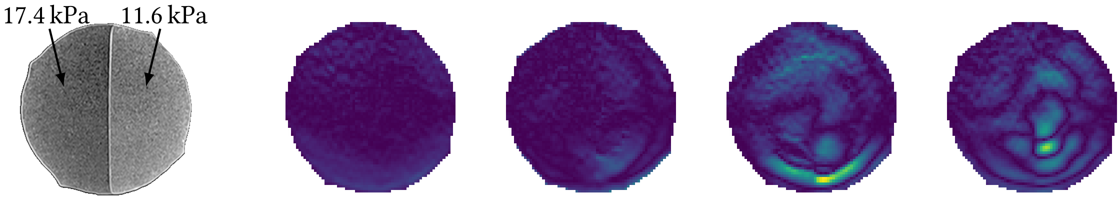

(a) *Magnitude* ***(c)*** τ = 11.0 ms ***(d)*** τ = 22.0 ms ***(e)*** τ = 33.5 ms ***(f)*** τ = 44.5 ms

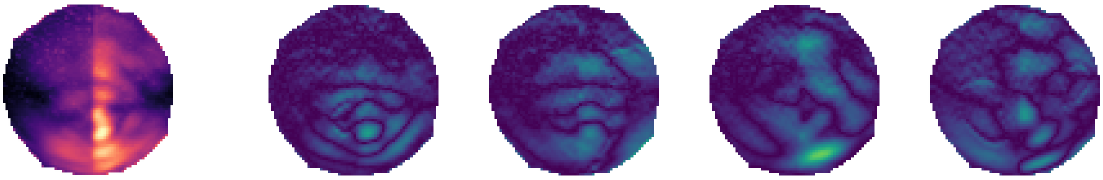

(b) $\epsilon_{\phi,\,\mathrm{total}}$ ***(g)*** τ = 55.5 ms ***(h)*** τ = 66.5 ms ***(i)*** τ = 78.0 ms ***(j)*** τ = 89.0 ms

Figure 4.12: *Absolute phase strain of phantom* **I***:*
(a) shows the high resolution magnitude image of the measured transversal slice. (c) to (j) show the calculated absolute phase strain $|\epsilon_\phi|$ *at different values of* τ*. Similar to what was expected from the phase images in fig. 4.11 the strain shows a complicated pattern of areas with high and low strain. (b) shows the temporally integrated absolute phase strain* $\epsilon_{\phi,\,\mathrm{total}}$*. The stiffer layer of the phantom clearly experienced less strain than the softer one, as one would expect. Additionally, it becomes obvious that the response of the material to the excitation is also dependent on the geometry of the phantom. The roughly concentric spatial distribution of regions of higher and lower strain suggests a resonant oscillation of higher order.*

slightly higher values than the top of the phantom. The pattern of the strain distribution seems to fit the hypothesized excitation of resonance frequencies (cf. section 2.1), albeit the measured oscillation seems to be a mode shape of higher order.

4.3.2.2 Phantom II

Phantom **II** consisted of two layers of equal agar concentration but different densities of $\rho = 1.0\,\mathrm{g/cm^3}$ and $\rho = 1.2\,\mathrm{g/cm^3}$ (cf. section 2.2.1).

The phantom was placed in the movable shell so that the denser layer was located at the left side and the less dense layer on the right side.

Figure 4.13 shows again a high resolution magnitude image of the measured slice and a series of 9 phase images post processed as described in section 3.2. In the magnitude image, the border between the two layers is barely visible as a thin darker line. At the posterior end, the border shows up as a hyper intense line. This may be an indicator that the two layers were disconnected there and water gathered in the gap. In the less dense layer, a hyper intense band running in the anterior-posterior direction is visible. The origin of this band is unknown.

The phase images show a similar behavior to the ones of phantom **I**: At $\tau = 0\,\mathrm{ms}$, the phase image shows no contrast but a homogeneous gray value (cf. fig. 4.13b). The images for later values of τ reveal again a global oscillation of the phantom material. Except for

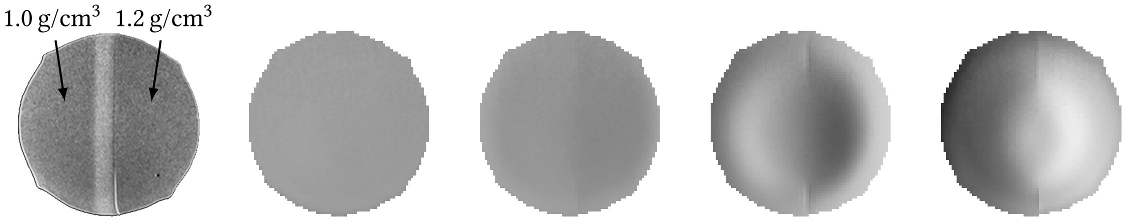

(a) *Magnitude* ***(b)*** $\tau = 0\,\mathrm{ms}$ ***(c)*** $\tau = 11.0\,\mathrm{ms}$ ***(d)*** $\tau = 22.0\,\mathrm{ms}$ ***(e)*** $\tau = 33.5\,\mathrm{ms}$

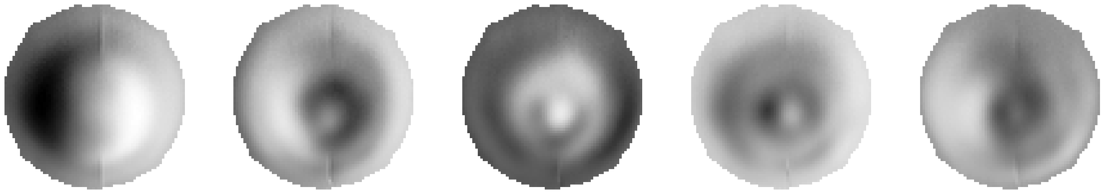

(f) $\tau = 44.5\,\mathrm{ms}$ ***(g)*** $\tau = 55.5\,\mathrm{ms}$ ***(h)*** $\tau = 66.5\,\mathrm{ms}$ ***(i)*** $\tau = 78.0\,\mathrm{ms}$ ***(j)*** $\tau = 89.0\,\mathrm{ms}$

Figure 4.13: *Representative phase images of phantom* ***II****:*
Fig. (a) shows the high resolution magnitude image fo the measured transversal slice. Figs. (b) to (j) show phase images of the same slice acquired at different values of τ*. All images are averages of 5 or 10 measurements and were corrected by the baseline image. At* $\tau = 0\,\mathrm{ms}$*, the phase shows an almost flat gray value, as expected. With increasing values of* τ*, a global oscillation becomes apparent. Contrary to the result with phantom* ***I****, the two layers seem to behave very similar.*

the anterior and posterior ends, the border of the two layers is not visible, though. In general, the two layers seem to behave similar.

An inspection of the absolute phase strain images in fig. 4.14 reveals again a complex pattern of areas with higher and lower strain. Again, the two layers seem to behave similar. Only in the image depicting the integrated absolute phase strain $\epsilon_{\phi,\,\mathrm{total}}$ it becomes visible that the denser layer experienced more strain than the less dense one. The difference is much less than the one observed for phantom **I**, though. As with phantom **I**, the excited oscillations look like a mode shape of higher order.

4.3.2.3 Relative Phase Progression

For both phantoms the phase $\Delta\phi_r$ relative to a reference was calculated as described in section 3.2.3. Since there is no area without expected motion in the center of the presented phantoms, the reference has been chosen as the mean phase of the outermost voxels of the center line of the ROI. Since eq. (3.11) does not hold true in this case, the phase images had to be unwrapped individually prior to the computation of the relative phase. Figure 4.15 shows $\Delta\phi_r$ for a single voxel in each layer of both phantoms.

The progression in phantom **I** (cf. fig. 4.15a) shows very small standard errors, depicted by the errorband that is hardly visible. Nevertheless, the data scatters strongly around the apparent progression. Both voxels show a similar oscillation. At larger values of τ, the amplitude of the voxel in the stiffer layer is slightly reduced compared to the other one. However, the distinction of the two layers, that was possible using the phase images

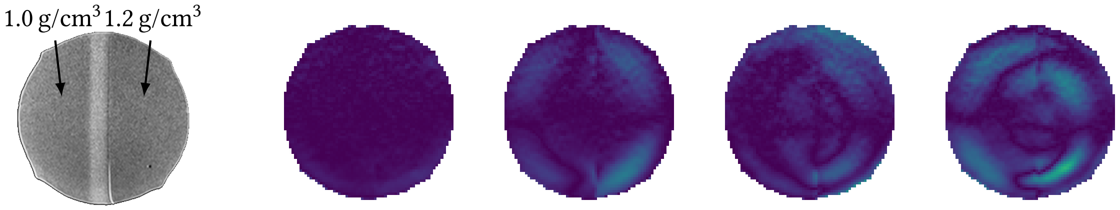

(a) *Magnitude* ***(c)*** $\tau = 11.0\,\mathrm{ms}$ ***(d)*** $\tau = 22.0\,\mathrm{ms}$ ***(e)*** $\tau = 33.5\,\mathrm{ms}$ ***(f)*** $\tau = 44.5\,\mathrm{ms}$

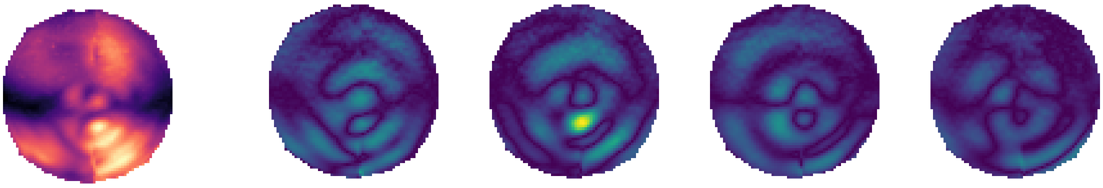

(b) $\epsilon_{\phi,\,\mathrm{total}}$ ***(g)*** $\tau = 55.5\,\mathrm{ms}$ ***(h)*** $\tau = 66.5\,\mathrm{ms}$ ***(i)*** $\tau = 78.0\,\mathrm{ms}$ ***(j)*** $\tau = 89.0\,\mathrm{ms}$

Figure 4.14: *Absolute phase strain of phantom* ***II****:*
(a) shows the magnitude image of the measured transversal slice. (c) to (j) show the calculated absolute phase strain $|\epsilon_\phi|$ *at different values of* τ*. Similar to what was expected from the phase images in fig. 4.13 and the results of phantom* ***I****, a complex pattern of regions with higher and lower strain is visible. Both different layers seem to behave similar though, and the border of the layers is not visible. (b) shows the temporally integrated absolute phase strain* $\epsilon_{\phi,\,\mathrm{total}}$*. Both layers experienced similar strain, although the denser layer shows slightly higher values. Similar to what was observed in phantom* ***I****, the spatial distribution of the strain suggests a higher order resonant oscillation of the material.*

(cf. fig. 4.11) is not possible on the basis of this data.

Figure 4.15b shows the progression of two voxels in the two layers of phantom **II**. Here, the scattering effect is not present except for a few τ-values. The standard error is very small, so that the errorband is not visible. The voxel in the denser layer shows a larger initial deflection. Approximately starting at $\tau =\approx 25\,\mathrm{ms}$, both voxels oscillate in phase opposition, albeit with comparable amplitude.

These results do not match the analysis of the phase images (cf. figs. 4.11 and 4.13) and the phase strain images (cf. figs. 4.12 and 4.14). However, as was observed there, the oscillation pattern in these phantoms is complex. Most likely, the two phase progressions shown for phantom **II** show a phase shift simply due to the specific choice of the voxels.

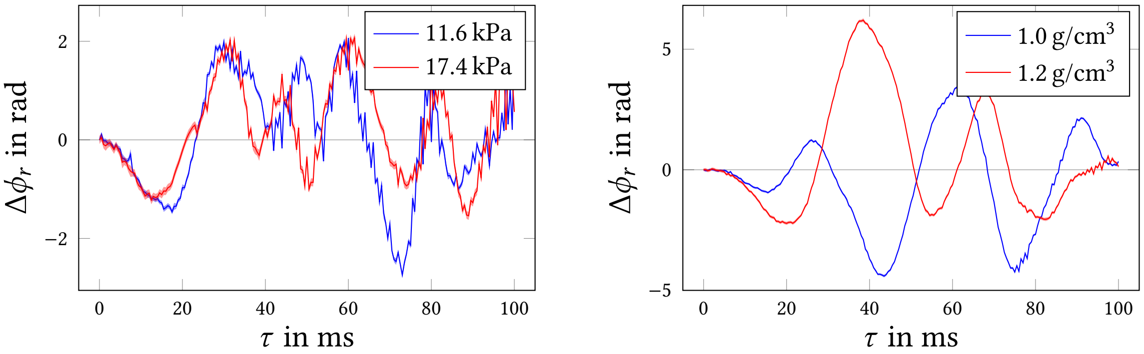

*(a) Phantom **I***

*(b) Phantom **II***

Figure 4.15: *Relative phase progression of the inhomogeneous phantoms.*
*For both both phantoms the relative phase $\Delta\phi_r$ has been computed. The computation was slightly different than described in section 3.2.3, for details see the description in the text. (a) shows the phase progression of one voxel in each layer of the phantom. The data shows large scattering around the apparent progression albeit a very small standard error indicated by the errorband. (b) shows the same plot for two voxel of phantom **II**. Here, the scattering is almost not visible. The standard error is very small, so that the errorbar is not visible.*

4.4 Healthy Volunteers

During the course of this thesis, the concept of MRR was tested on several healthy volunteers. In this section, the results of one 30 years old male volunteer are presented. They are representative for all measurements.

The experiment has been performed as described in sec. 2.2.2, resulting in a time series with values of τ from 0 ms to 400 ms with a $\Delta\tau$ of 1 ms and 5 ms and $N_\tau = 5$. The phase images were processed as described in section 3.2.

4.4.1 Phase Images

In fig. 4.16 a high resolution magnitude image and seven phase images at different values of τ are shown. These illustrate the general behavior of the brain tissue after the shock excitation performed in MRR. Similar to what was observed with the agar hydrogel phantoms, the phase image at $\tau = 0$ ms (a) shows an almost homogeneous gray value without contrast. The other phase images show an increasing contrast with increasing τ ((c) to (f)), that decreases again in images (g) and (h). Most prominently, the separation of the hemispheres becomes visible with the division along the falx cerebri (cf. section 1.2.1). Both hemispheres individually show an oscillation in gray values. The oscillation pattern is less complex than it was the case for the phantoms. In some images, small structures in the outer regions near the sulci become visible, especially in images (e) and (f).

The results in section 4.1.2 showed that a downwards motion (positive y axis in the DPCS) produces a positive phase signal. Therefore, in the phase images shown here, areas that appear lighter than the border regions were deflected downwards relative to the cranial bone, whereas areas that appear darker than the border regions were deflected

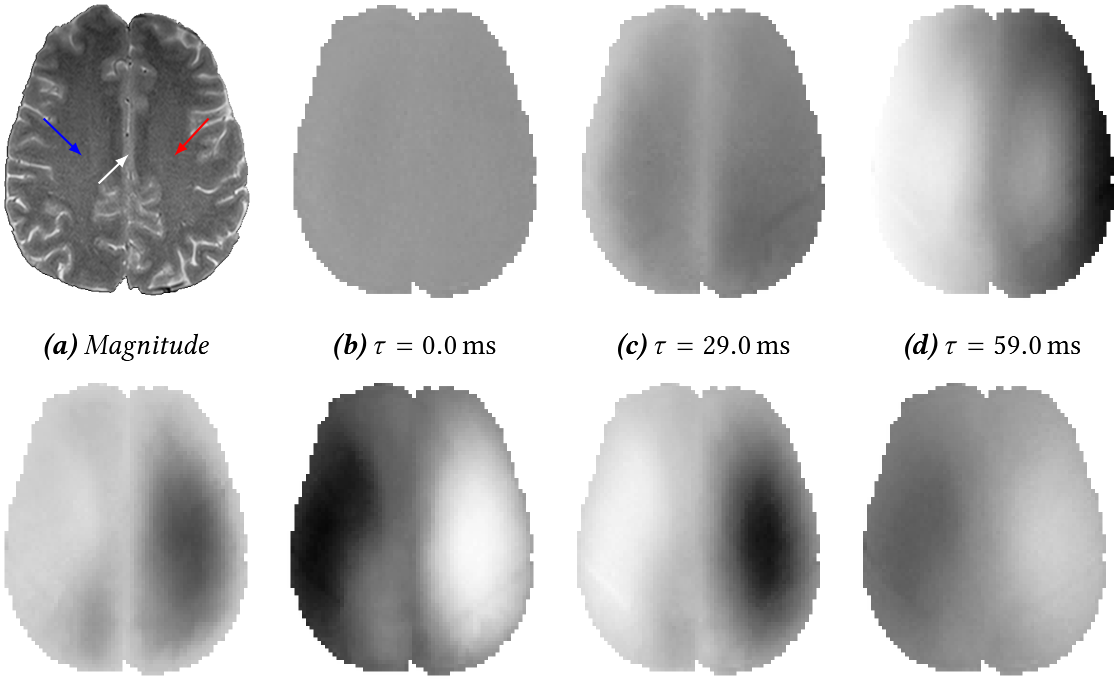
(a) *Magnitude* ***(b)*** $\tau = 0.0\,\mathrm{ms}$ ***(c)*** $\tau = 29.0\,\mathrm{ms}$ ***(d)*** $\tau = 59.0\,\mathrm{ms}$

(e) $\tau = 89.0\,\mathrm{ms}$ ***(f)*** $\tau = 120.0\,\mathrm{ms}$ ***(g)*** $\tau = 150.0\,\mathrm{ms}$ ***(h)*** $\tau = 180.0\,\mathrm{ms}$

Figure 4.16: *Exemplary phase images of the healthy volunteer:*
(a) shows a high-resolution image of the measured transverse slice. The arrows mark the location of pixels further analyzed with the relative phase $\Delta\phi_r$ *(cf. section 4.4.3). (b) to (h) show representative phase images at different values of* τ*. These images are averaged from five measurements and corrected by the baseline image. The gray scale is identical in all images.*
While the phase image at $\tau = 0\,\mathrm{ms}$ *only shows a homogeneous gray value, the images obtained at later times show an increasing contrast between the center and the border of each hemisphere. Up to* $\tau = 59\,\mathrm{ms}$ *the contrast is symmetric on both sides of the brain, later the motion clearly becomes asymmetric, as can be seen most prominently in (g).*

upwards.

4.4.2 Strain Images

The absolute phase strain images in figs. 4.17c and 4.17h show regions of higher strain in the anterior and posterior region and lower strain in the center region. The left hemisphere shows slightly larger values than the right one. Additionally, small areas of higher and lower strain are distributed almost equally over the measured slice. This pattern cannot be matched directly to the structures visible in the magnitude image (cf. fig. 4.17a). The integrated absolute phase strain depicted in fig. 4.17b again shows high values in the anterior and posterior parts and low values in the center of each hemisphere. The substructure shows several smaller features of high values that fit to the sulci visible in the magnitude image.

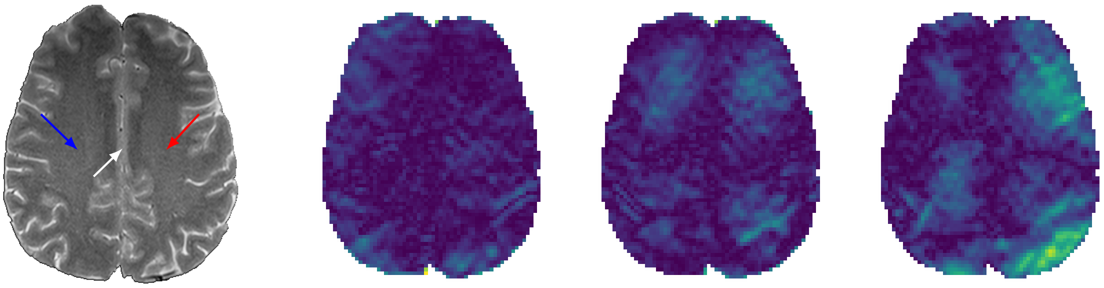

***(a)** Magnitude* ***(c)** $\tau = 29.0\,\mathrm{ms}$* ***(d)** $\tau = 59.0\,\mathrm{ms}$* ***(e)** $\tau = 89.0\,\mathrm{ms}$*

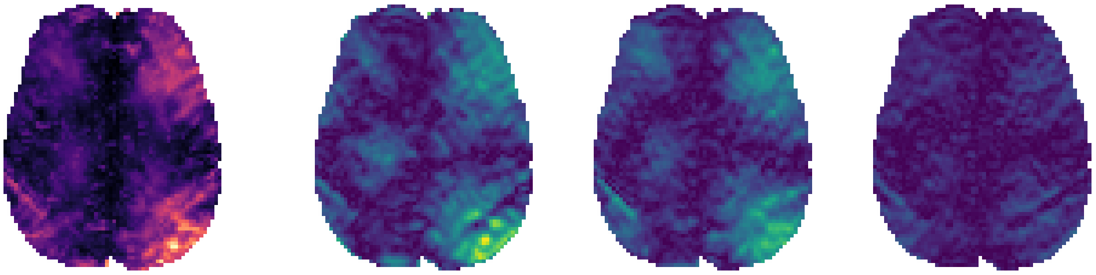

***(b)** $\epsilon_{\phi,\,\mathrm{total}}$* ***(f)** $\tau = 120.0\,\mathrm{ms}$* ***(g)** $\tau = 150.0\,\mathrm{ms}$* ***(h)** $\tau = 180.0\,\mathrm{ms}$*

***Figure 4.17:** Phase strain images of the healthy volunteer:*
Figure (a) shows again the high-resolution image of the measured transverse slice (fig. 4.16a). The arrows mark the location of pixels further analyzed with the relative phase $\Delta\phi_r$ (cf. section 4.4.3). Figures (c) to (h) show the absolute phase strain $|\epsilon_\phi|$ at the same values of τ as the phase images in fig. 4.16, except for $\tau = 0\,\mathrm{ms}$. This image is not shown, since it does not show any contrast. In all those images, the color scale is identical. Figure (b) shows the integrated absolute phase strain over all measured values of τ. In all phase strain images, darker colors represent lower strain, lighter colors represent higher strain.

4.4.3 Phase Progression

To further investigate the temporal behavior of the measured phase signal, the phase has been unwrapped in the temporal domain as described in section 3.2.

Figure 4.18 shows $\phi(\tau)$ for two single voxels, one in the center of the right and one in the center of the left hemisphere of the brain. The location of these voxels is indicated in figs. 4.16 and 4.17: the voxel in the right hemisphere is marked in blue, the one in the left hemisphere in red. The measurement of the phase turned out to be very accurate with standard errors as small as 0.02 rad. The mean standard error of all voxels over all measured values of τ was 0.15 rad.

Both graphs show a large initial peak and some smaller oscillations afterwards, that come to rest at approximately 350 ms. The asymmetry that was observed in the phase images is visible here as well when the two curves show a different progression from approximately $\tau = 80$ ms on. In the region with small $\Delta\tau$, the data scatters around the apparent progression stronger as the standard error, which might be an effect of the interleaved fashion of the different measurement series. A similar behavior was already observed in the measurement on phantom **I** (cf. fig. 4.15a).

The behavior of the phase is similar to what was expected from the simulated data in section 4.1.2. The initial peak can be explained by the downward motion of the movable shell (cf. fig. 4.3a). The smaller oscillation afterwards is likely governed by an oscillation of the tissue element (cf. fig. 4.3b), that is not visible on top of the large peak at small values of τ.

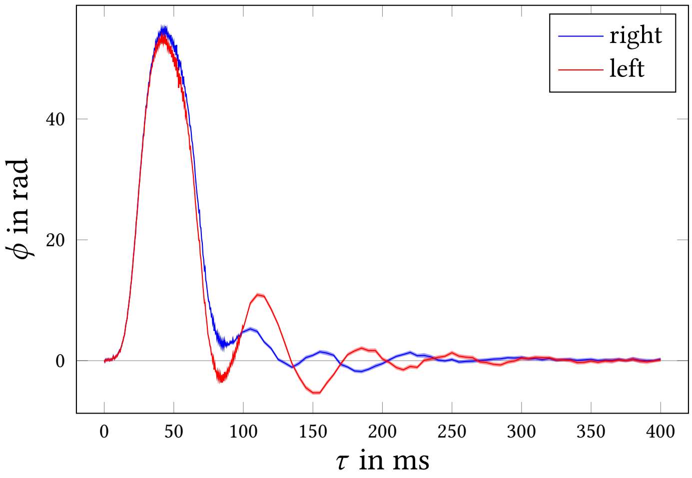

Figure 4.18: *Phase progression of single voxels of the healthy volunteer. The phase ϕ of two voxels in the center of each hemisphere of the healthy volunteer are plotted against τ. The standard error of the measurement is indicated by an errorband, but barely visible. Both graphs show a large initial peak that has its origin in the global falling motion of the head in the movable shell. Afterwards a smaller oscillation is visible. Here, the head does not experience a lot of motion, so that this part of the graph is governed by the oscillation of the corresponding volume elements relative to the cranial bone. The oscillation comes to a rest at approximately $\tau = 350$ ms.*

To be able to investigate the tissue response to the excitation without the superposed signal of the falling motion, the phase of the motion of the tissue elements relative to the cranial bone was desired. For this, the phase of every measured voxel relative to the phase of a reference voxel in the falx cerebri has been computed as described in section 3.2.3. The location of the pixel chosen as reference is indicated in figs. 4.16 and 4.17 by a white arrow.

Figure 4.19 shows the phase $\Delta\phi_r$ relative to the reference pixel for the same two voxels that have been shown in fig. 4.18. The oscillations of the two graphs start in phase shortly after $\tau = 0$ ms with an initial dip. At approximately $\tau = 70$ ms, the oscillations are both disturbed (most prominently in the right hemisphere). From here on, both graphs oscillate in phase opposition.

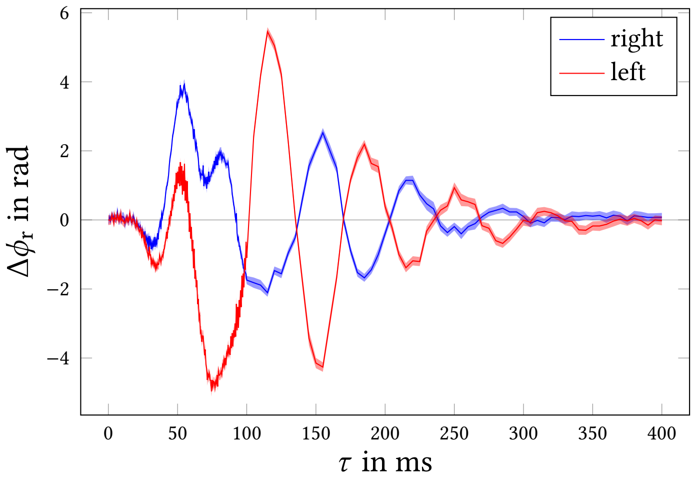

Figure 4.19: *Phase progression relative to a reference pixel: The phase $\Delta\phi_\mathrm{r}$ has been computed relative to the phase of the reference pixel in the falx cerebri. Again, the progression of the two voxels of the healthy volunteer (cf. fig. 4.18) is shown as a function of τ. The errorband indicates the standard error. Both volume elements show an oscillation starting in phase shortly after $\tau = 0$ ms. At about $\tau = 70$ ms this oscillation is disturbed and both volume elements continue to oscillate in phase opposition. Approximately 350 ms after the start of the falling motion the oscillation comes to rest.*

4.4.4 Deconvolution of the Phase Data

To examine the real deflection of the tissue that took place after the excitation, the relative phase $\Delta\phi_r$ of the two voxels elements needed to be deconvolved (cf. section 3.3). However, the variable sampling intervals used while measuring the phase (0.5 ms resp. 5.0 ms) proved to be incompatible with the algorithms developed: the least squared based algorithm (cf. section 3.3.3) needs evenly spaced samples per definition, and the derivative based algorithm failed at the transition between the two sampling rates. This was probably due to miscalculated derivatives in that region. Therefore, the relative phase data was interpolated by a smoothing spline representation of third order with the constraints of both a vanishing value and a vanishing derivative at $\tau = 0$ ms to comply with the assumptions made while developing the algorithms. Figure 4.20 shows the result of this interpolation for the two exemplary voxels in the two hemispheres. The spline representation was then used to create evenly sampled data points of the relative phase with a sample interval of $\Delta\tau = 1$ ms, which proved to be a value that yields reliable results in the simulations (cf. section 4.1.3).

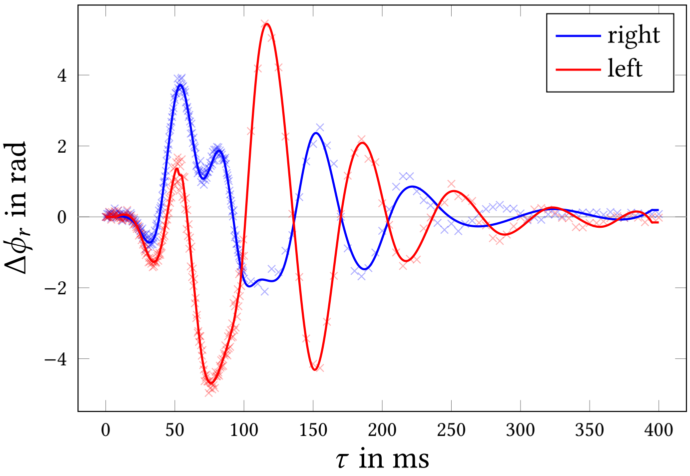

Figure 4.20: *Spline interpolation of the relative phase:*
The phase $\Delta\phi_r$ (light symbols) of the exemplary voxels in the left and right hemisphere has been interpolated by a smoothing spline (solid line). This spline interpolation has been used to create evenly spaced samples of the phase progression over the whole range of measured τ values. The splines fit the measured data well up to approximately $\tau = 200\,\text{ms}$, after that the spline deviates from the measurement due to the applied smoothing.

Figure 4.21 shows the results of the derivative based algorithm on that evenly sampled data. Both volume elements were initially deflected upwards and started oscillating. During the oscillation, the elements accumulated a shift in height relative to the reference point: the trajectory of the volume element in the right hemisphere leveled out approximately 20 µm lower than its original position, the volume element in the left hemisphere approximately 30 µm higher. In both reconstructed trajectories, the effect of noise begins to significantly distort the signal from roughly $\tau = 200\,\text{ms}$ on. This is expected: first, the underlying interpolating spline did not fit the measurement data in that region. Second, the numerical tests on the reconstruction algorithms showed already that measurement noise is amplified greatly during the deconvolution (cf. fig. 4.7). For that reason, the results of the least squared based algorithm (cf. section 3.3.3) are not shown: they initially show the same behavior, but significantly stronger noise amplification.

The apparent behavior of the two volume elements seems to be counter intuitive at first glance, since the relative phase (cf. fig. 4.19) seems to oscillate symmetrically around zero and vanishes at higher values of τ. However, in section 4.1.2 it was shown that a constant shift in the position of a volume element that is accumulated during the measurement sequence creates a peak in the phase signal, but not a constant shift in the phase (cf. fig. 4.3a). Therefore, the spatial shift experienced by the two volume elements is hard to observe in the relative phase, since it manifests there as a possibly small peak on top of the evident oscillation. The shift can possibly be explained by a rotation of the head along the longitudinal axis of the body (the z-axis in the DPCS).

4.4.5 Quality of the Interleaved Measurement

To investigate the small scattering of the data observed in fig. 4.18 and fig. 4.19, the phase values ϕ_i of the interleaved measurement series (cf. table 2.2) were evaluated individually. For that, the values $\phi_2(\tau, r, c)$ at half-integral values of τ that were measured with the second measurement series where interpolated linearly in the time domain and evaluated

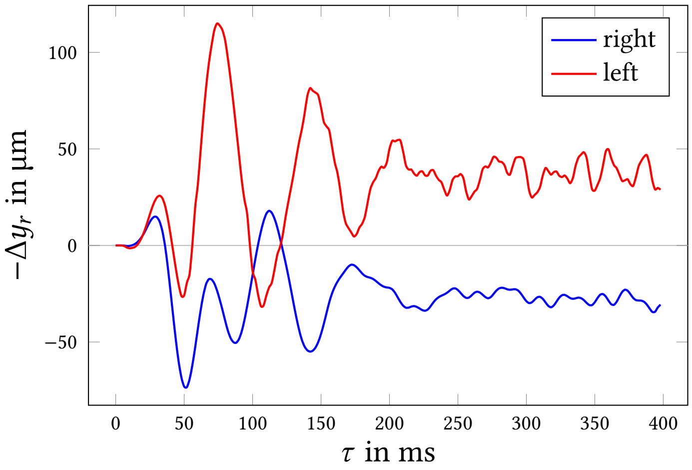

Figure 4.21: *Deconvolution of the relative phase:*
For better display, the negative value of the reconstructed relative deflection Δy_r is shown, i. e. a higher value represents a higher position. The evenly spaced samples of the relative phase created via the spline interpolation have been deconvolved using the derivative based algorithm. The volume elements both in the right and the left hemisphere initially deflected upwards and oscillated afterwards. During the oscillation, the volume elements accumulated a shift towards the reference point: The element in the right hemisphere comes to rest approximately 20 µm lower than it started, the element in the left hemisphere approximately 30 µm higher. This behavior might be explained by a rotation of the head during the falling motion, which would also translate into a height shift of the tissue with respect to the falx cerebri in the center of the measured slice. Both reconstructed positions show a strong influence of noise for later values of τ.

at integral values of τ. Then the difference of those interpolated values to the measured values $\phi_1(\tau, r, c)$ of the first measurement series was computed for every voxel inside the brain region $\mathcal{B}$ and averaged spatially:

$$\overline{\Delta\phi}(\tau) = \frac{1}{N} \sum_{(r,c)\in\mathcal{B}} \Big(\phi_1(\tau, r, c) - \phi_2(\tau, r, c)\Big), \tag{4.4}$$

with $N = 4022$ being the total amount of voxels in $\mathcal{B}$.

In a noise free scenario, $\overline{\Delta\phi}$ should be close to zero for all values of τ, except for the small errors introduced by the interpolation in the time domain. The measurement noise present here could possibly lead to deviations from that. In the case of a drift in the measured phase (cf. section 4.3.1), a constant value should be observed.

Figure 4.22 shows the computed values of $\overline{\Delta\phi}$. One can observe an initial peak with a maximum at approximately $\tau = 50$ ms and a succeeding dip with a minimum at approximately $\tau = 80$ ms. The differences of the third and fourth measurement series with τ values from 105 ms to 400 ms does not show a distinct structure. The time between the measurements compared here were approximately 30 min for the first and the second series and 10 min for the third and fourth series. If the effect is time dependent, this would therefore lead to a smaller effect for the higher values of τ.

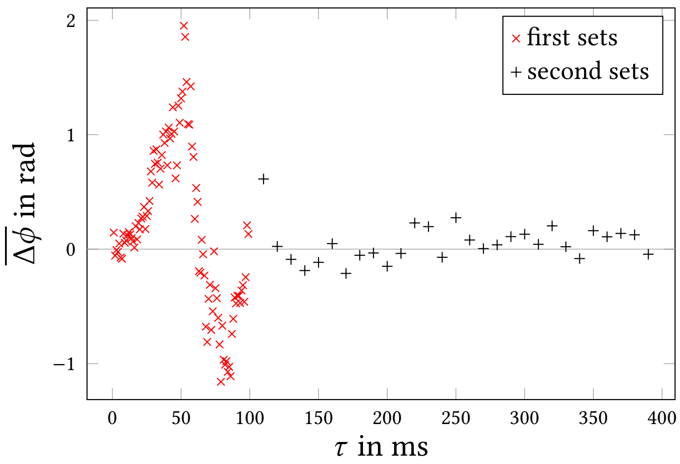

Figure 4.22: *Quality of the interleaved fashion of the measurement: The measured phase values of the second measurement series were interpolated to the values of* τ *of the first series and the difference was computed for every voxel. The plot shows the average difference* $\overline{\Delta\phi}(\tau)$ *of the voxels in the brain region as a function of* τ*. A constant drift of the reference phase should produce a constant value offside of zero in this plot. The peak and following dip in the first 100 ms suggest a change in the falling motion of the movable shell over time.*

The behavior at small τ could originate in a change of the shape of the falling motion of the movable shell over the course of the measurement. A lower falling height and a longer falling time would produce a smaller but broader initial peak in the measured phase. A second possible explanation is a slight shift of the start of the falling motion over time, resulting in a shift of the initial peak of the phase progression, which would also produce the observed behavior.

4.4.6 Analysis of the Falling Motion

To further investigate the results of the last section, the data of the OPMs was analyzed and the trajectory of the falling motion of the movable shell computed as described in section 3.1. To look for the possible changes in the falling motion of the movable shell over the measurement time, the change in height $y_s(\tau, t)$ at the location of the reference pixel in the center of the brain region has been computed from the OPM data at different value of τ.

The upper plot of fig. 4.23 shows the trajectories $y_s(\tau = 50\,\mathrm{ms}, t)$ and $y_s(\tau = 50.5\,\mathrm{ms}, t)$. The time scale has been chosen arbitrarily such that $t(\tilde{\tau} = 0) = 0$. To be able to compare these two trajectories, both have been shifted on the ordinate by the same value so that $y_s(\tau = 50\,\mathrm{ms}, 0) = 0$. Analogously, the center plot shows the trajectories $y_s(\tau = 200\,\mathrm{ms}, t)$ and $y_s(\tau = 205\,\mathrm{ms}, t)$. The errorbands indicate the standard deviation of the systematic error of the calculation that has been propagated from the errors on the location and the calibration of the OPMs.

Both plots show that the trajectory of the shell only changed very little over the time of the measurement: as explained above, due to the interleaved fashion of the measurement (cf. table 2.2), the two trajectories in the upper plot were acquired approximately 30 min after one another, while the two trajectories in the center plot were acquired approximately 9 min apart.

The lower plot in fig. 4.23 shows the difference $\Delta y_s(\tau = 50\,\mathrm{ms}, t) = y_s(\tau = 50\,\mathrm{ms}, t) -$

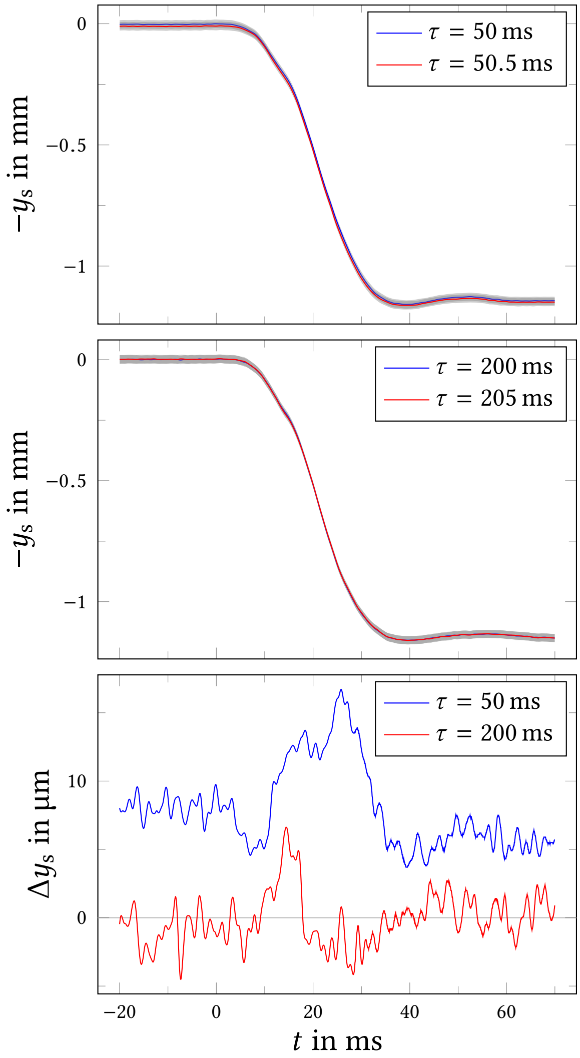

Figure 4.23: *Reconstructed trajectories of the movable shell.*

Shown are the shell height y_s reconstructed from the OPM data at different values of τ. The errorband indicates the systematic standard deviation of the reconstruction. For better display, the negative value of y_s is plotted, so that a higher value corresponds to a higher position. The upper and center plot each show two trajectories of successive values of τ that were measured in different measurement sequences due to the interleaved fashion of the measurement. The lower plot shows the difference of each of the two pairs of trajectories. Although the individual measurements were performed with large temporal delays of continuous measurements, there are only very small differences observable.

$y_\mathrm{s}(\tau = 50.5\,\mathrm{ms}, t)$ and the analogously calculated $\Delta y_\mathrm{s}(\tau = 200\,\mathrm{ms}, t)$. The deviations for the earlier value of τ are larger with a maximum value of approximately 17 µm. This plot also reveals that $\Delta y_\mathrm{s}(\tau = 50\,\mathrm{ms}, t) > 0$ for all times. This could either originate from a small shift of the movable shell (e. g. induced by motion of the patient) or indicate a small change in the photo voltage of the OPMs induced by a wobble of one of the fiber connectors or by a change of the light intensity of the LED.

To test whether these small differences in the falling motion could create the phase shift observed in the phase progression of the single voxels (cf. fig. 4.22), the $\Delta y_\mathrm{s}(t)$ were used to calculate the phase signal of these differences with eq. (2.2):

$$\begin{aligned} \phi(\Delta y_\mathrm{s}(\tau = 50\,\mathrm{ms})) &= 0.35\,\mathrm{rad} \\ \phi(\Delta y_\mathrm{s}(\tau = 200\,\mathrm{ms})) &= 0.03\,\mathrm{rad}. \end{aligned} \tag{4.5}$$

Especially for $\tau = 50\,\mathrm{ms}$ this value is too small to explain the phase differences $\overline{\Delta\phi}(\tau)$ (cf. fig. 4.22).

The OPM data was additionally used to calculate the orientation of the shell during the falling motion. Figure 4.24 shows the projection of the normal vector $\boldsymbol{n}$ of the calculated plane (cf. section 3.1.3) on the unit circle in the horizontal xz-plane of the DPCS, calculated from the azimuth and the inclination of $\boldsymbol{n}$. The plot reveals a rotation towards the foot of the patient (e. g. a nodding) and a slight rotation of the shell to the patient's right side. Although the shell is inclined by less than 0.1° in the left-right direction, this may account for a height shift of up to 0.1 mm over the width of a hemisphere with respect to the center of the brain. This result, therefore, confirms the interpretation of the relative deflection of the volume elements (fig. 4.21) and explains the left-right asymmetry observed in the phase images (fig. 4.16).

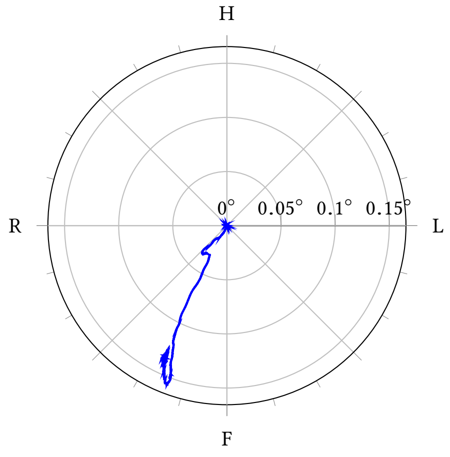

Figure 4.24: *Orientation of the movable shell during the falling motion.*
Plotted is the progression of the normal vector $\boldsymbol{n}$ *projected to the horizontal plane of the DPCS over the time of the falling motion at one specific value of* τ*. The result for other values of* τ *of the same measurement series are comparable. The radial axis depicts the inclination of the normal vector. The plot indicates a small rotation of the shell both along the longitudinal axis towards the volunteer's right side as well as one towards the foot of the volunteer, which corresponds to a nodding.*

4.5 Meningioma Patients

In order to test the capabilities of MRR to depict local alterations in the elastic properties of brain tissue in vivo, a study with four patients that were diagnosed with meningiomas

Patient ID	Sex	Age	Tumor location	Consistency
A	f	43	Right parietal convexity	Firm chondroitic consistency, with some softer areas similar to connective tissue
B	m	71	Right frontal convexity	Firm with some tougher calcification areas. Deeper tissue showed fluid retention
C	m	67	Left occipital	Soft, fat-like with only some areas of a more solid consistency comparable to muscle tissue
D	f	55	Right frontal falx	Comparable to muscle tissue with some even softer gelatinous areas

Table 4.1: *Overview of the meningioma patients:*
Listed are the patients' age and sex, the location of the meningioma and the neurosurgeons' interoperative assessment of the tumor consistency. [120]

was performed.

The MRR measurements have been conducted after all diagnostic scans took place and usually one day before the patients underwent surgery. During surgery, the consistency of the tumors was graded by the neurosurgeon. These assessments of the consistency and other relevant patient data are summarized in table 4.1. The experiments were conducted as described in section 2.2.2. All patients tolerated the measurement well, except for patient **B** who experienced slight discomfort, which is why the measurement was aborted after 28 min. Therefore, the time series for this patient only spans τ-values up to 69 ms. Due to a failure of the oscilloscope, the data of the OPMs was not stored for the measurement of patient **A**.

Figure 4.25 shows representative phase images of patient **A**. The meningioma, which is easily located in the high resolution magnitude image (cf. fig. 4.25a), is not visible in the phase image at $\tau = 0$ ms. In all successive images where significant motion took place during the motion encoding, the meningioma region becomes visible as a homogeneous area with different gray value than the surrounding healthy tissue. The contrast between those areas differs, and is strongest in figs. 4.25e and 4.25f ($\tau = 69$ ms and 105 ms). Apart from the tumor region, the overall contrast is comparable to the one observed in the healthy volunteer (cf. fig. 4.16). The images show significantly more smaller structures at the location of the sulci than it was observed in the healthy volunteer. All phase images additionally show a ghost artifact in form of a bent line in the posterior region of the measured slice.

Representative phase images of the patients **B** to **D** are presented in appendix A.3.1. They show qualitatively similar results, which is also illustrated in fig. 4.26b, showing phase images of all four meningioma patients at the time of the first maximum of $\Delta\phi_r$.

Figure 4.26c shows the calculated absolute phase strain $|\epsilon_\phi|$ for the same values of τas the phase images. In all four cases, the meningioma region shows up as a region with more homogeneous and overall lower strain. In patients **B** and **C** the boundary of the tumor is highlighted by a region of high strain. Especially in patient **A** the strain image also shows several of the sulci both in the outer region of the brain as well as near the

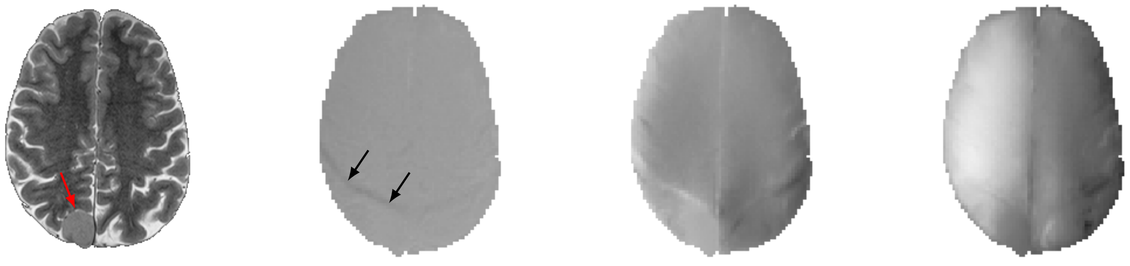

(a) *Magnitude* ***(b)*** $\tau = 0\,\mathrm{ms}$ ***(c)*** $\tau = 28.5\,\mathrm{ms}$ ***(d)*** $\tau = 52.5\,\mathrm{ms}$

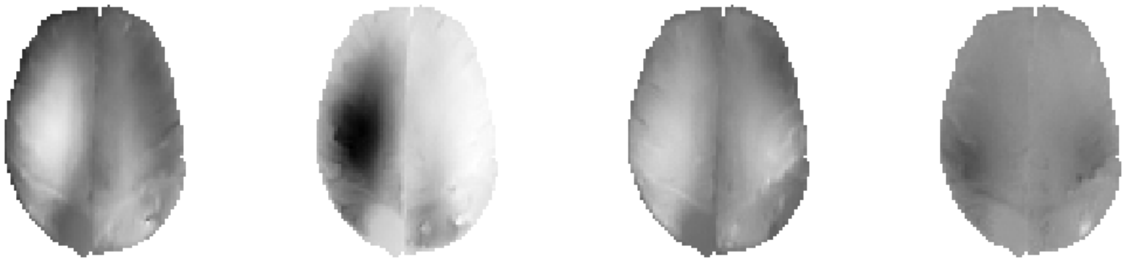

(e) $\tau = 69.0\,\mathrm{ms}$ ***(f)*** $\tau = 105.0\,\mathrm{ms}$ ***(g)*** $\tau = 130.0\,\mathrm{ms}$ ***(h)*** $\tau = 160.0\,\mathrm{ms}$

Figure 4.25: *Representative phase images of Meningioma patient **A**:*
(a) shows the high-resolution magnitude image. The meningioma is located at the right parietal convexity (red arrow). Figs. (c) to (h) show representative averaged phase images at different values of τ. The grayscale is identical in all those images. Similar to the results in fig. 4.16, the phase image at 0 ms shows no contrast except a line in the posterior region of the slice, that originates from a ghost in the image (black arrow). The meningioma is not visible in this image. However, in all phase images with higher values of τ, the meningioma becomes visible as a homogeneous region with varying clarity. [data published in 38].

falx cerebri.

The four meningiomas were sorted from solid to soft based on the surgeons' assessment of the tumor consistency. The tumor of **B** was identified as the most solid one, followed by the ones of the patients **A**, **D** and **C** in order of increasingly soft tissue consistency. The absolute phase strain values of the four meningiomas could not be compared directly due to the different excitations and the different location of the tumors in the cranial bone. The absolute phase strain was therefore normalized for each patient individually to the average value of the healthy region of the measured slice. This was done by manually outlining the tumor region based on the magnitude images. The average value of $|\epsilon_\phi|$ outside of the tumor region was then computed and the values inside the tumor region were normalized by that value. Figure 4.27 shows these normalized phase strain values as box plots compared to the tumor consistency. Although the spread of the values is large, a trend to higher strain values for softer tumors is visible. It should be noted that in this case the spread is not necessarily a measure for uncertainty, but mainly shows the heterogeneity of the tissue in the tumor region.

Figure 4.28 shows the total absolute phase strain $\epsilon_{\phi,\,\mathrm{total}}$ of the four meningioma patients (cf. section 3.2.4 and eq. (3.18)). Similar to the results of the healthy volunteer (cf. fig. 4.17),

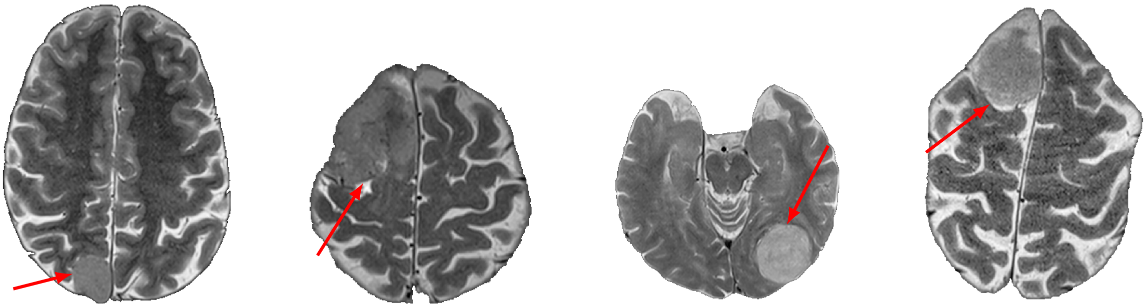

(a) *Magnitude images*

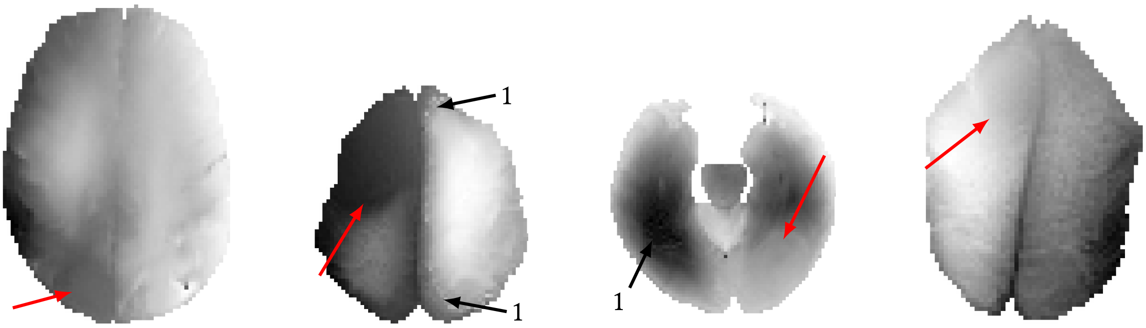

(b) *Phase images at the time of the maximum deflection*

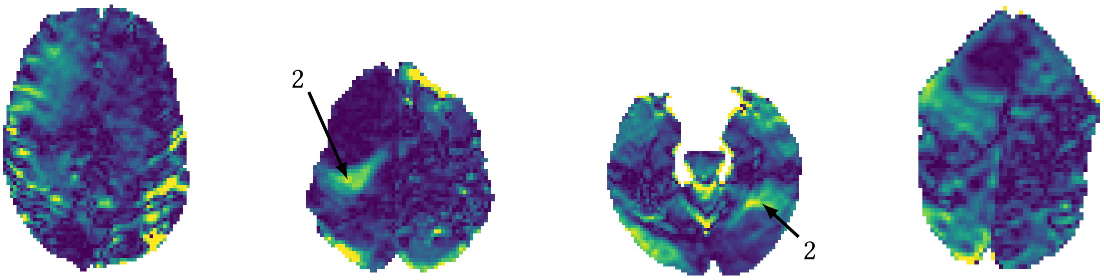

(c) *Absolute phase strain $|\epsilon_\phi|$ at the time of the maximum deflection*

Figure 4.26: *Comparison of the four meningioma patients.*
The meningioma patients ***A*** *to* ***D*** *are shown from left to right. Fig. (a) shows the high-resolution magnitude images of the measured slices. The meningiomas are marked with a red arrow. Fig. (b) shows a phase image of every patient at the time of the maximum deflection of the relative phase. Again, the meningiomas are marked with a red arrow. The phase images of patients* ***B*** *and* ***C*** *show phase unwrapping artifacts (marked with 1). The tumor regions show a signature in all images, although their visibility varies strongly: Patient* ***B*** *shows the highest visibility, while the meningioma of patient* ***D*** *is barely visible. Fig. (c) shows the absolute phase strain $|\epsilon_\phi|$ at the same values of τ as in the phase images. Here, all four meningiomas are visible as a region of smaller strain values. In patients* ***B*** *and* ***C*** *the region adjacent to the tumor is highlighted by high values of $|\epsilon_\phi|$ (marked with 2). [data published in 38].*

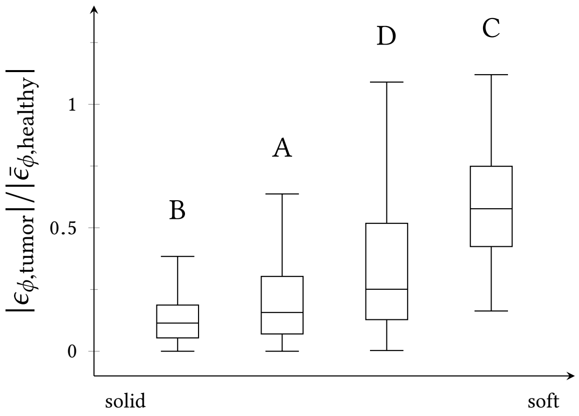

Figure 4.27: *Comparison of the meningioma stiffness.*

The absolute phase strain of the meningioma regions $|\epsilon_{\phi,\mathrm{tumor}}|$ was normalized to the average absolute phase strain in the corresponding healthy region $|\bar{\epsilon}_{\phi,\mathrm{healthy}}|$. This relative absolute phase strain of the meningiomas is shown as box plots sorted by the tumor consistency derived from the intraoperative palpation. The box plots' whiskers show values at 1.5 times the interquartile range below respectively above the first and third quartile. Outliers are not shown. Softer tumor tissue shows a trend towards higher values, as one would expect. [published in 38].

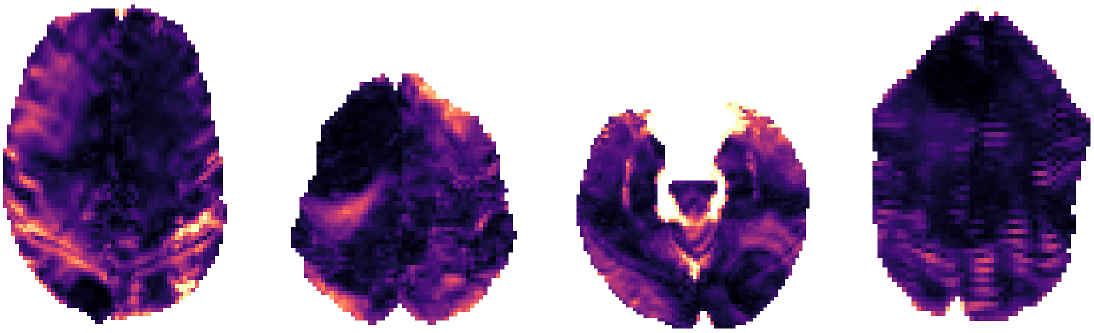

(a) *Patient* ***A*** ***(b)*** *Patient* ***B*** ***(c)*** *Patient* ***C*** ***(d)*** *Patient* ***D***

Figure 4.28: *Integrated absolute phase strain of the meningioma patients.*

Depicted is the absolute phase strain of the four patients integrated over the whole sampled interval. The scale of the images was adjusted individually. Darker colors represent low values, lighter colors represent high values.

the images for the patients **A** to **C** depict the structure of the sulci with much higher clarity than the single phase strain images, which is most apparent in patient **A** (fig. 4.28a). Consequently, the tumor boundaries, and in case of patient **C** the tumor heterogeneity, are well defined in these images. They match the borders identified in the magnitude images. The total phase strain image of patient **D** shows almost no contrast except for a large amount of short horizontal lines. These are most likely artifacts of the horizontal lines that are visible in the magnitude image and the phase images (cf. the corresponding images in figs. 4.26a and 4.26b). Those are intensified during the computation of $\epsilon_{\phi,\text{total}}$. In this case, the tumor region is almost not identifiable.

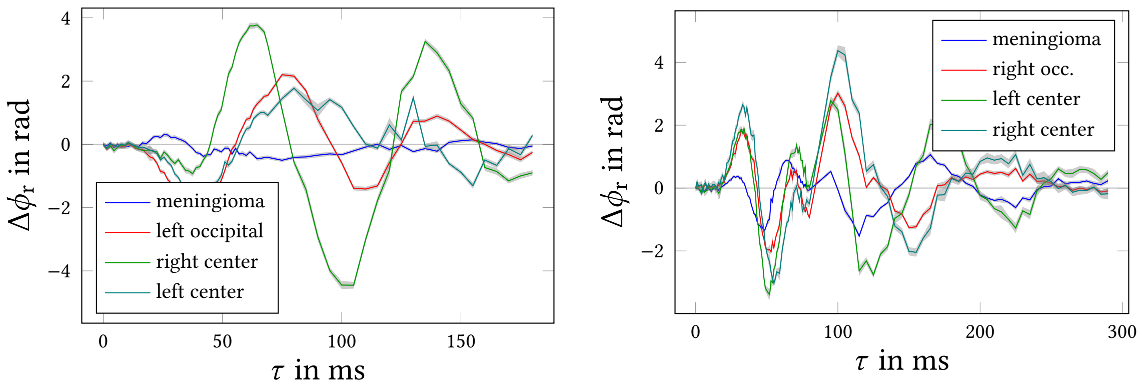

(a)** Patient **A

(b)** Patient **C

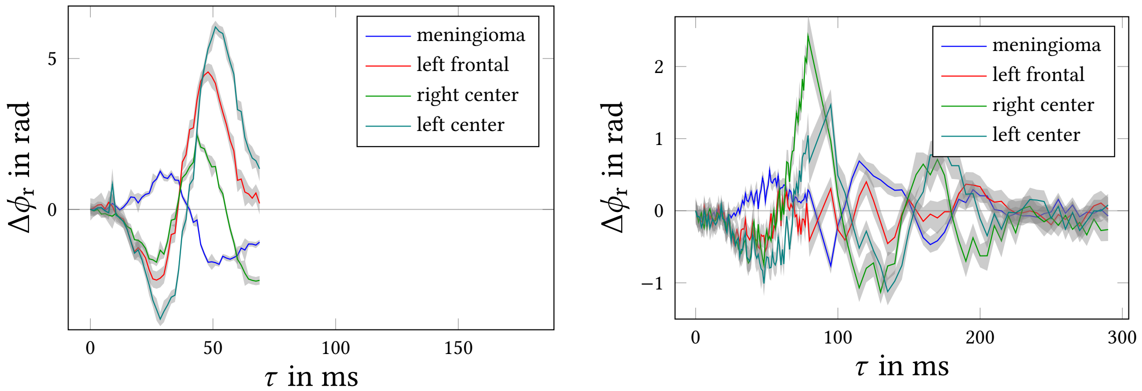

(c)** Patient **B

(d)** Patient **D

***Figure 4.29:** Relative phase progression of the meningioma patients.*
*The relative phase $\Delta\phi_r$ is plotted for four voxel: for each patient, one in the meningioma region (blue), one in the corresponding region of the healthy hemisphere (red) and two in the center of each hemisphere were chosen. In patients **A**, **B** and **C** the oscillation of the voxel in the meningioma region shows a reduced amplitude compared to the corresponding healthy region. The phase of patient **D** shows significantly more noise than the data of the other patients, most likely due to excessive motion of the patient.*

Figure 4.29 shows the phase $\Delta\phi_r$ of exemplary voxels with respect to a reference voxel in the falx cerebri for all four patients (cf. section 3.2.3). For every patient, a voxel in the meningioma region (blue), one at a similar location in the other hemisphere (red) and one in the center of each hemisphere was chosen. Most prominently in patient **A** but also in patient **B** the voxel in the meningioma region shows a reduced oscillation magnitude compared to the one at the corresponding region in the healthy hemisphere. In the patients **C** and **D** the oscillation in the meningioma region appears altered, too, but the magnitude is not reduce significantly. The uncertainty of the relative phase of patient **D** and the scattering of the data is noticeably higher than for the other patients and for the healthy volunteer (cf. fig. 4.19), which is attributed to excessive motion of the patient during the measurement.

5 Discussion and Conclusion

In this chapter, the previously described analysis methods and the presented results are discussed and put in a broader perspective.

First the quality and value of the phase images and of the phase progression is discussed, followed by a discussion of the experimental setup is. Last, the feasibility of MRR to depict mechanical properties space-resolved is discussed.

5.1 Phase Signal

In MRR the induced displacements of the tissue elements are encoded into the phase of the NMR signal and measured using the MRI system. The reconstructed phase images depicting this phase for every voxel in a single slice at a single value of τ are the basic data format provided by the MRR scanner. Numerical simulations have been used to predict the phase signal of single volume elements In the following, the quality and value of these images and the phase progression of the combined images are discussed.

5.1.1 Phase Images

The individual phase images of the phantom measurements (cf. figs. 4.11 and 4.13) match the hypothesis of a global oscillation as a response to the shock excitation (cf. section 2.1) with a higher deflection in the center than in the regions near the border. The baseline corrected images at $\tau = 0\,\mathrm{ms}$ showed no motion induced contrast. The motion pattern in both presented phantoms (cf. figs. 4.11 and 4.13) was similar to a higher mode of the vibration of a drum head. This indicates that some higher resonance frequencies did not experience high damping. The relatively high mobility of the phantom material in the container due to the sponge material at the container walls might play a role here, too.

The in vivo measurements both of the healthy volunteer and the patients revealed a similar oscillation in each hemisphere of the brain. Here, the overall motion pattern showed only the fundamental mode, which might indicate a higher damping constant of the brain tissue compared to the agar hydrogel used in the phantoms.

5.1.2 Phase Progression

To better understand the phase progression $\phi(\tau)$ (cf. section 3.2.2), numerical simulations were used to predict the phase signal the MEGs would produce for a single voxel. A constant shift in the position of a measured volume element similar to the falling motion used for the shock excitation produces a single peak in the phase $\phi(\tau)$ without a remaining constant offset. An oscillation of such a volume element on the other hand, as was hypothesized as the response to the excitation, again produces an oscillation of the phase (cf. section 4.1.2). This investigation also showed that the influence of the additional gradients that are present in the measurement sequence, namely the crusher gradients, is not negligible in general. In the investigated setup, the phase signal produced by those gradients was up to 15 % as strong as the one produced by the MEGs. It is worth noting that, since the crusher gradients are present in all spatial directions during the measurement, a potential motion perpendicular to the direction of the MEGs is therefore encoded into the measured signal with the same relative strength. These results explained the phase progressions of single voxels both in the phantom measurements and in vivo (cf. figs. 4.15 and 4.18).

To investigate the response of the volume elements to the excitation detached from the signal of the falling motion, the relative phase $\Delta\phi_r$ with respect to a reference point in the falx cerebri was calculated for the in vivo measurements (cf. figs. 4.16 and 4.29). The reference point was chosen because the falx cerebri should move little to none relative to the cranial bone. To which extent this assumption was justified could not be tested during this thesis, however.

To reduce the dependency of the measured phase signal on the form of the gradients of the MRI sequence, the trajectories of single voxels have been computed from the corresponding phase data. Three algorithms for this computation were developed of which two showed sufficient performance in tests with numerical data (cf. section 4.1.3). Although these tests also showed that these computations were sensitive to measurement noise, it was possible to use them to infer the trajectories of exemplary single voxels for the healthy volunteer after reducing the measurement noise of the measured signal (cf. fig. 4.21). However, the algorithms failed in deconvolving data with large changes in the sampling interval $\Delta\tau$, which is why the measured data had to be resampled. The calculated trajectories also revealed a rotation of the head of the healthy volunteer during the falling motion. They resulted in constant offsets in the location of volume elements next to the center of rotation. The fact that this offset was not observable in the relative phase is an indicator of the usefulness of the computation of the trajectories.

5.1.3 Phase Unwrapping and Quality of the Data

With the chosen settings of the MEGs, the range of the phase signal exceeded the range of 2π, which resulted in phase wraps that were removed using the algorithms described in section 1.5.2. Using the quality guided algorithm and the work flow described in section 3.2.1, this phase unwrapping process was sufficient for the cases presented here, as it was possible to automatically average and unwrap all images without any manual intervention. In some cases, the lines at which these wraps occurred were blurred in the column direction of the images, which resulted in the introduction of sometimes heavy artifacts by the phase unwrapping process (discussed in section 3.2.1). These artifacts could be reduced significantly by averaging phase images of identical measurements prior to the unwrapping (cf. fig. 3.6b), albeit without eliminating the smoothing effect in the original phase data. The blurring effect did only occur in some images (cf. figs. 4.11g, 4.11j and 4.26b).

The phase measurement of the MRI system proved to be very accurate despite the findings of Ulucay [40]: a measurement on a phantom without induced motion (cf. section 4.3.1) showed that the chosen measurement sequence lead to results with a standard deviation in the order of 10^{-2} rad in a single voxel. However, the measured phase showed a small drift over successive measurements that is currently unexplained. Even for in vivo experiments with induced motion, the phase measurements were still accurate with standard errors in the order of 10^{-1} rad (cf. fig. 4.18). Excessive motion of the patient lead to higher variabilities, as was most prominently observed with patient **D** (cf. fig. 4.29d). This was expected, however, since such motion influences the reproducibility of the induced falling motion.

5.1.4 Conclusion

The phase images provided a simple way of visually accessing the dynamics of the deflection inside the phantoms respectively the brain tissue. With only phase unwrapping, averaging and the baseline correction, there is no need for extensive post processing for these images. Investigating several phase images at different values of τ confirmed the hypothesized form of the volume elements' response to the excitation. The dynamics of the tissue response could be investigated further by means of the relative phase $\Delta\phi_r$ normalized to the phase of a reference point, which proved to be a reasonable approach.

Since the phase could be measured very precisely, future measurements might manage with less averages. Additionally, since it is unnecessary to sample the total phase progression but only the relative phase $\Delta\phi_r$ is needed to investigate the tissue response to the excitation, $\Delta\tau$ can be chosen much higher than in the measurements presented here. From the data of the healthy volunteer one can deduce that a sample spacing of $\Delta\tau \leq 4$ ms should be sufficient for the early part of the progression. The total measurement time was very high for the results presented in this thesis (≈80 min for the healthy volunteer). Using both approaches described above it might be possible to reduce this by a factor of more than ten (using one instead of five averages and a sample spacing of 4 ms for τ-values up to 100 ms).

Given the phase progression is sampled sufficiently in the temporal domain, it should be possible to unwrap the whole three-dimensional phase data set at once. In this case high quality regions at one value of τ might reduce artifacts in adjacent images, which might be especially beneficial with less averages (or even only a single image) per sampled value of τ. The problem of line artifacts in the unwrapped phase images at the location of the original phase wraps can in principle be avoided by choosing smaller MEGs and such avoid phase wraps altogether. However, this approach would not eliminate the apparent blurring of the original phase data. Furthermore, this would significantly lessen the sensitivity of the method. Therefore, future research should look into ways to reduce or eliminate the blurring.

The deconvolution approach to infer the actual deflection of volume elements developed in this thesis worked in principle, but was still sensitive to measurement noise. In its current implementation, it only operates on one-dimensional data so that it was only applied to the phase progression of selected voxels. In principle, an application to all measured volume elements is possible, though. The performance of the deconvolution could possibly be improved by choosing more suitable parameters for the MEGs. Choosing smaller values for Δ would produce less gaps in the Fourier spectrum of the gradient waveforms (cf. fig. 2.6), which might simplify the deconvolution. Choosing an altogether different shape of the MEGs with a flat Fourier spectrum up to a desired frequency would allow the use of the Fourier approach of the deconvolution (cf. section 3.3). A shape similar to the sine cardinal function might be adaptable here. Such an approach might alter the imaging contrast in the individual phase images, though.

To accurately calculate the deconvoluted deflection, the form of *all* gradients present in the MRI sequence needs to be known. In this thesis, only the parameters of the MEGs were extracted from the DICOM header, while the other gradients were assumed to be identical in every measurement. This assumption could not be tested, however. It would therefore be preferable to extract this data from the DICOM header as well.

5.2 Technical Realization

In this section the technical realization of the different parts of the MRR experiment are discussed, mostly the lifting device and its pneumatic control and the OPM.

All measurements presented in this thesis have been conducted using a setup that was the result of a series of prototypes developed our working group. These prototypes have been described extensively in [40]. The custom made lifting device and the pneumatic control create the desired motion of the head respectively the phantom with a high reproducibility.

After Ulucay described the setup, the post trigger was introduced into the measurement sequence that enabled the software based triggering of the motion (cf. sections 2.1.1.1 and 2.1.2.1). This greatly simplified the measurement process and lead to a semi-automatic sampling of the induced motion. Additionally extracting the measurement details from the DICOM header (cf. section 2.1.2.3) significantly simplified the post-processing of the phase data.

5.2.1 Lifting Device and Excitation

The construction of the lifting device was supposed to provide a stable upper position of the shell by means of the overpressure and determined by the flat headed screws (cf. section 2.1.1.1). The exact form of the falling motion should be controllable by adjusting the pressure and throttle valves. Björn Schemmann found in his diploma thesis that these control elements could not be adjusted independently from each other in a sufficient range. Moreover, the high pressure could not be adjusted in such a way that the upper position of the shell was determined only by the adjustment of the flat headed screws. As a consequence, both the orientation of the shell in the upper position and the trajectory of the falling motion were dependent on the distribution of weight on the shell. In contrast to the results of Ulucay [40], the detailed analysis of the OPMs unfortunately showed rotations of the shell in the transversal plane (cf. fig. 4.24 and appendix A.3.2). These may originate from a distortion of the shell itself, or, more likely, from the flat springs, whose stabilizing effect is not strong enough to effectively suppress such rotations, especially at the far end of the shell.

This rotation lead to a left-right asymmetry of the excitation of the tissue and with that also of the measured phase, which is visible in the phase images of all in vivo measurements and which was observed by Kofahl, too [98]. Also the calculated deflection of the healthy volunteer (fig. 4.21) clearly shows this asymmetry.

The interleaved fashion of the sampling of the phase progression additionally revealed a slow variation of the measured phase signal (cf. section 4.4.5). Such a variation might occur due to changes in the falling motion over the measurement time. However, the analysis of the falling motion of the shell could only in parts explain the observed effect (cf. fig. 4.23). The drift in the phase measurement (cf. section 4.3.1) might add to this effect as well: in the approximately 30 min between the two measurement sequences, the drift might accumulate a phase shift of more than 0.5 rad. However, this assumption can currently not be confirmed. It might well be possible, that there were alterations in the falling motion that were not depicted by the OPMs.

The measurement of the acceleration of the movable shell over the course of the falling motion under laboratory conditions (fig. 4.9) revealed several oscillations of the shell after the first landing on the vented rubber hoses. Since the excitation of the brain tissue in MRR is determined by this acceleration, this leads to a significantly more complex excitation profile than the one originally intended (cf. section 2.1). The observed accelerations were significantly smaller than the ones used by Bayly et al.: while the acceleration here was well below $1g$, Bayly reported peak accelerations of nearly $4g$ [39]. Peak acceleration is an important quantity regarding patient comfort.

5.2.2 Monitoring of the Shell Motion

The OPMs (section 2.1.1.2) have already been used by Ulucay [40] to qualitatively depict the motion of the movable shell. The optical signal is proportional to the height of the shell over a large range and provides a simple and fast way to monitor the shell motion in real time. This is an important property, since the OPMs were among other things used to tune the delay of the pneumatic control so that $\tau(\tilde{\tau} = 0) \leq 0\,\mathrm{ms}$ and to monitor the quality of the MRR measurement.

During this thesis, the OPM was also used to quantitatively measure the motion of the movable shell in order to look for rotations of the shell during the measurement. For that reason, the voltage of the photodiodes was calibrated by calipering the height of the shell in the upper and lower position (sections 2.1.1.2 and 3.1.1). This calibration was unsatisfactory for several reasons: Firstly, the connectors of the optical fibers did not close precisely enough. A motion of the optical fibers did therefore lead to a change in the measured signal. As a result the optical fibers had to be fixated prior to calibration, so that calibration had to take place inside the MRI scanner *after* the shell was loaded. In case of the in vivo measurements that meant calibration had to take place after the patient was positioned in the scanner, thereby significantly extending the time the patient had to spend in the scanner. Secondly, calibration by only two individual positions is prone to measurement errors. Under laboratory conditions, additional measurement points would lead to a higher precision. Thirdly, since the calipering was performed in the presence of the magnetic field of the MRI scanner, a non-magnetic sliding caliper with lower precision had to be used. All these reasons lead to a rather low precision of the calibration (fig. 3.2), that was propagated as a systematic uncertainty into all quantities depending on this data.

Additionally, the LEDs used for the OPM took over half an hour to reach a stable signal strength (fig. 4.8). Together with the calibration, this lead to a high amount of time needed to prepare a measurement.

To be able to infer the form of the falling motion at the location of the measured transversal slice, the location of the OPMs in the DPCS has to be known. For that reason, three markers were fixated at the movable shell and alignment scans were obtained to locate these markers in the DPCS (section 2.1.3). The semi-automatic locating of these markers in the scans and the determination of their location in the xz-plane of the DPCS (section 3.1.2 and fig. 3.3) was reliable and precise with standard deviations of 0.2 mm to 0.6 mm.

The transfer of these coordinates to the coordinates of the OPMs (section 3.1.2) was less precise due to the rather large uncertainties of the relative positions of the OPMs to the markers. As a result the standard deviations of the final location of the OPMs were in the range of 2 mm to 5 mm. While calculating the motion the movable shell performed during an MRR measurement (section 3.1.3), this led to a second systematic error next to the one of the calibration of the OPMs. Nevertheless, the calculated trajectory of the falling motion had a reasonably small uncertainty in the region of 10^{-2} mm (cf. fig. 4.23). Here, the location of the OPMs at the far end of the lifting device proofed to be beneficial since the above mentioned uncertainties did not propagate.

5.2.3 Conclusion

The practical application of the lifting device revealed that still some modifications are necessary to be able to produce reproducible acceleration profiles across measurements. Almost all pneumatic components need to be able to work in a wider working range to make sure the upper position of the shell is defined by the flat screws and not the weight distribution on the shell. To reduce the observed rotations along the body axis, the flat springs should either be adjusted or additional flat springs should be added at the superior end of the shell. The bouncing of the shell on the vented rubber hoses should be reduced to ensure no additional asymmetry is added and to simplify the acceleration profile. Preliminary work for the implementation of a damping material into the baseplate has been done by Roberto Correa Schragen in his bachelor thesis. Unfortunately, the actual implementation of this material into the prototype was not possible in time for the measurements presented here. Less oscillations might even help to reduce the phase unwrapping artifacts (section 3.2.1), if the hypothesis of its origin being motion during the read out parts of the sequence can be confirmed.

For a more precise calibration of the OPMs, different connectors for the optical fibers should be used whose transmission is less sensitive to motion of the fibers. This way, a precise calibration may be performed under laboratory conditions and reused several times. For the same reason, the system might benefit from the implementation of a measurement of the transmitted light relative to the maximum intensity to eliminate possible fluctuations in the light intensity emitted by the LEDs.

A higher precision of the location of the lifting device in the scanner's coordinate system could be achieved by a more precise measuring of the location of the marker on the shell. The marker itself worked reasonable well but might benefit from a different structure (like e.g. a cross shape) that makes it easier to determine their center.

A novel approach to create the desired motion of the head is been developed by Jakob Bindl, who uses a stepping motor instead of a pneumatic control to lift the head [121]. This approach might provide higher flexibility in choosing an excitation profile in the future.

5.3 Depiction of Mechanical Properties

The aim of MRR is the spatially resolved depiction of mechanical properties of brain tissue in vivo. In this section, the presented experimental results are therefore discussed regarding the potential of the novel method to depict local inhomogeneities in these properties.

5.3.1 Agar Hydrogel Phantoms

The measurements of the agar based phantoms confirmed the hypothesized global resonant oscillation of the volume elements of the material. The contrast in the phase images also clearly shows that the deflection pattern is influenced by the agar concentration of the agar hydrogel of the material since the different layers of both phantoms are distinguishable by eye (cf. fig. 4.11). Differences in the density of the agar hydrogel on the other hand only lead to comparatively small alterations of the deflection pattern, albeit the used difference of 20 % was much larger than what one would expect in brain tissue (cf. table 1.1). It is therefore unlikely that MRR will depict local inhomogeneities of the density of brain tissue in the current setup.

In both cases, the overall shape of the deflection pattern was similar in both layers of the phantom, which suggests that this shape is highly influenced by the geometry of the phantom and its boundary conditions. However, the phase images of phantom I (fig. 4.11) also suggest an influence of the agar concentration on the frequency of the oscillation of the volume elements. Both effects have been confirmed by Kofahl [38] in a systematic study on different agar phantoms.

In both phantoms, the deflection shows a complex pattern similar to a higher vibration mode of a drum sphere (cf. figs. 4.11 and 4.13). Therefore, areas of agar hydrogel with homogeneous properties do not appear homogeneous. In some cases this might lead to difficulties in the detection of smaller local alterations of these properties or in the confirmation of the absence of such alterations.

Due to the global oscillation of the material, the relative phase that encodes the deflection is not comparable directly over different locations in the measured volume. The aim of the phase strain images (cf. section 3.2.4) was to create a measure of the principle strain ϵ_{yy} that is less dependent on this total deflection pattern. However, the complex deflection pattern in the phantoms naturally translated into a highly complex pattern in the phase strain images as well (cf. figs. 4.12 and 4.14). In general, however, it was observed that the area with a lower agar concentration showed higher values of ϵ_ϕ, as one would expect. Matching the observations in the phase images, the area of higher density in phantom II showed slightly higher values of ϵ_ϕ, too. Again, this effect is much smaller than the one of the agar concentration.

In an attempt to compress the temporal information of the phase strain into a single image, its absolute value was integrated over the total measured interval of τ (cf. figs. 4.12b and 4.14b). Although there is no intuitive interpretation ready for this quantity, regions that experience higher strain over a significant amount of time should show higher values than areas that in general experience less strain. The results in both phantoms clearly reveal the mode shape of the oscillation. The lower regions of the hydrogel seem to experience more strain than the regions in the upper part of the phantoms and very low values near the left and right border of the phantom. This effect might be due to the fact that only the strain in one spatial direction was investigated, though. For both phantoms, these images provided the best way to distinguish the different layers of hydrogel with a sharp visible boundary and overall different values over the whole area of a homogeneous region.

5.3.2 In vivo Measurements

The general behavior of the agar hydrogel phantoms could be translated into the in vivo measurements, where each hemisphere of the brain individually showed a similar global oscillation (cf. figs. 4.16, 4.25 and 4.26b). In contrast to the results of the phantom measurements, though, the observed mode shape was only of fundamental or first order, which might serve as an indication that brain tissue is lossier than the agar hydrogel used as phantom material.

The images of the healthy volunteer (fig. 4.16) show almost no additional contrast. Intuitively, one would interpret this as a homogeneous tissue. However, the magnitude image clearly shows several fluid filled sulci that constitute local inhomogeneities of the mechanical properties. In the phase images of patient **A**, however, these sulci create a distinct contrast (cf. fig. 4.25). While a single phase image does not depict all of these sulci, images at different values of τ highlight different sulci. The phase images of the patients **B** and **C** also show signatures of sulci (cf. fig. 4.26b). In a study on ten healthy volunteers, Kofahl, too, observed that these small scale structures were depicted in some MRR measurements but not in all [98]. The reason for this behavior is currently unknown.

The absolute phase strain images of the healthy volunteer again confirm the basic mode shape of the oscillation of the two hemispheres, as it was the case for the phantoms. The posterior region shows slightly higher values than the anterior region, and, again similar to what was observed in the phantoms, the central region shows smaller values.

The advantage of the integrated absolute phase strain for a visual inspection is evident in this measurement as well: In this image, many sulci show a signature, although they were neither identifiable in the individual phase images nor in the individual phase strain images. These signatures match the location of the sulci in the magnitude image.

5.3.3 Meningiomas

With the four meningioma patients, four in vivo MRR measurements could be performed with known lesions that alter the mechanical properties of the tissue (cf. section 1.2.3.1). All these tumor regions showed a distinct signature of a homogeneous region with less deflection in the phase images (cf. figs. 4.25 and 4.26b). In the phase strain images (cf. fig. 4.26c) the meningiomas in general show smaller values than the healthy tissue. This behavior can be explained by the stiffer tissue of these tumors relative to the healthy brain tissue (cf. section 1.2.3.1), which was also confirmed by the neurosurgeons' assessment of the tumor consistency (cf. table 4.1).

Especially in the phase strain images, the borders of the meningiomas are well defined and match their extent in the magnitude images. The patients **B** and **C** shows areas of large values of $|\epsilon_\phi|$ in the healthy tissue next to the tumor region.

In an attempt to create a measure for the absolute phase strain that is comparable over the measurements of the different meningioma patients, the absolute phase strain in the meningioma region at the time of the first maximum of the deflection was normalized to the mean value of the healthy region of the measured slice and compared to the apparent stiffness based on the neurosurgeons' assessment (cf. fig. 4.27). The result agrees with the hypothesis that stiffer tissue experiences less strain. However, this result will not cover the complete underlying mechanical properties of the tissue, since it will still depend on on the overall geometry of the brain and the size of the tumor. Other studies on meningioma patients also reported an increased stiffness in the tumor tissue [27, 69]. If the spread of the values in the tumor regions is interpreted as heterogeneity, this estimate, too, agrees with the corresponding assessment by the neurosurgeons.

The integrated absolute phase strain images of the patients **A** to **C** (cf. figs. 4.28a–c) highlight the meningioma regions as areas with very low values and allow a clear evaluation of the boundaries of the meningiomas. The heterogeneity of the meningioma of patient **C** was depicted as well. A comparison of the meningioma stiffness based on these images is not feasible, though, since, apart from the limitations discussed for the individual phase strain images, the integrated value also depends on the length of the measured timeline and possibly the sample spacing. The integrated absolute phase strain of patient **D** is governed by what appears to be motion artifacts, that are enhanced by the computation of this value.

The mechanical properties of the meningioma tissue should also manifest in the progression of the relative phase (cf. fig. 4.29), which is evident in the results of the patients **A** and **B**. Here, the stiffer tissue shows a reduced oscillation amplitude as expected. For the softer meningiomas of the patients **C** and **D** this reduced amplitude is observable as well, however, the difference to a comparable volume element in the corresponding healthy region is very small.

5.3.4 Conclusion

The results presented in this thesis confirm the hypothesized influence of the mechanical properties of the tissue on the measured signals in MRR. Since the amount of measurements is small, though, this can only serve as a first proof of concept.

The deflection in the phantoms showed a complex mode shape, that showed various regions with low deflection that might limit the sensitivity of the method to local alterations in these areas. However, the global deflection pattern in the in vivo measurements were much simpler, so that various fluid filled sulci and all meningioma regions were visible both in the phase and the phase strain images. This possibility of MRR to depict local inhomogeneities in the mechanical properties was confirmed by Kofahl in measurements of phantoms with various inclusion [98].

Not all in vivo measurements depicted small features like the sulci, although most did. The reason for this sometimes lower spatial resolution is currently unknown, although an effect of a different excitation seems likely. Additional research is needed to discover, which excitation profiles lead to a desired contrast and to be able to reliably provide this excitation.

Currently, the discovery of lesions based on the mechanical properties in MRR measurements might be ambiguous, especially if the lesion is small, since at least some of the presented images show a complex contrast. This might be overcome by further measurements on healthy volunteers and a growing knowledge on the depiction of certain structures in MRR. The potential of MRR to depict small features may be used for qualitative diagnosis of the boundaries and properties of different lesions of the brain.

A quantitative analysis of the mechanical properties of the tissue was not possible during this thesis. In the future it might be desirable to infer mechanical parameters of the tissue, though. This would help in comparing measurements on different patients and would provide a way to detect and investigate diffuse neural diseases that alter the mechanical properties of the a large portion or the whole volume of the brain at once, as it was found for ageing [63], neurodegeneration [30, 122] and normal pressure hydrocephalus [75, 76] (cf. section 1.2.3).

As it was shown by the results in this thesis, it is feasible to measure the complete temporal evolution of the tissue deflection after the excitation, as well as the excitation profile itself, in physical units. In principle, this data contains all information about the mechanical properties of the system and can, therefore, be used to obtain quantitative values of these properties by using models of viscoelasticity. Such an approach would likely need three dimensional data encoding deflection in all three spatial dimensions, which would provide the full deflection field.

Summary

In this thesis the first application of Magnetic Resonance Rheology (MRR) to patients with known brain lesions was presented.

MRR is a novel approach to image the mechanical properties of brain tissue in vivo. It utilizes a short fall of the head of approximately 1 mm to create a global excitation of the brain tissue. The resulting deformations of the tissue are measured by means of Magnetic Resonance Imaging (MRI) and motion sensitive phase imaging techniques.

Numerical simulations were used to predict the signals MRR yields for volume elements following specific trajectories during the experiment. A post-procession pipeline was developed and implemented to analyze the measured phase data and to reconstruct the induced falling motion based on the optically measured position of the lifting device.

The influence of mechanical properties of the investigated material (stiffness and density) was presented on the basis of exemplary measurements on inhomogeneous phantoms. These consisted of two layers of different agar hydrogel manufactured with either different stiffness but similar density, or of similar stiffness but different density. The application of the method in vivo was shown by means of exemplary measurements on a healthy volunteer.

The measured data was analyzed by visual inspection of the resulting phase images depicting deflection of the material and of computed phase strain images depicting the principle strain in the direction of the falling motion. The dynamics of the material was further investigated using the temporal evolution of the phase over the progression of the falling motion.

The results confirmed a global oscillation of the material in response to the excitation. Particularly useful for visual inspection proved the temporal integration of the phase strain. Here, local differences in the mechanical properties of the phantom material respectively the brain tissue were depicted best.

The presented methods have been used in a study on four patients diagnosed with meningiomas, which are benign tumors originating from the meninges surrounding the brain. Manual palpation by the neurosurgeons that resected the tumors after the MRR measurements showed an increased stiffness of the tumor tissue compared to healthy tissue. The tumor regions showed well defined signatures in the obtained images. Comparing the strain in the tumor regions with the one in healthy parts of the corresponding brains showed a trend of lower strains with increased tumor stiffness.

These results can be considered a proof of concept of the feasibility of MRR to depict local alterations of the mechanical properties of brain tissue in vivo.

A Appendix

A.1 Phantom densities

In this section the measurement results of the densities of the phantom material is shown. All collected samples had a size of about $1 \times 1 \times 1\,\mathrm{cm}^3$. For every sample, the masses of the empty pycnometer m_0, the pycnometer filled with distilled water m_1, the pycnometer with the dissected sample m_2 and the pycnometer with sample filled up with distilled water m_3 where measured. The density was calculated after equation (2.6). The measurement error on the masses was assumed to be $\Delta m = 0.005\,\mathrm{g}$, which should include inaccuracies due to air bubbles or left over pollutions on the outside of the pycnometer. The masses m_0 and m_1 were averaged over all samples of one phantom before the calculation to provide a better estimate.

Sample	m_0 [g]	m_1 [g]	m_2 [g]	m_3 [g]	ρ [g/cm^3]
1	43.503	146.022	46.048	146.031	1.004(7)
2	43.802	146.014	46.703	146.025	1.001(7)
3	43.805	146.021	46.942	146.026	1.001(7)
4	43.783	146.013	46.685	146.032	1.003(7)

(a) *Measurement results*

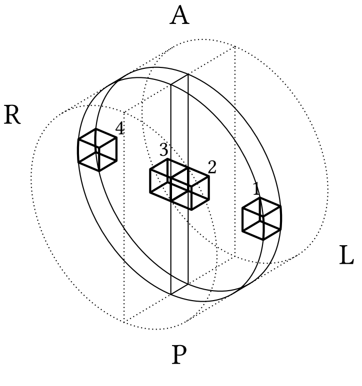

(b) *Location of the samples.*

Table A.1: *Density measurements of Phantom I.*
(a) shows the results of the pycnometer measurements of the individual samples. (b) shows the location of the samples in the phantom oriented in the Dicom Patient Coordinate System (DPCS) as it was in the scanner. The water used for the density measurements had a temperature of $T_{\mathrm{H_2O}} = 19.0(2)\,^\circ\mathrm{C}$ *and with that a density of* $\rho_{\mathrm{H_2O}} = 0.9984(1)\,\mathrm{g/cm^3}$.

Sample	m_0 [g]	m_1 [g]	m_2 [g]	m_3 [g]	ρ [g/cm^3]
1	43.500	145.987	48.093	146.783	1.214(14)
2	43.660	145.982	47.672	146.624	1.185(12)
3	43.611	145.981	47.428	145.975	0.996(6)
4	43.591	145.978	47.134	145.973	0.996(6)
5	43.601	145.982	46.134	146.442	1.219(14)
6	43.587	145.984	46.284	146.418	1.191(13)

***(a)** Measurement results*

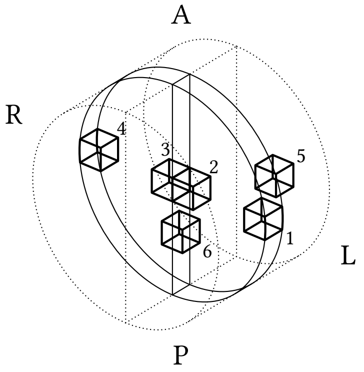

***(b)** Location of the samples.*

***Table A.2:** Density measurements of Phantom II.*
The results of the pycnometer measurements of the individual samples are shown in (a). The location of the samples is shown in (b), that shows the phantom oriented in the DPCS as it was in the scanner. The hydrogel on the patient's left side (samples 1, 2, 5 and 6) was cooked with added tungsten carbide to increase the density. The used water had a temperature of $T_{H_2O} = 20.0(5)\,°\mathrm{C}$ *and with that a density of* $\rho_{H_2O} = 0.9982(2)\,\mathrm{g/cm^3}$.

A.2 Siemens CSA header fields

Quantity	Unit	Field in CSA header	Description
Δt_{90}	[ms]	`sWiPMemBlock.adFree[9]`	Start of the first motion encoding gradient after the maximum of the 90° pulse
δ	[ms]	`sWiPMemBlock.adFree[7]`	Length of the MEG
$\delta\Delta$	[ms]	`sWiPMemBlock.adFree[8]`	Time between both MEG. This value equals to $\Delta - \delta$
G	[mT/m]	`sWiPMemBlock.adFree[12]`	Maximum gradient strength of the MEG
$\tilde{\tau}$	[ms]	`sWiPMemBlock.alFree[6]`	Post trigger fill time
$\Delta\tau$	[ms]	`sWiPMemBlock.alFree[20]`	PTFT Decrement
N_τ	[ ]	`sWiPMemBlock.alFree[21]`	PTFT Averages

***Table A.3:** Quantities describing the form and position of the motion encoding gradients of the spin echo (SE)-echo planar imaging (EPI) sequence "nin_ep2d_diff_vb10r" and the respective fields in the private CSA header of the DICOM files they are stored in.*

A.3 Additional experimental results

A.3.1 Representative phase images of the meningioma patients

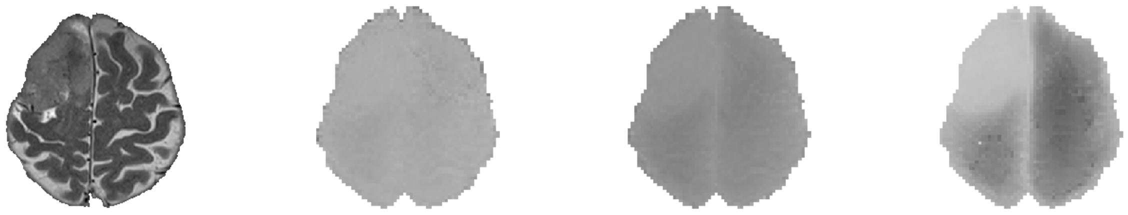

(a) *Magnitude* ***(b)*** $\tau = 0\,\mathrm{ms}$ ***(c)*** $\tau = 12.0\,\mathrm{ms}$ ***(d)*** $\tau = 24.0\,\mathrm{ms}$

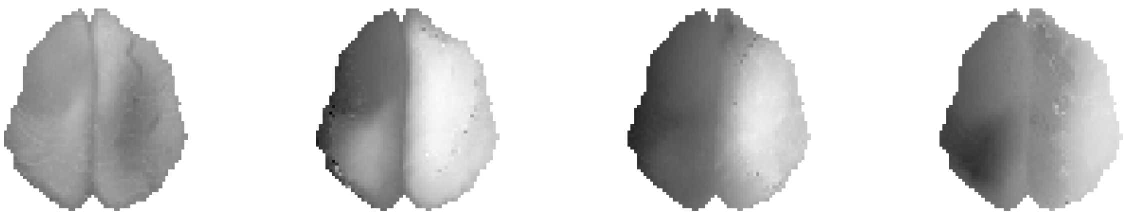

(e) $\tau = 37.5\,\mathrm{ms}$ ***(f)*** $\tau = 48.0\,\mathrm{ms}$ ***(g)*** $\tau = 58.5\,\mathrm{ms}$ ***(h)*** $\tau = 69.0\,\mathrm{ms}$

Figure A.1: *Representative phase images of Meningioma patient* ***B****:*
(a) shows the high-resolution magnitude image. The meningioma is located at the right frontal convexity. Figs. (c) to (h) show representative averaged phase images at different values of τ. *The grayscale is identical in all those images. The phase images of this patient show a large amount of phase unwrapping artifacts.*

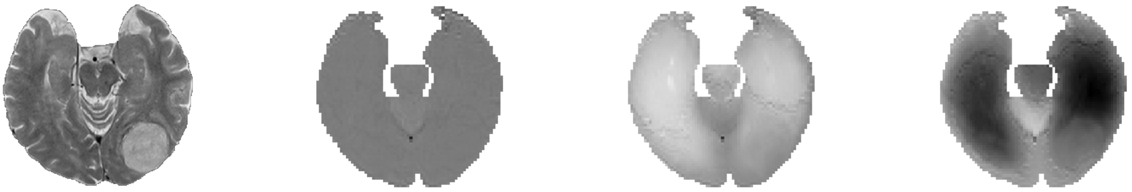

(a) *Magnitude* ***(b)*** $\tau = 0\,\mathrm{ms}$ ***(c)*** $\tau = 28.0\,\mathrm{ms}$ ***(d)*** $\tau = 52.0\,\mathrm{ms}$

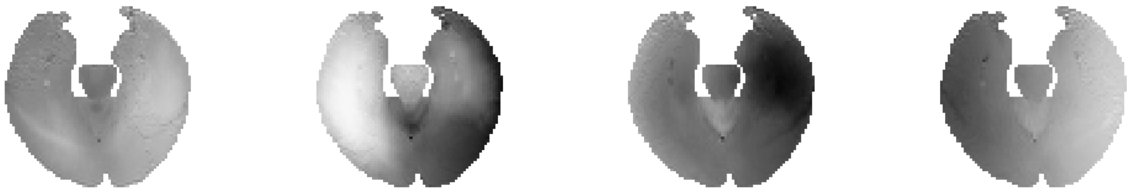

(e) $\tau = 69.0\,\mathrm{ms}$ ***(f)*** $\tau = 105.0\,\mathrm{ms}$ ***(g)*** $\tau = 130.0\,\mathrm{ms}$ ***(h)*** $\tau = 160.0\,\mathrm{ms}$

Figure A.2: *Representative phase images of Meningioma patient* ***C****:*
(a) shows the high-resolution magnitude image. The meningioma is located left occipital. Figs. (c) to (h) show representative averaged phase images at different values of τ. *The grayscale is identical in all those images.*

(a) *Magnitude* ***(b)*** $\tau = 0\,\mathrm{ms}$ ***(c)*** $\tau = 28.0\,\mathrm{ms}$ ***(d)*** $\tau = 52.0\,\mathrm{ms}$

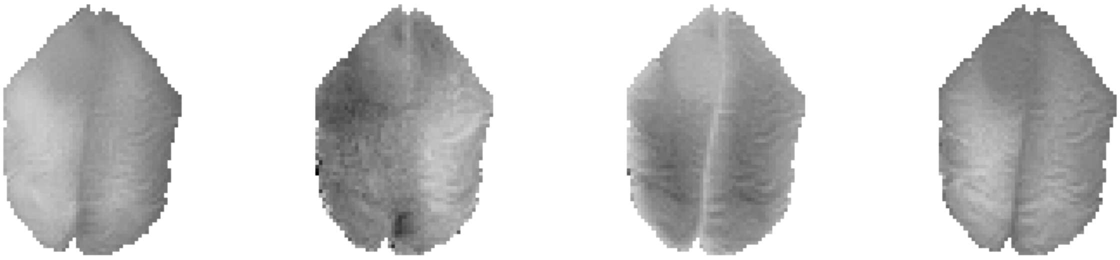

(e) $\tau = 69.0\,\mathrm{ms}$ ***(f)*** $\tau = 105.0\,\mathrm{ms}$ ***(g)*** $\tau = 130.0\,\mathrm{ms}$ ***(h)*** $\tau = 160.0\,\mathrm{ms}$

Figure A.3: *Representative phase images of Meningioma patient* ***D****:*
(a) shows the high-resolution magnitude image. The meningioma is located at the right frontal falx. Figs. (c) to (h) show representative averaged phase images at different values of τ*. The grayscale is identical in all those images.*

A.3.2 Orientation plots of the meningioma patients

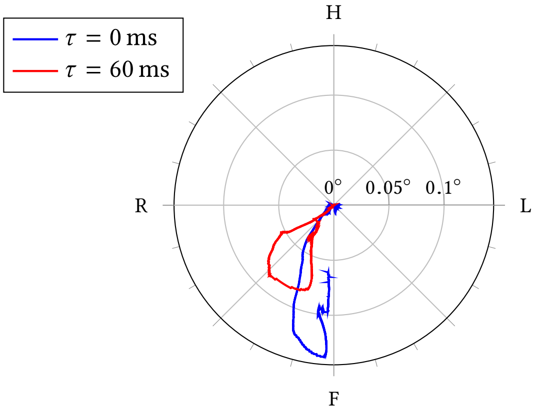

Figure A.4: *Orientation of the movable shell during the measurement of patient* ***B****. Plotted is the progression of the normal vector* $\boldsymbol{n}$ *projected to the horizontal plane of the DPCS over the time of the falling motion. The radial axis depicts the inclination of the normal vector. The results varied for this measurement, therefore the progression is shown for two values of* τ *outlining this variability.*

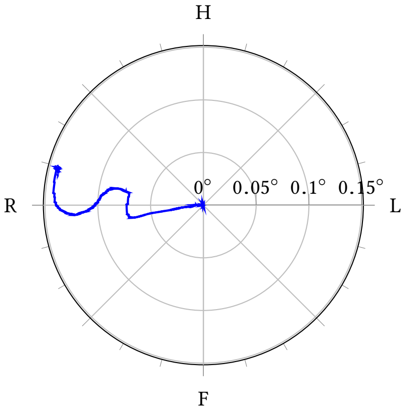

Figure A.5: *Orientation of the movable shell during the measurement of patient **C**. Plotted is the progression of the normal vector **n** projected to the horizontal plane of the DPCS over the time fo the falling motion at one specific value of τ. The results for other values of τ were comparable. The radial axis depicts the inclination of the normal vector. This plot indicates a rotation of the shell along the longitudinal axis towards the patient's right side.*

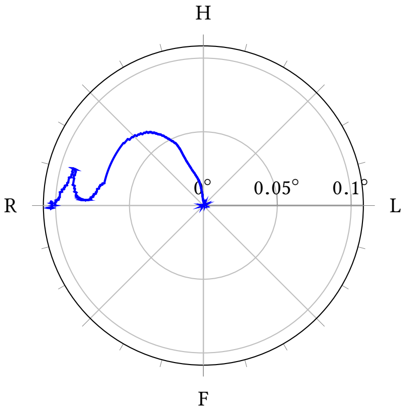

Figure A.6: *Orientation of the movable shell during the measurement of patient **D**. Plotted is the progression of the normal vector **n** projected to the horizontal plane of the DPCS over the time fo the falling motion at one specific value of τ. The results for other values of τ were comparable. The radial axis depicts the inclination of the normal vector. This plot indicates a rotation of the shell along the longitudinal axis towards the patient's right side.*

Bibliography

[1] D. Berger. "A brief history of medical diagnosis and the birth of the clinical laboratory. Part 1–Ancient times through the 19th century". In: *MLO: medical laboratory observer* 31.7 (1999), 28–30, 32, 34–40. ISSN: 0580-7247 (cit. on p. 1).

[2] Wells, Peter N. T. and Hai-Dong Liang. "Medical ultrasound: imaging of soft tissue strain and elasticity". In: *Journal of the Royal Society, Interface* 8.64 (2011), 1521–1549. ISSN: 1742-5662 (cit. on p. 1).

[3] S. Webb. *The physics of medical imaging.* 2nd ed. Bristol: Institute of Physics, 2001. ISBN: 978-0-7503-0573-0 (cit. on pp. 1, 15, 18, 50).

[4] Hans L. Oestreicher. "Field and Impedance of an Oscillating Sphere in a Viscoelastic Medium with an Application to Biophysics". In: *The Journal of the Acoustical Society of America* 23.6 (1951), 707–714. ISSN: 0001-4966 (cit. on p. 1).

[5] Henning E. von Gierke et al. "Physics of Vibrations in Living Tissues". In: *Journal of Applied Physiology* 4.12 (1952), 886–900. ISSN: 8750-7587 (cit. on p. 1).

[6] R. J. Dickinson and C. R. Hill. "Measurement of soft tissue motion using correlation between A-scans". In: *Ultrasound in Medicine & Biology* 8.3 (1982), 263–271. ISSN: 03015629 (cit. on p. 1).

[7] L. Wilson. "Ultrasonic measurement of small displacements and deformations of tissue". In: *Ultrasonic Imaging* 4.1 (1982), 71–82. ISSN: 01617346 (cit. on p. 1).

[8] T. A. Krouskop, D. R. Dougherty, and F. S. Vinson. "A pulsed Doppler ultrasonic system for making noninvasive measurements of the mechanical properties of soft tissue". In: *Journal of rehabilitation research and development* 24.2 (1987), 1–8. ISSN: 0748-7711 (cit. on p. 1).

[9] R. M. Lerner et al. "Sono-Elasticity: Medical Elasticity Images Derived from Ultrasound Signals in Mechanically Vibrated Targets". In: *Acoustical Imaging: Proceedings of the Sixteenth International Symposium, June 10–12, 1987.* Ed. by L. W. Kessler. Vol. 16. Boston and MA: Springer US, 1988, 317–327. ISBN: 978-1-4613-0725-9 (cit. on p. 1).

[10] J. Ophir. "Elastography: A quantitative method for imaging the elasticity of biological tissues". In: *Ultrasonic Imaging* 13.2 (1991), 111–134. ISSN: 01617346 (cit. on p. 1).

[11] Armen P. Sarvazyan et al. "Shear wave elasticity imaging: a new ultrasonic technology of medical diagnostics". In: *Ultrasound in Medicine & Biology* 24.9 (1998), 1419–1435. ISSN: 03015629 (cit. on p. 1).

[12] Stefan Catheline, François Wu, and Mathias Fink. “A solution to diffraction biases in sonoelasticity: The acoustic impulse technique”. In: *The Journal of the Acoustical Society of America* 105.5 (1999), 2941–2950. ISSN: 0001-4966 (cit. on p. 1).

[13] J. Bercoff, M. Tanter, and M. Fink. “Supersonic shear imaging: a new technique for soft tissue elasticity mapping”. In: *IEEE Transactions on Ultrasonics, Ferroelectrics and Frequency Control* 51.4 (2004), 396–409. ISSN: 0885-3010 (cit. on p. 1).

[14] Kathryn R. Nightingale et al. “On the feasibility of remote palpation using acoustic radiation force”. In: *The Journal of the Acoustical Society of America* 110.1 (2001), 625–634. ISSN: 0001-4966 (cit. on p. 1).

[15] J. B. Fowlkes et al. “Magnetic-resonance imaging techniques for detection of elasticity variation”. In: *Medical physics* 22.11 Pt 1 (1995), 1771–1778. ISSN: 0094-2405 (cit. on p. 1).

[16] Elias A. Zerhouni et al. “Human heart: tagging with MR imaging–a method for noninvasive assessment of myocardial motion”. In: *Radiology* 169.1 (1988), 59–63. ISSN: 0033-8419 (cit. on p. 1).

[17] L. Axel and L. Dougherty. “Heart wall motion: improved method of spatial modulation of magnetization for MR imaging”. In: *Radiology* 172.2 (1989), 349–350. ISSN: 0033-8419 (cit. on p. 1).

[18] R. Muthupillai et al. “Magnetic resonance elastography by direct visualization of propagating acoustic strain waves”. In: *Science* 269.5232 (1995), 1854–1857. ISSN: 0036-8075 (cit. on pp. 1, 12).

[19] Raja Muthupillai et al. “Magnetic resonance imaging of transverse acoustic strain waves”. In: *Magnetic Resonance in Medicine* 36.2 (1996), 266–274. ISSN: 07403194 (cit. on p. 1).

[20] Nathan McDannold and Stephan E. Maier. “Magnetic resonance acoustic radiation force imaging”. In: *Medical physics* 35.8 (2008), 3748–3758. ISSN: 0094-2405 (cit. on p. 1).

[21] Marcus Radicke et al. “New image contrast method in magnetic resonance imaging via ultrasound”. In: *HFI/NQI 2007*. Ed. by A. Pasquevich et al. Berlin, Heidelberg: Springer Berlin Heidelberg, 2008, 541–546. ISBN: 978-3-540-85319-0 (cit. on p. 1).

[22] Jessica Mende et al. “Acoustic radiation force contrast in MRI: detection of calcifications in tissue-mimicking phantoms”. In: *Medical physics* 37.12 (2010), 6347–6356. ISSN: 0094-2405 (cit. on pp. 1, 37).

[23] M. Radicke et al. “Acoustic radiation contrast in MR images for breast cancer diagnostics–initial phantom study”. In: *Ultrasound in Medicine & Biology* 37.2 (2011), 253–261. ISSN: 03015629 (cit. on p. 1).

[24] K. J. Parker, M. M. Doyley, and D. J. Rubens. “Imaging the elastic properties of tissue: the 20 year perspective”. In: *Physics in medicine and biology* 56.1 (2011), R1–R29. ISSN: 1361-6560 (cit. on p. 1).

[25] Yogesh K. Mariappan, Kevin J. Glaser, and Richard L. Ehman. “Magnetic resonance elastography: a review”. In: *Clinical anatomy (New York, N.Y.)* 23.5 (2010), 497–511. ISSN: 1098-2353 (cit. on pp. 1, 12).

[26] Paul J. McCracken et al. “Mechanical transient-based magnetic resonance elastography”. In: *Magnetic resonance in medicine* 53.3 (2005), 628–639. ISSN: 0740-3194 (cit. on pp. 2, 13).

[27] M. Simon et al. “Non-invasive characterization of intracranial tumors by magnetic resonance elastography”. In: *New Journal of Physics* 15.8 (2013), 085024. ISSN: 1367-2630 (cit. on pp. 2, 13, 99).

[28] Matthew C. Murphy et al. “Preoperative assessment of meningioma stiffness using magnetic resonance elastography”. In: *Journal of neurosurgery* 118.3 (2013), 643–648. ISSN: 1933-0693. (Visited on 01/10/2015) (cit. on pp. 2, 13).

[29] Jens Wuerfel et al. “MR-elastography reveals degradation of tissue integrity in multiple sclerosis”. In: *NeuroImage* 49.3 (2010), 2520–2525. ISSN: 1095-9572 (cit. on pp. 2, 14).

[30] Matthew C. Murphy et al. “Decreased brain stiffness in Alzheimer’s disease determined by magnetic resonance elastography”. In: *Journal of magnetic resonance imaging : JMRI* 34.3 (2011), 494–498. ISSN: 1053-1807 (cit. on pp. 2, 14, 100).

[31] Kevin J. Glaser, Armando Manduca, and Richard L. Ehman. “Review of MR elastography applications and recent developments”. In: *Journal of magnetic resonance imaging : JMRI* 36.4 (2012), 757–774. ISSN: 1053-1807 (cit. on pp. 2, 12 sq.).

[32] Simon Chatelin, André Constantinesco, and Rémy Willinger. “Fifty years of brain tissue mechanical testing: from in vitro to in vivo investigations”. In: *Biorheology* 47.5-6 (2010), 255–276. ISSN: 1878-5034 (cit. on pp. 2, 12 sq.).

[33] M. M. Doyley. “Model-based elastography: a survey of approaches to the inverse elasticity problem”. In: *Physics in medicine and biology* 57.3 (2012), R35–73. ISSN: 1361-6560 (cit. on p. 2).

[34] John B. Weaver et al. “Brain mechanical property measurement using MRE with intrinsic activation”. In: *Physics in medicine and biology* 57.22 (2012), 7275–7287. ISSN: 1361-6560 (cit. on pp. 2, 13).

[35] L. Xu et al. “Magnetic resonance elastography of the human brain: a preliminary study”. In: *Acta radiologica (Stockholm, Sweden : 1987)* 48.1 (2007), 112–115. ISSN: 0284-1851 (cit. on p. 2).

[36] Sebastian Theilenberg et al. “Magnetic Resonance Rheology of the human brain”. In: *Proceedings of the International Society for Magnetic Resonance in Medicine.* 2014, 1690 (cit. on pp. 2, 29).

[37] Anna-Lisa Kofahl et al. “MR-Rheology - a feasibility study with phantoms”. In: *Proceedings of the International Society for Magnetic Resonance in Medicine.* 2014, 1689 (cit. on pp. 2, 29).

[38] Anna-Lisa Kofahl et al. "Combining rheology and MRI: Imaging healthy and tumorous brains based on mechanical properties". In: *Magnetic resonance in medicine* (2016), n/a–n/a. ISSN: 0740-3194 (cit. on pp. 2 sq., 69, 85 sqq., 97).

[39] P. V. Bayly et al. "Deformation of the human brain induced by mild acceleration". In: *Journal of neurotrauma* 22.8 (2005), 845–856. ISSN: 0897-7151 (cit. on pp. 2, 95).

[40] Deniz Ulucay. „Rheologie im Kopf". PhD thesis. Bonn: Rheinische Friedrich-Wilhelms-Universität Bonn, 2015 (cit. on pp. 2, 29–32, 68 sq., 93 sqq.).

[41] M. Reiner. "The Deborah Number". In: *Physics Today* 17.1 (1964), 62. ISSN: 00319228 (cit. on p. 5).

[42] Christopher W. Macosko. *Rheology: Principles, measurements, and applications.* Advances in interfacial engineering series. New York: VCH, 1994. ISBN: 1-56081-579-5 (cit. on pp. 5, 9).

[43] Hanswalter Giesekus. *Phänomenologische Rheologie: Eine Einführung.* Berlin and New York: Springer-Verlag, 1994. ISBN: 3-540-57513-8 (cit. on pp. 5–9).

[44] Manfred Pahl, Wolfgang Gleißle, and Hans-Martin Laun. *Praktische Rheologie der Kunststoffe und Elastomere.* Kunststofftechnik. Düsseldorf: VDI-Verlag, 1991. ISBN: 9783182341550 (cit. on p. 5).

[45] M. Mooney. "A Theory of Large Elastic Deformation". In: *Journal of Applied Physics* 11.9 (1940), 582–592. ISSN: 0021-8979 (cit. on p. 10).

[46] R. W. Ogden. "Large Deformation Isotropic Elasticity - On the Correlation of Theory and Experiment for Incompressible Rubberlike Solids". In: *Proceedings of the Royal Society A: Mathematical, Physical and Engineering Sciences* 326.1567 (1972), 565–584. ISSN: 1364-5021 (cit. on p. 10).

[47] Richard L. Drake, Wayne Vogl, and Mitchell, Adam W. M. *Gray's Anatomie für Studenten.* 1. Aufl. München [u.a.]: Elsevier, Urban & Fischer, 2007. ISBN: 978-3-437-41231-8 (cit. on p. 10).

[48] Maria Antoniou Patestas and Leslie P. Gartner. *A textbook of neuroanatomy.* Malden, MA: Blackwell Pub., 2006. ISBN: 978-1-4051-0340-4 (cit. on pp. 10 sq.).

[49] Martin Trepel. *Neuroanatomie: Struktur und Funktion : [mit dem Plus im Web - Zugangscode im Buch].* 5. Aufl. München: Urban & Fischer in Elsevier, 2012. ISBN: 978-3-437-41299-8 (cit. on pp. 10 sq.).

[50] Henry Gray and Warren H. Lewis. *Anatomy of the human body.* 20th ed. Philadelphia: Lea & Febiger, 1918. ISBN: 1-58734-102-6 (cit. on pp. 10 sq.).

[51] Karol Miller. *Biomechanics of the brain.* Biological and medical physics, biomedical engineering. New York: Springer, 2011. ISBN: 978-1-4419-9996-2 (cit. on pp. 11 sq.).

[52] R. H. Pudenz and C. H. Shelden. "The lucite calvarium; a method for direct observation of the brain; cranial trauma and brain movement". In: *Journal of neurosurgery* 3.6 (1946), 487–505. ISSN: 1933-0693 (cit. on p. 12).

[53] Ayub K. Ommaya. “Mechanical properties of tissues of the nervous system”. In: *Journal of biomechanics* 1.2 (1968), 127–138. ISSN: 1873-2380 (cit. on p. 12).

[54] G. T. Fallenstein, V. D. Hulce, and J. W. Melvin. “Dynamic mechanical properties of human brain tissue”. In: *Journal of biomechanics* 2.3 (1969), 217–226. ISSN: 1873-2380 (cit. on p. 12).

[55] James E. Galford and James H. McElhaney. “A viscoelastic study of scalp, brain, and dura”. In: *Journal of biomechanics* 3.2 (1970), 211–221. ISSN: 1873-2380 (cit. on p. 12).

[56] Shaokoon Cheng, Elizabeth C. Clarke, and Lynne E. Bilston. “Rheological properties of the tissues of the central nervous system: a review”. In: *Medical engineering & physics* 30.10 (2008), 1318–1337. ISSN: 1350-4533 (cit. on p. 12).

[57] G. Franceschini et al. “Brain tissue deforms similarly to filled elastomers and follows consolidation theory”. In: *Journal of the Mechanics and Physics of Solids* 54.12 (2006), 2592–2620. ISSN: 00225096 (cit. on p. 12).

[58] T. W.E.D. Barber, Judith A. Brockway, and Lawrence S. Higgins. “THE DENSITY OF TISSUES IN AND ABOUT THE HEAD”. In: *Acta Neurologica Scandinavica* 46.1 (1970), 85–92. ISSN: 00016314 (cit. on p. 12).

[59] Howard Metz, James McElhaney, and Ayub K. Ommaya. “A comparison of the elasticity of live, dead, and fixed brain tissue”. In: *Journal of biomechanics* 3.4 (1970), 453–458. ISSN: 1873-2380 (cit. on p. 12).

[60] Jürgen Braun et al. “Simulation and analysis of magnetic resonance elastography wave images using coupled harmonic oscillators and Gaussian local frequency estimation”. In: *Magnetic Resonance Imaging* 19.5 (2001), 703–713. ISSN: 0730725X (cit. on p. 13).

[61] Michael A. Green, Lynne E. Bilston, and Ralph Sinkus. “In vivo brain viscoelastic properties measured by magnetic resonance elastography”. In: *NMR in biomedicine* 21.7 (2008), 755–764. ISSN: 1099-1492 (cit. on p. 13).

[62] Jürgen Braun et al. “High-resolution mechanical imaging of the human brain by three-dimensional multifrequency magnetic resonance elastography at 7T”. In: *NeuroImage* 90 (2014), 308–314. ISSN: 1095-9572 (cit. on p. 13).

[63] Ingolf Sack et al. “The impact of aging and gender on brain viscoelasticity”. In: *NeuroImage* 46.3 (2009), 652–657. ISSN: 1095-9572 (cit. on pp. 13, 100).

[64] Daniel Gallichan et al. “TREMR: Table-resonance elastography with MR”. In: *Magnetic resonance in medicine* 62.3 (2009), 815–821. ISSN: 0740-3194 (cit. on p. 13).

[65] Lucy V. Hiscox et al. “Magnetic resonance elastography (MRE) of the human brain: technique, findings and clinical applications”. In: *Physics in medicine and biology* 61.24 (2016), R401–R437. ISSN: 1361-6560 (cit. on p. 13).

[66] L. Xu et al. “Magnetic resonance elastography of brain tumors: preliminary results”. In: *Acta radiologica (Stockholm, Sweden : 1987)* 48.3 (2007), 327–330. ISSN: 0284-1851 (cit. on p. 13).

[67] David N. Louis et al. “The 2007 WHO classification of tumours of the central nervous system”. In: *Acta neuropathologica* 114.2 (2007), 97–109. ISSN: 0001-6322 (cit. on p. 13).

[68] Peter Berlit. *Klinische Neurologie.* 3., erweiterte und vollständig überarbeitete Auflage. Berlin, Heidelberg: Springer Berlin Heidelberg, 2012. ISBN: 978-3-642-16919-9 (cit. on pp. 13 sq.).

[69] M. Reiss-Zimmermann et al. “High Resolution Imaging of Viscoelastic Properties of Intracranial Tumours by Multi-Frequency Magnetic Resonance Elastography”. In: *Clinical neuroradiology* 25.4 (2015), 371–378. ISSN: 1869-1447 (cit. on pp. 13, 99).

[70] Joshua D. Hughes et al. “Higher-Resolution Magnetic Resonance Elastography in Meningiomas to Determine Intratumoral Consistency”. In: *Neurosurgery* 77.4 (2015), 653–8, 653–8. ISSN: 1524-4040 (cit. on p. 13).

[71] R. Alroughani et al. “Predictors of Conversion to Multiple Sclerosis in Patients with Clinical Isolated Syndrome Using the 2010 Revised McDonald Criteria”. In: *ISRN neurology* 2012 (2012), 792192. ISSN: 2090-5513 (cit. on p. 14).

[72] Kaspar-Josche Streitberger et al. “Brain viscoelasticity alteration in chronic-progressive multiple sclerosis”. In: *PloS one* 7.1 (2012), e29888. ISSN: 1932-6203 (cit. on p. 14).

[73] Andreas Fehlner et al. “Higher-resolution MR elastography reveals early mechanical signatures of neuroinflammation in patients with clinically isolated syndrome”. In: *Journal of magnetic resonance imaging : JMRI* 44.1 (2016), 51–58. ISSN: 1053-1807 (cit. on p. 14).

[74] Matthew C. Murphy et al. “Regional brain stiffness changes across the Alzheimer’s disease spectrum”. In: *NeuroImage. Clinical* 10 (2016), 283–290 (cit. on p. 14).

[75] Kaspar-Josche Streitberger et al. “In vivo viscoelastic properties of the brain in normal pressure hydrocephalus”. In: *NMR in biomedicine* 24.4 (2011), 385–392. ISSN: 1099-1492 (cit. on pp. 14, 100).

[76] Florian Baptist Freimann et al. “Alteration of brain viscoelasticity after shunt treatment in normal pressure hydrocephalus”. In: *Neuroradiology* 54.3 (2012), 189–196. ISSN: 1432-1920 (cit. on pp. 14, 100).

[77] N. Fattahi et al. “MR Elastography Demonstrates Increased Brain Stiffness in Normal Pressure Hydrocephalus”. In: *AJNR. American journal of neuroradiology* 37.3 (2016), 462–467. ISSN: 1936-959X (cit. on p. 14).

[78] I. I. Rabi et al. “A New Method of Measuring Nuclear Magnetic Moment”. In: *Physical Review* 53.4 (1938), 318. ISSN: 0031-899X (cit. on p. 14).

[79] E. M. Purcell, H. C. Torrey, and R. V. Pound. “Resonance Absorption by Nuclear Magnetic Moments in a Solid”. In: *Physical Review* 69.1-2 (1946), 37–38. ISSN: 0031-899X (cit. on p. 14).

[80] F. Bloch, W. W. Hansen, and Martin Packard. “Nuclear Induction”. In: *Physical Review* 69.3-4 (1946), 127. ISSN: 0031-899X (cit. on p. 14).

[81] P. C. Lauterbur. “Image Formation by Induced Local Interactions: Examples Employing Nuclear Magnetic Resonance”. In: *Nature* 242.5394 (1973), 190–191. ISSN: 0028-0836 (cit. on p. 14).

[82] P. Mansfield and P. K. Grannell. “NMR ’diffraction’ in solids?” In: *Journal of Physics C: Solid State Physics* 6.22 (1973), L422–L426. ISSN: 0022-3719 (cit. on p. 14).

[83] Maximilian Reiser, ed. *Magnetresonanztomographie: Mit 253 Tabellen.* Berlin [u.a.]: Springer, 1992. ISBN: 3-540-51004-4 (cit. on pp. 15, 18).

[84] F. Bloch. “Nuclear Induction”. In: *Physical Review* 70.7-8 (1946), 460–474. ISSN: 0031-899X (cit. on p. 17).

[85] Dominik Weishaupt, Victor D. Köchli, and Borut Marincek. *Wie funktioniert MRI? Eine Einführung in Physik und Funktionsweise der Magnetresonanzbildgebung.* 7th ed. Berlin, Heidelberg: Springer, 2014. ISBN: 3642416160 (cit. on p. 18).

[86] E. L. Hahn. “Spin Echoes”. In: *Physical Review* 80.4 (1950), 580–594. ISSN: 0031-899X (cit. on p. 19).

[87] Matt A. Bernstein, Kevin Franklin King, and Xiaohong Joe Zhou. *Handbook of MRI pulse sequences.* Amsterdam and Boston: Academic Press, 2004. ISBN: 978-0-12-092861-3 (cit. on pp. 21, 34).

[88] National Electrical Manufacturers Association. *Digital Imaging and Communications in Medicine (DICOM) Standard* (cit. on pp. 22, 24).

[89] Jolinda Smith. *IKT: Create 3D image data by a series of 2D dicom files.* 2003. URL: `https://itk.org/pipermail/insight-users/2003-September/004762.html` (visited on 09/20/2016) (cit. on p. 24).

[90] Dennis C. Ghiglia and Mark D. Pritt. *Two-dimensional phase unwrapping: Theory, algorithms, and software.* New York: Wiley, 1998. ISBN: 0471249351 (cit. on pp. 24 sq., 27).

[91] Kazuyoshi Itoh. “Analysis of the phase unwrapping algorithm”. In: *Applied optics* 21.14 (1982), 2470. ISSN: 0003-6935 (cit. on p. 25).

[92] Richard M. Goldstein, Howard A. Zebker, and Charles L. Werner. “Satellite radar interferometry: Two-dimensional phase unwrapping”. In: *Radio Science* 23.4 (1988), 713–720. ISSN: 00486604 (cit. on p. 25).

[93] J. M. Huntley. “Noise-immune phase unwrapping algorithm”. In: *Applied optics* 28.16 (1989), 3268–3270. ISSN: 0003-6935 (cit. on p. 26).

[94] T. J. Flynn. “Consistent 2-D phase unwrapping guided by a quality map”. In: *Proceedings of the 1996 International Geoscience and Remote Sensing Symposium.* Vol. 4. 1996, 2057–2059 (cit. on p. 26).

[95] Anil K. Jain. *Fundamentals of digital image processing.* Prentice-Hall information and system sciences series. Englewood Cliffs, NJ: Prentice Hall, 1989. ISBN: 9780133325782 (cit. on p. 26).

[96] M. W. Roth. “Phase Unwrapping for Interferometric SAR by the Least-Error Path”. In: *Johns Hopkins University Applied Physics Lab Technical Report, Laurel, Md* 30 (1995) (cit. on p. 27).

[97] M. D. Pritt. “Phase unwrapping by means of multigrid techniques for interferometric SAR”. In: *IEEE Transactions on Geoscience and Remote Sensing* 34.3 (1996), 728–738. ISSN: 01962892 (cit. on p. 27).

[98] Anna-Lisa Kofahl. “Magnetic Resonance Rheology on Phantoms and Human Brains: to be published”. PhD thesis. Bonn: Rheinische Friedrich-Wilhelms-Universität Bonn, 2017 (cit. on pp. 30, 38, 69, 95, 98, 100).

[99] Jürgen Finsterbusch. *Motion sensitive SE_EPI sequence "nin_ep2d_diff_vb10r"*. 2015-03-31 (cit. on p. 33).

[100] E. O. Stejskal and J. E. Tanner. “Spin Diffusion Measurements: Spin Echoes in the Presence of a Time-Dependent Field Gradient”. In: *The Journal of Chemical Physics* 42.1 (1965), 288. ISSN: 00219606 (cit. on p. 33).

[101] J. Bishop et al. “Magnetic resonance imaging of shear wave propagation in excised tissue”. In: *Journal of magnetic resonance imaging : JMRI* 8.6 (1998), 1257–1265. ISSN: 1053-1807 (cit. on p. 37).

[102] T. J. Hall et al. “Phantom materials for elastography”. In: *IEEE Transactions on Ultrasonics, Ferroelectrics and Frequency Control* 44.6 (1997), 1355–1365. ISSN: 0885-3010 (cit. on pp. 37 sq.).

[103] U. Hamhaber et al. “Comparison of quantitative shear wave MR-elastography with mechanical compression tests”. In: *Magnetic resonance in medicine* 49.1 (2003), 71–77. ISSN: 0740-3194 (cit. on p. 38).

[104] Masayuki Tokita and Kunio Hikichi. “Mechanical studies of sol-gel transition: Universal behavior of elastic modulus”. In: *Physical Review A* 35.10 (1987), 4329–4333. ISSN: 0556-2791 (cit. on p. 38).

[105] Guido van Rossum. *Python*. 2014. URL: `http://www.python.org` (cit. on p. 43).

[106] van der Walt, Stéfan, S. Chris Colbert, and Gaël Varoquaux. “The NumPy Array: A Structure for Efficient Numerical Computation”. In: *Computing in Science & Engineering* 13.2 (2011), 22–30. ISSN: 1521-9615 (cit. on p. 43).

[107] Eric Jones, Travis Oliphant, Pearu Peterson, et al. *SciPy: Open source scientific tools for Python*. 2001–. URL: `http://www.scipy.org/` (cit. on pp. 43 sq.).

[108] Sebastian Theilenberg. *PyMRR*. 2016. URL: `https://github.com/theilen/PyMRR` (visited on 12/21/2016) (cit. on p. 43).

[109] Fernando Pérez and Brian E. Granger. “IPython: a System for Interactive Scientific Computing”. In: *Computing in Science and Engineering* 9.3 (2007), 21–29. ISSN: 1521-9615. URL: `http://ipython.org` (cit. on p. 43).

[110] F. J. Harris. “On the use of windows for harmonic analysis with the discrete Fourier transform”. In: *Proceedings of the IEEE* 66.1 (1978), 51–83. ISSN: 0018-9219 (cit. on p. 43).

[111] Paul T. Biggs and Janet E. Rogers. “Orthogonal distance regression”. In: *Statistical Analysis of Measurement Error Models and Applications*. Ed. by Philip J. Brown and Wayne A. Fuller. Vol. 112. Providence, Rhode Island: American Mathematical Society, 1990, 183–194. ISBN: 9780821851173 (cit. on p. 44).

[112] R. J. Barlow. *Statistics: A Guide to the Use of Statistical Methods in the Physical Sciences*. Manchester Physics Series. Hoboken: Wiley, 1999. ISBN: 0471922951 (cit. on p. 44).

[113] Martin Ester et al. “A Density-Based Algorithm for Discovering Clusters in Large Spatial Databases with Noise”. In: *Proceedings of 2nd International Conference on Knowledge Discovery and Data Mining*. Ed. by Evangelos Simoudis, Jiawei Han, and Usama M. Fayyad. Menlo Park, Calif.: AAAI Press, 1996. ISBN: 978-1-57735-004-0 (cit. on p. 45).

[114] Fabian Pedregosa et al. “Scikit-learn: Machine learning in Python”. In: *Journal of Machine Learning Research* 12 (2011), 2825–2830 (cit. on p. 45).

[115] *scikit-learn*. 2015. URL: `http://scikit-learn.org` (cit. on p. 45).

[116] Peter A. Jansson. *Deconvolution of images and spectra: Second edition*. Second edition Dover edition. Dover Publications, 2014. ISBN: 0486453251 (cit. on p. 58).

[117] Jürgen Finsterbusch. *IDEA sequence simulation*. 2014-06-10 (cit. on p. 60).

[118] Peter beim Graben. “Estimating and improving the signal-to-noise ratio of time series by symbolic dynamics”. In: *Physical Review E* 64.5 (2001). ISSN: 1063-651X (cit. on p. 64).

[119] R. Mathur-De Vre et al. “The use of agar gel as a basic reference material for calibrating relaxation times and imaging parameters”. In: *Magnetic Resonance in Medicine* 2.2 (1985), 176–179. ISSN: 07403194 (cit. on p. 69).

[120] Elke Hattingen. *Summary of the meningioma diagnostics*. 2015 (cit. on p. 84).

[121] Jakob Bindl et al. “Using a controlled acceleration of the head to access viscoelastic properties of brain tissue”. In: *Proceedings of the Fourteenth International Tissue Elasticity Conference*. 2015, 40 (cit. on p. 97).

[122] Axel Lipp et al. “Cerebral magnetic resonance elastography in supranuclear palsy and idiopathic Parkinson’s disease”. In: *NeuroImage. Clinical* 3 (2013), 381–387 (cit. on p. 100).